UNIVERSITY OF SOUTHAMPTON

FACULITY OF PHYSICAL SCIENCE AND ENGINEERING

Optoelectronics Research Centre

SnS Thin Films for Photovoltaic Solar Cell Applications

by

Ghadah AlZaidy

Thesis for the degree of Doctor of Philosophy

2018

UNIVERSITY OF SOUTHAMPTON

ABSTRACT

FACULTY OF PHYSICAL SCIENCES AND ENGINEERING

Optoelectronics Research Centre

Thesis for the degree of Doctor of Philosophy

SnS Thin Films for Photovoltaic Solar Cell Applications

Ghadah AlZaidy

Currently, a wide range of semiconductors are explored for their potential use as absorbers in photovoltaic (PV) applications. General criteria determining the choice of a particular semiconductor are efficiency, cost, availability, scale production and toxicity of the raw material. Among these materials tin (II) sulphide (SnS) has recently received great attention due to its desirable properties for thin film photovoltaic (PV) applications.

This thesis research has focused on two important goals: the synthesis of efficient thin film absorbers using cost-effective techniques, and incorporating it into a PV device showing its capability of working as a PV absorber. SnS thin films were deposited using two different scalable fabrication methods: chemical vapour deposition (CVD) and radio frequency (RF) sputtering.

First a novel deposition method for SnS films was achieved by room temperature CVD using tin (IV) tetrachloride and H_2S as precursors, providing a facile route to high-quality thin films. As-deposited amorphous sulphur rich tin sulphide thin films were transformed to crystalline p-type single phase SnS thin films by an optimised post annealing treatment. The phase transition was confirmed by x-ray diffraction (XRD), Raman spectroscopy and energy dispersive X-ray spectroscopy (EDX). Single phase SnS thin films with a high carrier concentration around 10^{15} cm^{-3} and mobility of 2.35 cm^2/V.s.

Second, as a comparable study SnS thin films were grown by RF sputtering. The as-sputtered thin films were subjected to post-annealing treatment to improve thin film quality. Specifically, the phase change and improvements in optical and electrical properties were studied with various annealing conditions to find the optimal annealing procedure. Experimental observations shows that annealing at 400 ^{o}C under low pressure for annealing time of 4 hours is optimal to obtain single-phase SnS with a high carrier concentration around 10^{16} cm^{-3} and mobility of 4.74 cm^2/V.s.

SnS thin films by both deposition methods were directly grown on n-type Si wafers. The photovoltaic operation was observed in both heterojunctions from their clear rectifying behaviour signifying the formation of p–n junctions. The RF sputtered films exhibit better photovoltaic performance which can be explained by its better crystallinity which improves the electrical properties allowing lower carrier losses and long diffusion length.

Both growth processes were found to give good quality thin films, showing tin monosulphide as the main phase, large grains and suitable properties for PV application, but higher homogeneity and stoichiometry control were achieved using the RF-sputtering route.

The results from these devices show that both methods for preparing single-phase SnS thin films used here produces high quality material that works excellent as an absorber material for PV applications. This study shows a new opportunity to discover new physics and properties in two-dimensional heterojunctions

Table of Contents

Table of Contents i

List of Tables v

Table of Figures vii

Declaration of Authorship xi

Acknowledgements xiii

Definitions and Abbreviations xv

Chapter 1 Introduction 1

- 1.1 Classification of Thin Film Solar Cells 1
  - 1.1.1 First Generation PV: Crystalline Silicon PV's 2
  - 1.1.2 Second Generation PV: Thin Films Photovoltaics 2
  - 1.1.3 Third Generation PV: Novel and Emerging Technologies 6
- 1.2 Review of SnS Thin Films 8
  - 1.2.1 Structure of SnS 8
  - 1.2.2 Phase Diagram of SnS 9
  - 1.2.3 SnS Potential as a PV absorber 10
  - 1.2.4 Growth Methods of SnS Thin Films 11
  - 1.2.5 Overview of SnS Thin Film Solar Cells 14
  - 1.2.6 Potential Causes of Low Efficiency of SnS Solar Cells 16
- 1.3 Aim of Work 16
- 1.4 Thesis structure 17
- 1.5 References 17

Chapter 2 Principles and Operation of Photovoltaic Solar Cells 23

- 2.1 Introduction 23
- 2.2 The Solar Spectrum 23
- 2.3 Photovoltaic Concepts 24
  - 2.3.1 PN Junction 24
  - 2.3.2 Dark Forward I-V Characteristics of Solar Cells 26
  - 2.3.3 Light Absorption and Carrier Generation 26

    2.3.4 Heterojunctions 28
    2.3.5 Current Density-Voltage Characteristics of Photovoltaic Devices 28

  2.4 Conclusions 32
  2.5 References 32

Chapter 3 Thin film Synthesis & Characterisation Methods 35

  3.1 Introduction 35
  3.2 Thin film Synthesis 35

    3.2.1 Chemical Vapour Deposition (CVD) 35
    3.2.2 Radio Frequency (RF) Sputtering 42

  3.3 Thin-Film Material Characetrsiation Methods 44

    3.3.1 Raman Spectroscopy 44
    3.3.2 X-ray diffraction (XRD) 46
    3.3.3 Scanning Electron Microscopy (SEM) and Energy Dispersive X-ray Spectroscopy (EDX) 47

  3.4 Electrical Characerisation 48

    3.4.1 Hall Effect 48
    3.4.2 Current-Voltage (IV) curves 49

  3.5 References 49

Chapter 4 Synthesis and Characterisation of Single Phase Tin Sulphide Thin Films by Chemical Vapour Deposition 51

  4.1 Introduction 51
  4.2 Feasibility of Reaction by Thermodynamics 51
  4.3 The First Step: Room Temperature Growth of the SnS Thin Films 53

    4.3.1 Influence of Precursor Concentration Ratio $H_2S/SnCl_4$ on the Morphology and Composition of SnS Thin Films 56

  4.4 The Second Step: Post-Depositon Annealing Procedure 58

    4.4.1 Effect of Post-Deposition Annealing Temperature 60
    4.4.2 Results of Compositional and Structural Analysis 61

  4.5 Conclusions 68

4.6 References 69

Chapter 5 Design, Fabrication and Characterization of p-SnS/n-Si Heterojunction by CVD 71

5.1 Introduction 71
5.2 Device Fabrication Process 71
5.2.1 Substrtate Preperation 72
5.2.2 Growth of SnS Absorber Layer 72
5.2.3 Front Contact Deposition 75
5.2.4 Back Contact Deposition 78
5.3 Device Characterisation 79
5.3.1 Current-Voltage (I-V) Measurements 79
5.3.2 Hall-Effect Mobility Measurements 81
5.4 Conclusions 82
5.5 References 82

Chapter 6 Synthesis and Characterisation of Single Phase Tin Sulphide Thin Films by RF sputtering via Post-Deposition Annealing Method 85

6.1 Introduction 85
6.2 Growth of SnS Absorber Layer by RF-Sputtering 86
6.2.1 Stoichiometry of Sputtering Target 86
6.2.2 Sputtering Conditions 87
6.3 Systematic Studies of the Influence of Post-Annealing Treatment 88
6.3.1 Phase Investigation of Effects of Post-Deposition Annealing Treatment in Vacuum at Various Temperatures 88
6.3.2 Phase Investigation of Effects of Post-Deposition Annealing Treatment at Various Annealing Pressures 92
6.3.3 Phase Investigation of Effects of Post-Deposition Annealing Treatment at Various Annealing Times 95
6.4 Conclusions 97
6.5 References 98

Chapter 7 Design, Fabrication and Characterization of p-SnS/ n-Si Heterojunction by RF sputtering 101

7.1 Introduction 101
7.2 65Device Fabrication Process 101
  7.2.1 Substrate Preparation 102
  7.2.2 Growth of SnS Absorber Layer 103
  7.2.3 Front Contact Deposition 105
  7.2.4 Back Contact Deposition 105
7.3 Device Characterisation 106
  7.3.1 Current-Voltage (I-V) Measurements 106
  7.3.2 Hall-Effect Mobility Measurements 108
7.4 Conclusions 108
7.5 References 108

Chapter 8 Conclusions and Future Work 111

8.1 Conclusions 111
8.2 Future Work 114
8.3 References 115

Appendix A1: Thermodynamics Data for Calculating the Gibbs free energy, Entropy and product concentration 116
Appendix A2: Thermodynamics Data for Calculating the Concentration of Reaction Products at Various Deposition Temperatures 118
Appendix A3 Single crystal XRD data (Inorganic Crystal Structure Database (ICSD) 122
Appendix A4 Hall Measurements for SnS films by CVD 123
Appendix B1 Sputtering Deposition Conditions 125
Appendix B2 EDX of SnS target 127
Appendix B3 Electrical Characterisation of RF Sputtered SnS/n-Si heterojunctions 129

List of Tables

Table 4.1 The effect of the precursor $H_2S/SnCl_4$ ratio concentration on film composition.57

Table 4.2 Composition of H_2S annealed SnS thin films obtained by EDX. 62

Table 8.1 Performance of SnS-based devices by performance 113

Table of Figures

Figure 1.1 Highest recorded solar cell efficiencies, complied by the National Renewable Laboratory, USA [5]....7

Figure 1.2 Schematic diagram of double structured layered of orthorhombic SnS [42]. ..8

Figure 1.3 Structures of the Pmna, Cmcm, π-cubic, rocksalt and zincblend phaes of SnS [48]. 9

Figure 1.4 Phase diagrams of the Sn-S system calculated by Lindwall et al. at (a) 1 bar, (b)1 mbar and 10^{-3} mbar where L and G represent liquid and gas phases respectively [53]....10

Figure 1.5 Absorption coefficients for common materials used in PV technology as compared to sputtered SnS thin films [57]....11

Figure 1.6 a) Schematic diagram of a SnS solar cell b) A cross section SEM image of a SnS solar cell [86]....15

Figure 1.7 Schematic of SnS devices b) Schematic of cross section of SnS thin film solar cell [87]....15

Figure 2.1 Schematic of the sun's position for determination of air mass (AM).....24

Figure 2.2 The formation of a p-n junction. A p-type and an n-type semiconductor in contact resulting in diffusion flux of charged carriers and formation of a built in field.25

Figure 2.3 Photon absorption in a semiconductor. 27

Figure 2.4 Schematic of solar cell equivalent circuit diagram. 30

Figure 2.5 Current-Voltage (I-V) curve for photovoltaic device under illumination (red) and in dark (black)) [6]....31

Figure 3.1 Schematic summary of the most important reactions involved in film synthesis by CVD. 36

Figure 3.2 Schematic of the CVD reactor system. 40

Figure 3.3 Gas flow control panel with all MFC's. 41

Figure 3.4 Schematic of the bubbler system for liquid precursor [3].....42

Figure 3.5 image of a NANO sputter facility in ORC clean room (left) and Schematic of a sputtering system (right). 43

Figure 3.6 Schematic of energy level showing the states involved in Raman spectra (left), Renishaw inVia Raman microscope used to characterise the thin films in this thesis (right). 45

Figure 3.7 Schematic diagram of XRD experiment (left), image XRD system used in this thesis. 46

Figure 3.8 Schematic diagram of scanning electron microscope (SEM) (left), image of the ZEISS SEM facility in ORC (right). 47

Figure 4.1 Changes in Gibbs free energy of possible reactions in the CVD process. 52

Figure 4.2 Change in reaction product concentration according to eq. 4.2 and Gibbs free energy at different deposition temperatures. 53

Figure 4.3 Schematics of CVD system used to grow SnS thin films in this thesis. 54

Figure 4.4 The CVD system in ORC (a) shows the reactor and injection of gases (b) shows the glass bubbler of tin precursor. 55

Figure 4.5 SEM image of as-deposited SnS films at optimised deposition conditions. 55

Figure 4.6 Effect of $H_2S/SnCl_4$ precursor concentration ratio on the reaction product concentration. 56

Figure 4.7 SEM images showing the effect of precursor concentration ratio on the morphology of SnS thin films. 58

Figure 4.8 Schematic diagram of CVD annealing system. 60

Figure 4.9 XRD patterns of SnS thin films annealed in H_2S atmosphere at different annealing temperatures. 63

Figure 4.10 Standard XRD patterns for SnS, Sn_2S_3 and SnS_2 extracted from ICSD. 63

Figure 4.11 Raman spectra of (a) SnS_2 (b) Sn_2S_3 (c) SnS [16]. 65

Figure 4.12 Raman spectra of the samples annealed at various temperatures. 66

Figure 4.13 SEM images of the films annealed at various temperatures. 68

Figure 4.14 SEM cross section of the sample annealed at 350 °C on soda lime substrate.68

Figure 5.1 Schematic of SnS/n-Si heterojunction solar cell. 71

Figure 5.2 XRD of bilayer SnS thin films on n-type silicon substrates. 73

Figure 5.3 Energy Dispersive X-ray Analysis (EDX) of bilayer SnS thin films. 74

Figure 5.4 Raman spectra and SEM images of both layers of SnS thin films. 75

Figure 5.5 Optical microscope image of the Cr/Au (5nm/50nm) contacts deposited on SnS film. 76

Figure 5.6 Energy band diagram of SnS film and metal structure [6]. 77

Figure 5.7 IV plot of Au/SnS measured at room temperature. 78

Figure 5.8 I-V curve of Au/SnS/n-type S/Al heterojunction under dark conditions showing clear current rectification (the inset shows the I-V plotted in semi-log scale).79

Figure 5.9 The I-V curve of SnS/n-Si under 633 nm laser illumination. 80

Figure 5.10 I-V characteristics of SnS/n-Si heterojunction solar cell under 633 nm laser. 81

Figure 6.1 Energy dispersive X-ray of SnS (1:1) target showing atomic ratio of target elements and SEM image of SnS target. 86

Figure 6.2 Table shows EDX composition of the SnS target compared to the as-deposited thin films sputtered from the SnS target and SEM image of the as-deposited thin films. 87

Figure 6.3 XRD spectra of the annealed samples at different temperatures at fixed pressure and annealing time. 89

Figure 6.4 Raman spectra of the annealed samples at different temperatures at fixed pressure and annealing time. 91

Figure 6.5 SEM images of the SnS films annealed at various temperatures, fixed pressure and annealing time. 92

Figure 6.6 XRD spectra of the annealed samples at different temperatures at fixed temperature and annealing time, with a total pressure of 6 mbar. 93

Figure 6.7 Raman spectra of the annealed samples under different pressures at fixed annealing temperature of 400 °C and annealing duration of 2 hours ,with a total pressure of 6 mbar. 94

Figure 6.8 Plot of domains of stability of different sulphides of Sn as a function of temperature under S vapour [10]. 95

Figure 6.9 XRD spectra of the annealed samples at different annealing durations 2, 4, 6 hours, at fixed temperature 400 C, with a total pressure of 6 mbar. 96

Figure 6.10 Raman spectra of annealed samples at different annealing durations 2, 4, 6 hours at fixed temperatures at a fixed annealing temperature of 400 °C ,with a total pressure of 6 mbar. 97

Figure 7.1 SEM images showing top surface of (a) RF sputtered SnS films and (b) SnS films by CVD. 102

Figure 7.2 Schematic of the SnS/n-Si solar cell device structure. 102

Figure 7.3 XRD spectra of the RF sputtered films deposited at room temperature and post annealed at 400 °C for 2 hours,with a total pressure of 6 mbar. Experimental XRD peaks are compared to SnS diffraction peak positions listed by JCPFS (039-0354). 104

Figure 7.4 Raman spectra of the RF sputtered films deposited at room temperature and post annealed at 400 °C for 2 hours, with a total pressure of 6 mbar. 104

Figure 7.5 I-V characteristics of the Au contacts on RF sputtered SnS thin films. 105

Figure 7.6 I-V curve of Au/SnS/n-type Si/Al heterojunction under dark conditions showing clear current rectification (the inset shows I-V plotted in semi-log scale). .. 106

Figure 7.7 I-V characteristics of SnS/n-Si heterojunction solar cell under 633 nm laser.107

Declaration of Authorship

I, Ghadah Alzaidy declare that this thesis and the work presented in it are my own and has been generated by me as the result of my own original research.

SnS Thin Films for Photovoltaic Solar Cell Applications

I confirm that:

1. This work was done wholly or mainly while in candidature for a research degree at this University;
2. Where any part of this thesis has previously been submitted for a degree or any other qualification at this University or any other institution, this has been clearly stated;
3. Where I have consulted the published work of others, this is always clearly attributed;
4. Where I have quoted from the work of others, the source is always given. With the exception of such quotations, this thesis is entirely my own work;
5. I have acknowledged all main sources of help;
6. Where the thesis is based on work done by myself jointly with others, I have made clear exactly what was done by others and what I have contributed myself;
7. None of this work has been published before submission [or] Parts of this work have been published as: [please list references below]:

Signed:

Date: 30/01/2019

Acknowledgements

Definitions and Abbreviations

PV	Photovoltaic
AM	Air Mass Coefficient
E_g	Bandgap Energy
SnS	Tin Monosulphide
SnS_2	Tin Disulphide
V_{oc}	Open Circuit Voltage
I_{sc}	Short Circuit Current
q	Elemental Charge
CVD	Chemical Vapour Deposition
FF	Fill factor
d	Film thickness
CdS	Cadmium sulfide
CZTS	Copper zinc tin sulfide(Cu_2ZnSnS_4)
n	Diode ideality factor
R_s	Series resistance
H_2S	Hydrogen sulphide
Sn	Tin
RH	Hall coefficient
Au	Gold
R	Resistance

Chapter 1 Introduction

1.1 Classification of Thin Film Solar Cells

For over a century, electricity transformed human's lifestyle and became a necessity in every household. The need for more energy supplies due to increased demand has increased interest in the development of novel technologies that make use of solar energy. Although an essential form of energy, the generation of electricity does not come without a cost to the environment. Most of electricity worldwide is generated from fossil fuels such as coal, natural gas and oil. This is an inefficient and costly method. The alternative would be a renewable resource that does not negatively impact the environment or contribute to climate change. Solar energy is a cost-effective resource since the sun continuously supplies it. Solar cells are devices that convert solar energy into electricity based on the photovoltaic effect. PV cells are made of semiconductor materials. Many organic and inorganic materials have been investigated for PV devices. Although currently a wide range of semiconductors materials are explored for their potential use in photovoltaic applications, only few of them have commercial interest to due to satisfying constraints such as efficiency, cost, toxicity, and availability. The starting point of the photovoltaic technology can be referred to Alexandre-Edmond Becquerel in 1839, the father of solar cells. Scientific curiosity led him to discover the reaction of semiconductors under illuminance when he was observing the generation of current flowing when setting two platinum plates in contact with an aqueous acidic galvanic cell under illumination. His research innovation can be considered as the discovery of the photovoltaic (PV) effect, the main principle of PV technology [1] . Later on, the first solar cell was produced at Bell Laboratories in the 1950's [2].

In the past decade photovoltaics have become a major contender for producing power on a large scale, either in centralised power stations or integrated into buildings (BIPV, "building integrated photovoltaics"). In 1954 Reynolds et al. produced a cuprous sulphide/cadmium sulphide heterojunction solar cell where 6% efficiency was achieved [3]. This step attracted interest in developing thin film solar cells devices as it proved that thin film technology is a more viable low cost approach compared to bulk silicon devices [3]. PV cell technology is usually classified into three main generations: first generation, second generation and a third generation of PV devices depending on the materials used and level of commercial maturity. Each of these has its own advantages and disadvantages that are subsequently discussed

1.1.1 First Generation PV: Crystalline Silicon PV's

First generation PV systems are fully commercialised and use single crystalline or multi-crystalline silicon. Commercial production of crystalline silicon (SCS) modules began in 1963 where a 242 W PV fixture on a lighthouse was installed by SHARP, one of largest installation at that time [4].

Due to the mature silicon semiconductor industry and material abundance it builds upon the accumulated knowledge base of the silicon-chip electronics industry showing the state-of-art production techniques for PV modules with high efficiencies. In addition, silicon is non-toxic and abundantly available in the earth crust. As a result, these type of cells are the most popular in the PV market, accounting for around 90% of the global sales in 2017 [5]. Silicon based solar cells show relatively high efficiencies, up to 26.7% have been achieved for single-crystalline solar cells and 22.3% for multi-crystalline silicon wafer based PV technology [5-7]. However, silicon is an indirect band gap material and as such needs a larger light-harvesting region than typical direct gap materials in order to operate effectively. The cost distribution of this technology is dominated by material's costs, especially by the costs of the silicon wafer. Other challenges of the technique are the purity requirements and their low throughput. These factors form the primary impetus behind the wealth of research that has led to the development of the subsequent generations of photovoltaic devices.

1.1.2 Second Generation PV: Thin Films Photovoltaics

Shockley-Queisser studied the theoretical efficiency limit for an ideal homo-junction solar cell (also known as the Shockley-Queisser limit and found that, the maximum possible efficiency is 30% for a band gap of 1.1 eV (assuming only radiative recombination) if exposed to the sunlight of global air mass 1.5 [8, 9]. This value is relatively close to the most recent data published in Progress in Photovoltaics which reports a crystalline silicon (Si) solar cell efficiency of 25% measured under the AM 1.5 spectrum at 25°C [10]. Although silicon cell technology currently dominates the market, accounting around 90% of the market, its drawbacks show that the Si is not considered a viable candidate for low cost thin film PV devices.

The second generation of PV technology was developed with the aim of reducing the high costs prevalent in the first generation through the utilisation of thin film technology. The idea was to save on bulk material cost with a significant reduction in the quality and quantity of the material used, with the challenge of increasing the thin film absorption to compensate for the reduced thickness in the photoactive layer. Second generation solar cells are known as thin-film solar cells (TFSC) because when compared to crystalline silicon based cells they are made from layers only a few micrometres thick and can go down to hundreds of nanometres. The huge reduction of the active material requirement respect to the standard technology allows a large decrease of the device costs. Moreover, the large versatility in the device design and fabrication, due to the wide choice of different substrates (rigid, flexible) and deposition techniques for the different device layers, allow engineering and optimizing the solar cell stack in order to enhance the device performances [11]. Among others, thin-films cells are thought to be the simplest, cheapest and most sustainable method of solar cell production.

Besides which, the highest efficiency achieved to date for a single junction cell was obtained with a thin-film device. In addition, the light absorption in near the junction region which makes long minority carrier diffusion length not necessary, as a consequence the need for high purity material. Thin film solar cells also lend themselves to large scale, low cost production, resulting in shorter energy payback times.

The three primary types of thin-film solar cells in terms of commercial development are hydrogenated amorphous silicon solar cells (a-Si), cadmium telluride (CdTe) and copper indium gallium diselenide solar cells.

Amorphous Silicon (a-Si)

Amorphous silicon (a-Si) is a non-crystalline semiconductor in which the composed of randomly oriented Si atoms in a homogenous layer rather than a crystal structure. This changes the absorbance characteristics of the material and can allow thinner layers to be used for devices. For this reason a-Si is also among the thin film solar cells and has a direct bandgap of 1.7 eV and an optical absorption coefficient $\alpha > 10^5$ cm^{-1}, means that only a few microns of material are needed to absorb most of the incident light, reducing materials usage and hence cost. This type of films are deposited by decomposition of silane (SiH_4) by CVD (chemical vapour deposition), plasma enhanced chemical vapour deposition (PECVD) or hot wire CVD [12, 13]. Although attempts have been made in the form of amorphous silicon, a-Si, cells, but these only exhibited efficiencies in the 10-12% range [14]. One of the disadvantages of this technology is the low efficiency of 12% compared with crystalline solar cells. In addition, the major problem associated with the a-Si solar cells is the degradation of performance over time [15].

Chalcogenide Based Compounds

Chalcogenide thin film solar cells are based on chalcogenide absorbers, like CdTe, Cu(In,Ga)Se2. Chalcogenides have recently gained much attention due to their potential for producing low-cost, high-efficiency, large-area thin-film solar cells [16]. The favourable optical properties of these materials such as optimum band gap and high absorption coefficient allow the use of thin films (few nanometres) instead of thick bulk layers of silicon. A brief discussion of various chalcogenide compound based solar cells will be mentioned in the following sections.

Cadmium Telluride (CdTe)

Cadmium telluride (CdTe) is an II-VI binary chalcogenide semiconductor with a band gap of around 1.44 eV, a value which is close to the optimal bandgap for solar cell. Research in this material dates back to the 1950's, Loferski showed that the optimum energy bandgap for photovoltaic solar energy conversion is 1.5 eV [17]. This led him to suggest that CdTe which has a direct energy gap near to this value showing that CdTe is a promising PV material [18, 19]. CdTe solar cells are usually partnered with cadmium sulphide (CdS), which has n-type conductivity. In 1972, Bonnet and Rabenhorst reported an efficiency of 6% on CdTe/CdS thin film solar cells [20]. Subsequent concentrated research effort by several groups worldwide resulted in improving the efficiency of CdTe devices, where a record efficiency of 16.5% has been reported by the NREL group in 2001 subsequently exceeded in 2014 going up to >21% [21, 22]. Although cells with high efficiencies have been achieved, some problems remain. The major drawbacks of thin film CdTe technology originate from the toxicity of cadmium and scarcity of tellurium which limit the production of this material. The greatest advantage of CdTe cells is the payback time which has been shown to be less than one year, a powerful advantage over first generation technologies [23].

Copper-Indium Diselenide (CIS)

Copper indium selenide ($CuInSe_2$) (CIS) is a ternary compound p-type absorber material belonging to the I–III–VI_2 family. CIS solar cells have shown long-term stability and the high conversion efficiencies. Solar cells based on these materials are also very stable, thus allowing long operational lifetimes. CIS-based solar cells can be prepared both from gas and liquid phases by a variety of methods including evaporation from elemental or compound sources, selenization of precursor layers, chemical vapour deposition etc. The first $CuInSe_2$ thin film solar cell was fabricated with an efficiency of 4–5% by evaporating $CuInSe_2$ powder in the presence of excess Se vapour [24]. Later, by using the co-evaporation technique, an efficiency of 11.4% was reported by Boeing [25]. Solar Frontier successfully achieved a world record thin-film solar cell efficiency of 22.3% which have set a new world record for thin-film solar cell efficiency [26].The electrical properties of CIS greatly depend on its elemental composition, especially Cu/In ratio It is known that stoichiometric CIS shows p-type conductivity, while Cu-deficient show n-type conductivity. This means that precise control for the optimisation is required.

Copper Indium Gallium sulphide (CIGS)

Addition of gallium to $CuInSe_2$ has been widely used, as it is reported to improve the device performances. The relatively low band gap energy of $CuInSe_2$ (1.04 eV) is responsible for the low open circuit voltage generally observed in solar cells made of this material. As gallium is added to the structure the band gap energy of the compound is raised to a maximum value of 1.7 eV [27, 28].

The larger band gap of CIGS is responsible for a higher built-in potential of the device, which results in the increase of the open circuit voltage.

Quaternary chalcogenides have attracted extensive attention due to their exceptional optoelectronic device characteristics [29]. Copper indium diselenide $CuInSe_2$ (CIS), and the related compounds such as $Cu(In,Ga)Se_2$ (commonly abbreviated as CIGS) and $Cu(In,Ga)(Se,S)_2$ are the most leading chalcogenide absorber materials in large-scale photovoltaic systems. . CIGS absorber layer is formed mainly by the co-evaporation of the elements or the deposition of the metallic precursor layers by sputtering followed by selenization. Co-evaporation yields devices with the highest performances, while the latter deposition process is preferred for large-scale production since it allows to obtain better compositional uniformity over a large area In 2014 small area CIGS solar cells have reached an efficiency of 20.9 % close to the record efficiency of bulk crystalline Si dollar cells 25% [30, 31]. Large-area modules of CIGS with efficiency of about 13-14% are currently produced on industrial scale. Despite the large development of the actual chalcogenide-based PV, these technologies suffer from using rare elements, such as In, Ga, whose critical supply could be one of the main limits for the sustainability of these technologies in the years to come [32].

The development of new abundant, environmental friendly and low cost materials as possible alternative to CIGS alloys is a challenge to fulfil the requirements of PV massive production on terawatt scale foreseen in 2020-2040 [33].

Cu_2ZnSnS_4 (CZTS) and $Cu_2ZnSn(Se)_4$ CZTSe

In the last two decades, many efforts have been addressed to the development of a new class of quaternary compounds as possible candidates to replace CIGS in thin film solar cells. These materials can be thought of as a derivation of CIGS structure, by a process known as "cross-substitution", consisting in the replacement of one element (In or Ga in the present case) with a couple of two elements of different groups of the periodic table, keeping fixed the ratio between the number of atoms and valence electrons. The resulting materials are therefore quaternary compound given by the chemical formula Cu_2-II-IV-VI_4, where VI is a chalcogen element (S or Se) while II and IV represent divalent (Zn, Cd, Fe) and tetravalent (Sn, Ge, Si) elements, respectively.

Among the possible Cu_2-II-IV-VI_4 compounds, are $Cu_2ZnSn(S,Se)_4$ CZTSSe the most studied and the rapid improvement of photovoltaic performances obtained in the recent years makes these materials even much attractive. These compounds are very promising materials, being composed by low cost, widely available showing desirable properties for thin film photovoltaic applications. CZTSSe are spontaneously p-type semiconductors, with a direct band gap energy between 1 eV (for the pure selenide $Cu_2ZnSnSe_4$ alloy) and 1.5 eV (for the pure sulphide Cu_2ZnSnS_4), close to the optimal value to match the solar spectrum (in the limit of radiative recombination only, the theoretical conversion efficiency predicted by Schokley and Queisser for such semiconductors is as high as 30%). The direct band gap gives a high absorption coefficient, making these materials suitable as thin film photoactive layers, since a sensible absorption of the incoming light occurs within about one micron.

The emergence of CZTS and CZTSSe has been an important step forward the design of earth abundant PV with the promise of scalability and low cost [34].

The first CZTS device report of 0.66% efficiency lead to active research on CZTSSe-based solar cells, which after extensive optimization effort has led to efficiency values of up to 12.6% [35, 36].

1.1.3 Third Generation PV: Novel and Emerging Technologies

Emerging technologies, known as “third-generation PV”, could become viable commercial options in the future either by achieving very high efficiency or very low cost. Examples include dye-sensitised solar cells (DSSC) and organic PV cells, which are based on a photo-electrochemical system with the semiconductor formed between a photosensitised anode and an electrolyte [37, 38]. This technology is relatively new but one of the most developed among third generation PV. Other examples of third generation devices include the use of quantum dots, plasmonic nanostructures, intermediate band, multi-junctions and bio-inspired materials. Another recently developed PV technology is that of perovskite solar cells [39]. This technology is inspired from DSSC, but the electrolyte dye has been substituted with solid state material. Engineering of these solar cells leads to high performance, however stability is one of the main issues with these cells, which is a common problem for devices based on organic material. All these technologies have promising theoretical potential which is being developed currently in many universities and research centres. The certified progress of all of the technologies discussed in this section, and more, are plotted over time in Figure 1.1.

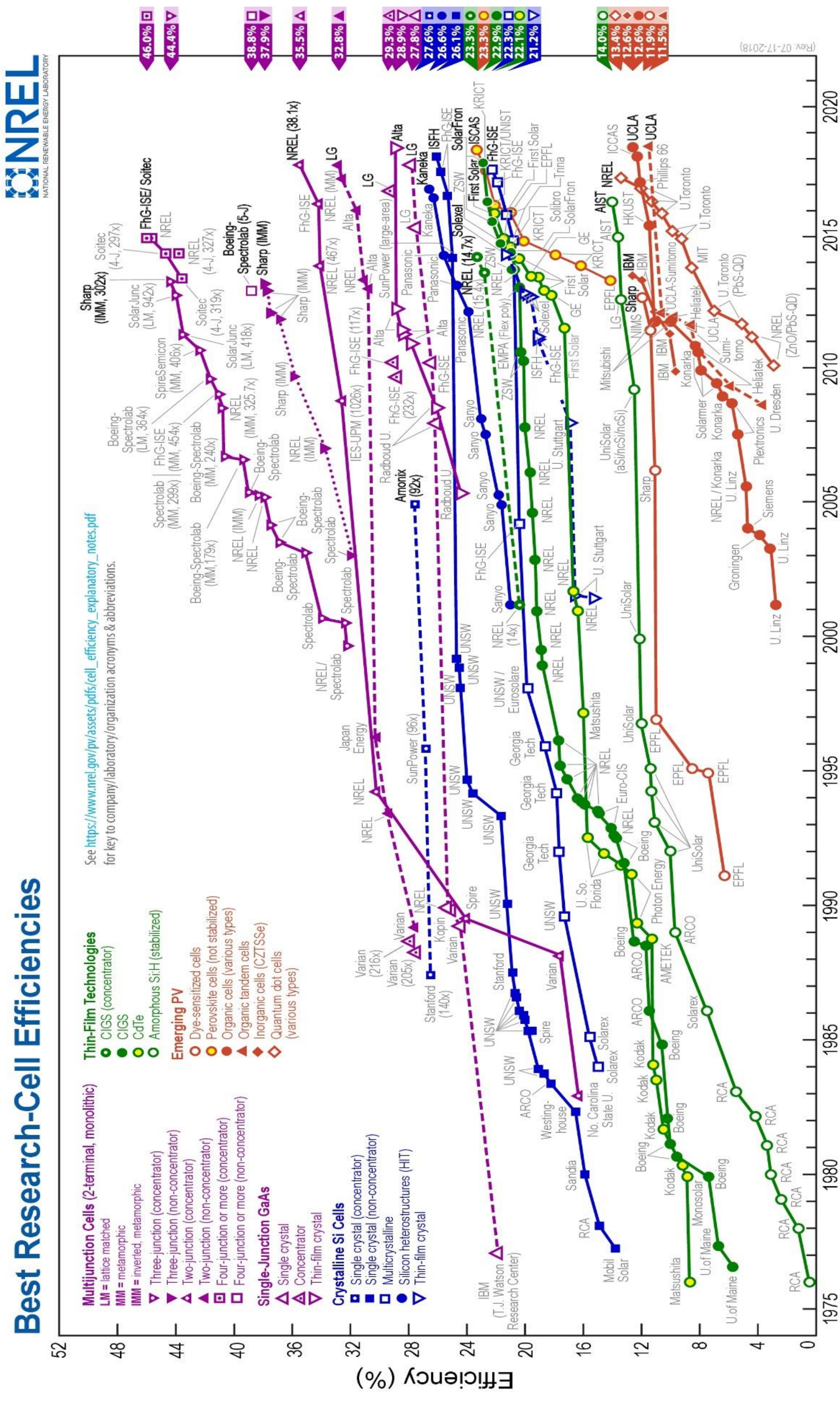

Figure 1.1 Highest recorded solar cell efficiencies, complied by the National Renewable Laboratory, USA [5].

1.2 Review of SnS Thin Films

1.2.1 Structure of SnS

Among the IV-VI semiconducting compounds, tin chalcogenide exhibit orthorhombic structure with eight atoms per unit cell forming double layer planes normal to the longest axis. A tin monosulpde (SnS) compound was first reported by the German mineralogist Robert Herzenberg in 1932, hence the reason the mineral to be recognized as Herzenbergite [40]. Sn(II) has the electron configuration [Kr] $4d^{10}$ $5s^2$ $5p^6$ and forms stoichiometric SnS that preferentially crystallizes in the orthorhombic (OR) crystal structure where every Sn atom (with the with oxidation state of Sn^{+2}) coordinates with three S atoms (with oxidation state S^{2-}) as nearest neighbours with three short Sn-S bonds, belonging to the space group *Pnma* within the orthorhombic crystal system. Bi-layers of SnS stacked along the *c* axis forming a natural (001) cleavage plane. The lines connecting Sn with interlayer S-atoms are approximately mutually perpendicular and the same is true for the inter-layer S atoms [41]. Figure 1.2 shows a view of the orthorhombic crystal structure of SnS revealing the layered crystal structure with slabs each two atoms thick [42].

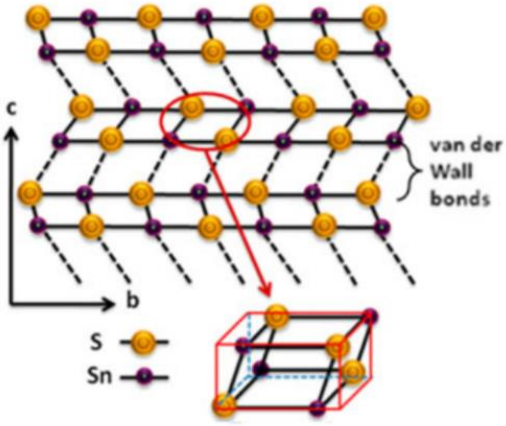

Figure 1.2 Schematic diagram of double structured layered of orthorhombic SnS [42].

It implies that these layered structures are connected along c-axis with weak van der Waal's forces. This defect-tolerant surface might reduce the carrier recombination loss due to defects at p-n junctions at grain boundaries and hence increased carrier lifetime [43].

Other stable phases of SnS that are of interest are a high temperature Cmcm phase [44], and three cubic phases: the rocksalt (RS) phase $(Fm\bar{3}m)$ [45], the zincblende (ZB) structure $(F\bar{4}m)$ [46] and the recently reported π-cubic $(P2_13)$ consisting of 64 atoms in the unit cell[47] ,as shown in Figure 1.3 [48].

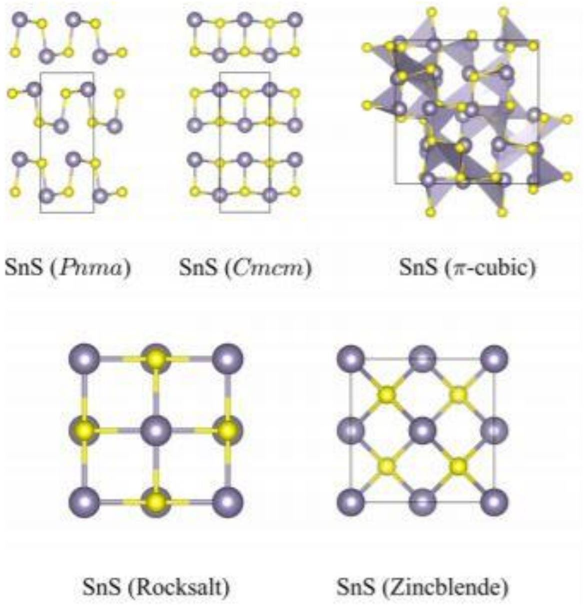

Figure 1.3 Structures of the Pmna, Cmcm, π-cubic, rocksalt and zincblend phaes of SnS [48].

1.2.2 Phase Diagram of SnS

In order to grow SnS thin films under controlled conditions it is necessary to have knowledge of the phase diagram of the Sn-S system. Tin sulphide is a challenging material to work with due to the dual valency of tin (Sn^{2+} and Sn^{4+}) which enables tin to form various phases dependent on the growth conditions and as a result making phase pure SnS material a challenge. Tin sulphide (Sn_xS_y) can appear in range of sulphide phases which include SnS, SnS_2 and Sn_2S_3. Experimentally, it is known that the S–Sn system contains four solid solution phases (α-S, β-S, α-Sn and β-Sn), a liquid phase with two miscibility gaps and a gas phase. Until recently availability of phase diagrams for Sn-S in the literature were limited to atmospheric pressure at varying temperature as a function of composition. The earliest work on the $T - x$ phase digram of Sn-S system was done by Pelabon [49] and Biltz [50]. In 1961, Albers et al. [51] complied the data of several investigators and some of their own into phase diagram for the Sn-S system. In 1986, Sharma et al. [52] reviewed the data for Bulletin of Alloy Phase Diagrams.

With many groups using vacuum deposition techniques and annealing processes, the phase diagram provides little guidance for choosing optimal temperatures and sulphur partial pressures. Newer phase diagrams were developed by the CALPHAD (Calculation of Phase Diagrams) technique using first-principles calculations by Lindwall *et al.* [53].

These phase diagrams examine the Sn–S system at varying pressure as well as varying temperature, which is useful for vacuum processing. An example of the calculated phase diagrams is shown in figure showing the phase relationship and transformation temperature for the different forms of the intermediate phases of the Sn-S system at three different pressures s (1 bar, 1 mbar, and 0.001 mbar), Figure 1.4.

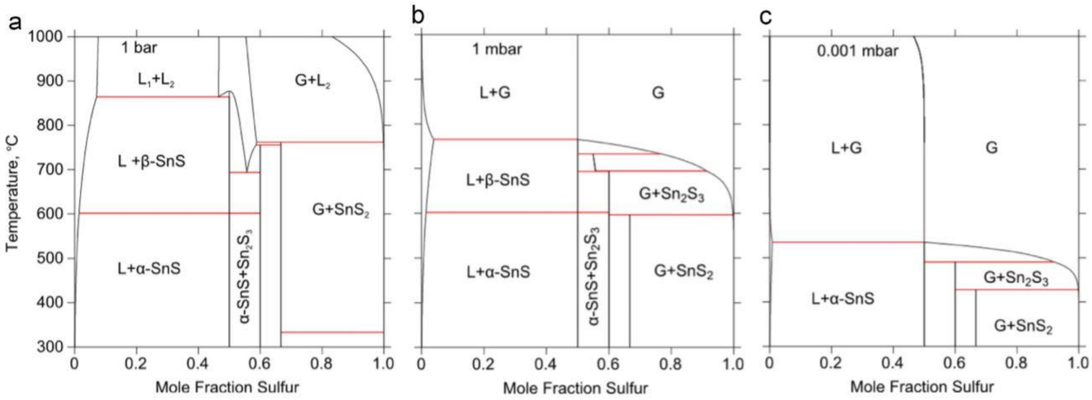

Figure 1.4 Phase diagrams of the Sn-S system calculated by Lindwall et al. at (a) 1 bar, (b)1 mbar and 10^{-3} mbar where L and G represent liquid and gas phases respectively [53].

At a pressure of I bar the gas pressure stable above ~735 K on the rich side, which is a temperature similar to the experimentally measured boiling temperature for pure sulphur (717.8 K) [54]. As the pressure decreases, the stability region for gas increases and the sublimation temperature for the compounds decreases. Note that the order of the sublimation temperatures for the SnS_2 and the Sn_3S_2 compounds changes as the pressure is decreased. SnS_2 is stable up to a higher temperature compared to the Sn_2S_3 at higher pressure, whereas Sn_2S_3, due to its lower sulphur content, is the thermally more stable sulphide at lower pressure.

1.2.3 SnS Potential as a PV absorber

Although the chalcogenide compounds mentioned in 1.1.2.2 have shown some promising properties, it is important to develop systematic design principles that accelerate the discovery of novel materials with lower cost and higher efficiency. In ternary and quaternary compounds, the formation of secondary phases is very harmful for thin-film solar cells. However, for multi-compound materials such as CIGS and CZTS, the formation of a secondary phase is possible which will highly effect the electrical properties of the material and reduce the overall efficiency of the device. Moreover, the main disadvantage of the co-evaporation process in three successive stages lies in its scalability to industrial production level, since it would require relatively long production times and several lines of evaporation sources.

One of these candidates is tin sulphide, a binary metal sulphide (IV-VI) compound semiconductor material, satisfies these advantages which has a simpler chemistry than multicomponent chalcogenide materials. Both elements Sn and S are non-toxic, earth abundant and low cost elements make SnS a suitable PV absorber for safe manufacturing at scale. SnS also has a wellsuited bandgap and absorption coefficient for use as a solar absorber material with an optical band gap between 0.9 eV and 1.8 eV, which lays in the region to the optimum for photovoltaic solar energy conversion [55]. SnS exhibits intrinsic p-type conductivity and a high absorption coefficient >10^5 cm^{-1} ,Figure 1.5 [56] .

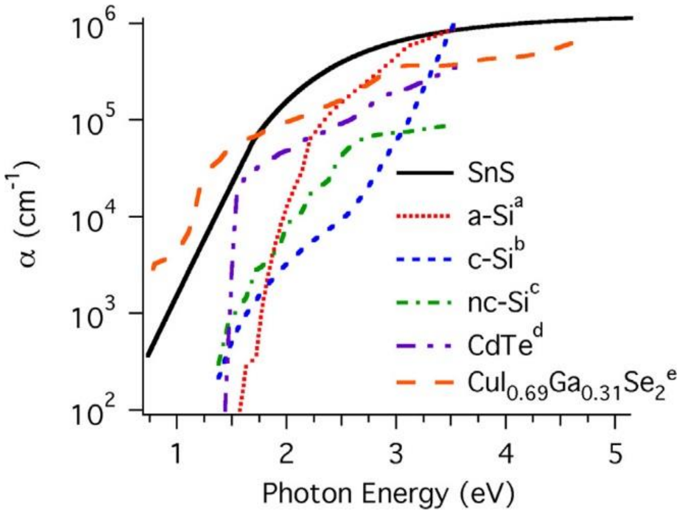

Figure 1.5 Absorption coefficients for common materials used in PV technology as compared to sputtered SnS thin films [57]

Besides this, the fabrication of binary compounds, where properties are tailored to PV applications by varying the stoichiometry of individual components, is simpler to optimise compared with quaternary compounds such as CIGS and Cu2ZnSnS4 (CZTS), therefore the processing and manufacturing difficulties are less. Ternary and quaternary compounds lead to the formation of various phases during the fabrication process. These phases will affect the electrical and optical properties of the material which can be detrimental to efficiency. Furthermore, SnS is very suitable for sublimation type deposition methods due to its relatively high vapour pressure and desorption. Thus, by all mentioned parameters m measures we conclude that SnS is an ideal absorber materials for PV.

The main disadvantage of the co-evaporation process in three stages lies in its scalability to industrial production level, since it would require relatively long production times and several lines of evaporation sources.

1.2.4 Growth Methods of SnS Thin Films

Here we provide a brief review of the progress in the work done so far on growth methods of SnS. Perfecting the process was important for achieving control of phase purity and producing high quality single phase material. SnS thin films were prepared by various chemical and physical methods which could be categorized into three areas. The first method involves solution-based techniques such as chemical bath deposition (CBD) and electrodeposition. CBD is a simple and very popular technique for thin film deposition, especially for the deposition of chalcogenide thin films. Electrochemical deposition is a low cost, easily scalable deposition method that has good control and operates at atmospheric pressure. A second technique is physical vapour deposition such as thermal evaporation and RF sputtering [28]. The last method uses transport by chemical vapours such as chemical vapours deposition (CVD), and atomic layer deposition (ALD). A short summary of some of these techniques is presented in order for context of this thesis work. These includes the methods used to achieve highest efficiency of SnS based thin film solar cells, spray pyrolysis and thermal evaporation. In addition, a brief review on SnS thin films produced by CVD and RF sputtering since they will be the depositing methods utilized in this thesis.

Spray Pyrolysis

Spray pyrolysis involves spraying an aqueous solution containing soluble salts of the constituent atoms/vapour of the required compound onto a substrate at very high temperatures, such that pyrolytic (endothermic) decomposition is achieved, resulting in the formation of a single crystal or an aggregate of crystallite of the required product. It is a very versatile and economic technique widely used to produce SnS films. One of the great advantages of using this technique is that it allows stoichiometric doping and/or adding an external agent to the solution with the precursor making the precursor concentration one of the most important variables in this process. The Reddy group were the first worker to report spray pyrolytic deposition of SnS films [57]. The absorber layer thickness was 0.6 µm at 350 ◦C and the optical band gap was found to be 1.32 eV [56]. Jeyaprakash *et al*. deposited pure single phase SnS thin films with an optical band gap of 1.35 eV at 300 °C [58].

Thermal Evaporation

Thermal evaporation techniques resistive, electron beam and flash evaporation are the simplest techniques as compared to all other physical vapour deposition (PVD) techniques. According to measurements of the vapour phase for the evaporation of SnS, Colin and Drowart [59] found that SnS evaporates congruently, which makes it a desirable candidate for thermal evaporation.

Many studies exploring the parameter space for thermally evaporated SnS have been done. Substrate temperature was found to be directly related to Sn-to-S ratio [60]. Nwofe *et al*. deposited high quality SnS films of good crystallinity with thicknesses in the range 2-3.6 µm using substrate temperatures in the range 320 °C and 360 °C [61].

Atomic Layer Deposition (ALD)

Atomic layer deposition (ALD) is a technique used for the deposition of various thin films and nanostructures by introducing the material precursors one at a time in sequential steps to form a continuous thin films. ALD SnS thin films was reported by Kim *et al*. using the reaction of tin 2,4-pentaneionate ($Sn(acac)_2$) and hydrogen sulphide (H_2S) [62]. However, the growth rate was relatively low resulting in an unfavourable thermodynamic enthalpy change. Ham et al. reported ALD SnS thin films from $[(CH_3)_2N]_4Sn$ precursor which contains Sn in the +4 oxidation state, and the phase of the grown films was reported to change from the hexagonal SnS_2 at intermediate temperatures of 140-150 °C to orthorhombic SnS at temperatures of 160-180 °C [63]. Later on, Sinsermsuksakul et al. reported pure SnS films from the reaction of bis(N,N'-disopropylacetamidinato)tin(II) referred to as ($Sn(acac)_2$) and H_2S at substrate temperatures between 100 and 200 °C [64]. The utilization of a Sn(II), rather than Sn(IV) precursor significantly influenced the growth of the impurity-free SnS phase over a relatively low temperature range. In 2014, the same group fabricated SnS thin films by ALD devices by ALD using alternative doses of the same tin precursor at a temperature of 90 °C (($Sn(acac)_2$) and H_2S gas) achieving a record efficiency of 4.36% with the SnS [65].

Chemical vapour deposition (CVD)

Chemical vapour deposition (CVD) is able to grow high quality thin films with thickness control over large areas at high growth rates. Plasma enhanced chemical vapour deposition (PECVD) and conventional CVD have been shown to deposit SnS. Pure tin sulphide mono phase thin films have been prepared by the PECVD technique, using $SnCl_4$ and H_2S as source materials at temperatures ≥200 °C [66]. Novel, volatile (fluoroalkythiolato) tin (IV) precursors have been synthesised and $(CF_3CH_2S)_4Sn$ used to deposit tin sulphide films under atmospheric pressure chemical vapour deposition (APCVD) conditions. Films deposited at temperatures 550 or 600 °C were found to be pure tin monosulfide phase [67].The CVD of tin sulphides has been previously reported by Price *et al*. using $SnCl_4$ and H_2S at temperature range of 300-545 °C [68]. At deposition temperatures of 545 °C pure single-phase SnS were obtained. Barone et al. deposited pure SnS thin films by aerosol-assisted chemical vapour deposition (AACVD) at 500 °C using a single source precursor $(PhS)_4Sn$ and H_2S as the co-reactant gas [69]. Zhang *et al*. reported the deposition of pure orthorhombic SnS films by CVD using $SnCl_4$ and H_2S at temperatures equal to or higher than 350 °C [70].

Radio Frequency (RF) Sputtering

While research groups are using a variety of deposition techniques for SnS, sputter deposition is known to produce high-quality films and is an easily scalable reliable and industrially proven process to manufacture thin films. Unfortunately, sputtering has not been explored sufficiently enough for SnS thin films. In the IEEE conference of the year 1994 Guang-Pu *et al*. reported a study of RF sputtering of tin sulphide for the first time [71] . Shinichi and Shigetoshi reported SnS thin-films reactively sputtered using a pure tin target and an H_2S/Ar gas mixture[72] .Years later Hartman *et al*. reported SnS thin-films sputtered using a SnS target by using argon plasma. They have found that the resistivity, stoichiometry, phase, grain size, shape, band gap, and the optical absorption coefficient can be varied by modifying argon pressure for a fixed deposition time in these films [73]. Banai *et al*. successfully deposited single phase SnS thin films from a SnS_2 target and SnS target [74, 75]. Lkuno *et al*. reported a SnS thin film solar cell device with conversion efficiency of 2.1% by RF magnetron sputtering by RF magnetron sputtering, followed by post-annealing treatment at temperatures ranging from 80 to 220 °C [76].

1.2.5 Overview of SnS Thin Film Solar Cells

Despite the efforts made recent last years in improving SnS-based solar cells, low efficiency values have been obtained, with the best value of 4.36 % reached in 2014 [65]. This section focuses on the progress on the record experimental efficiency of SnS solar cells over time. In 1988, Sharon and Basavaswaran reported a photo conversion efficiency of 0.6% for a photoelectrochemical cell (PEC) with the structure: n-SnS/Ce^{4+}/Ce^{3+}/Pt. SnS thin films were synthesised by passing H_2S through the solution of $SnCl_2$ [77]. Noguchi *et al*. successfully deposited SnS thin films by vacuum evaporation and fabricated SnS solar cells, where aITO/n- CdS/p-SnS/Ag cell was deposited. Although the synthesis was performed under vacuum only 0.29% of efficiency was achieved with a reported short-circuit current (J_{sc}) of 7 mA/cm^2 and an open circuit voltage (V_{oc}) of 0.12 V [78]. Later on in 1997, a study reported by Reddy *et al*. resulted in a device with a record efficiency of 0.5% [79]. More than a decade after, an improvement in the record efficiency was made by Reddy *et al*. in 2006 were synthesized by spray pyrolysis achieving a conversion efficiency of 1.3% [80]. Ghosh et al. fabricated a SnS/CdS heterojunction, where a CdC_{l2} -post treatment was applied to the CdS layer which resulted in an increment in the grain size. The efficiency values for the SnS solar cells with and without treatment were 0.08 and 0.05% respectively [81]. Avellanenda *et al*. investigated two different crystal structures of SnS: orthorhombic SnS and zinc-blend SnS. These films showed a p-type conductivity in a SnO2:F/CdS/SnS (ZB)/SnS (OR)/Ag structure. The devices showed low conversion efficiency, 0.2% [82]. Heterojunction solar cells were fabricated using sprayed with cadmium sulphide as the window layer with a structure of Mo/p-SnS/n-CdS/ZnO heterojunction by hot wall deposition method on the Mo-coated glass. The best junctions have an efficiency up to 0.5% where The main conclusion of this work concerns the benefits of using the hot wall deposition method to prepare the SnS layers instead of the standard vacuum evaporation technique [83]. One year later, an optimization of the SnS conduction band offset (CBO) as the light absorbing layer and Zn1-xMgxO as a window layer in SnS thin film solar cells was fabricated to improve the solar cell efficiency leading to a conversion efficiency of approximately 2.1% [76]. Hedge et al. synthesized SnS polycrystalline thin film by thermal evaporation technique in 2013. This research group reported the fabrication of heterojunction solar cells in superstrate configuration using SnS as an absorber layer and CdS:In as window layer. The solar cells with indium doped CdS window layer showed improved performance as compared to pure CdS window layer. The best device had a conversion efficiency of 0.4 % [84]. Most recently, Sinsermsukskal *et al*. fabricated a SnS heterojunction solar cell by vapour deposition with an optimised Zn(O,S) layer which exhibited an National Renewable Energy Laboratory (NREL) certified efficiency of 2.04% . Although the effective improvement in this work was optimising the band offset between Zn(O,S) and SnS to an optimum slightly positive value by increasing the sulfur content in Zn(O,S) [85]. As of the conclusion of this work the current SnS-based champion cell was processed by the same group. Steinmann *et al*. fabricated and optimized the previous device by Enhancing the efficiency of SnS solar cells via band-offset engineering with a zinc oxysulfide buffer layer of few nanometres at the SnS/Zn(O,S) interface, reaching an NREL-certified efficiency of 4.36% [86].

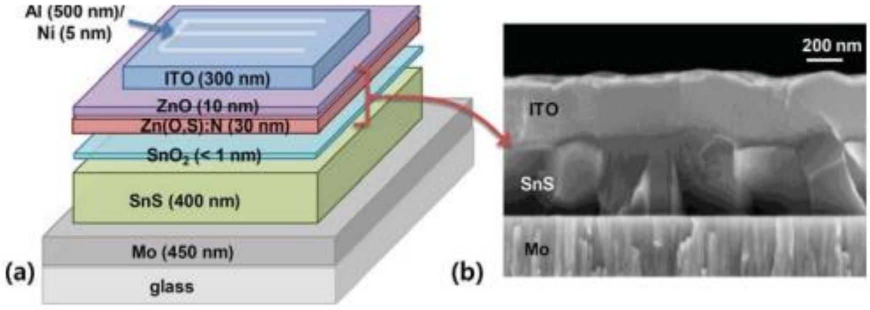

Figure 1.6 a) Schematic diagram of a SnS solar cell b) A cross section SEM image of a SnS solar cell [86].

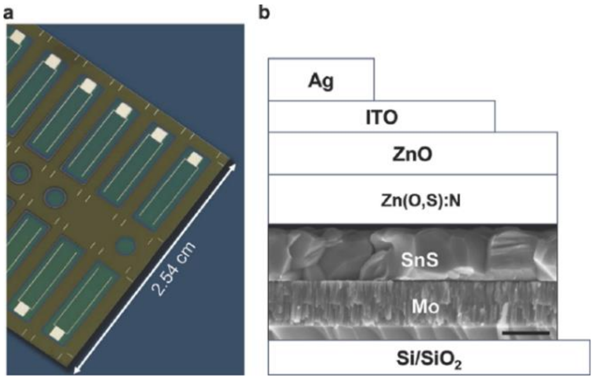

Figure 1.7 Schematic of SnS devices b) Schematic of cross section of SnS thin film solar cell [87].

1.2.6 Potential Causes of Low Efficiency of SnS Solar Cells

Despite the ideal properties of SnS as an absorber for PV application the highest efficiency obtained is still remarkably low compared to other absorbers such as CdTe and CIGS. This poor performance can be due to multiple possibilities, perhaps the likeliest of which is the formation of the alternate phases of SnS. Besides the formation of SnS phase, the secondary sulphide phases SnS_2 and Sn_2S_3 are often co-deposited. The incorporation of these secondary phases is undesired as they can result in changes in composition can result in conductivity type inversion, either p- or n-type thus causing detrimental for the p-n heterojunction formation [87]. Bulk recombination in SnS because of defects such as grain boundaries or intrinsic point defects such as sulphur vacancies that arise from the preparation methods can contribute to the poor efficiency. In addition to the quality of SnS, other main contributors to this poor efficiency are believed poor proper device optimization. The band alignment at the heterojunction between SnS and the buffer layer. For maximum conversion efficiency, heterojunction solar cells often have a “spike” type conduction band offset (CBO), in which the n-type buffer layer has a slightly higher energy at its conduction band minimum than does the p-type absorber layer. This spike CBO minimizes the recombination rate at the p-n junction [88]. It is not necessary to have a spike CBO to form an efficient heterojunction solar cell if the recombination velocity at the junction is low enough.

1.3 Aim of Work

The work presented in this thesis is an attempt towards the development of low cost-effective, eco-friendly absorber material for thin film solar cells using a simple economically viable deposition technique. In this thesis SnS thin films were deposited by two entirely different techniques that have been adopted for this purpose. First, a novel two step method using CVD was developed. Compositional, structural and electronic analyses of the synthesized SnS thin films, were performed, with the intent to uncovering some of the key fundamental properties. The key achievement of this work is that the films phase can be tuned by the post annealing treatment. Moreover, the main goal was showing the capability of our deposited films to be used in PV devices. Secondly, further this study has been extended and another approach to the deposition method has been applied to have a comparable study. SnS thin films were deposited by RF sputtering. A detailed study of the effects of the annealing conditions on the phase content of the tin sulphide films was achieved. This thesis concludes with a discussion of the important results found over the course of this project and suggestions for future work, to carry these conclusions forward.

1.4 Thesis structure

This thesis assesses two fabrication methods for high quality SnS thin films and device fabrication. The structure is organized as follows. **Chapter 1** is a general introduction to this thesis. It briefs the three generations of PV cell technologies depending on the materials used and the level of commercial maturity. Further it continues with discussion on the structure of SnS and phase diagram and the photovoltaic suitability of SnS. A review of various methods to deposit SnS is discussed. **Chapter 2** gives a basic introduction to the key physical principles to understanding the principles of operation of solar cell devices. Methods of depositions, characterisation and analysis of SnS thin films for this thesis is presented in **Chapter 3**. **Chapter 4** deals with the engineering of structural, optoelectronic and morphological properties of SnS by a novel two step CVD method. Supporting information for this chapter is available in Appendix A and B. Exploiting the potential of a new material for photovoltaic applications requires showing the capability of the material to be practically used in a working device. **Chapter 5** shows the fabrication steps for the p-n junctions fabricated by CVD and the electrical characterisation. **Chapter 6** describe the RF sputtering method used for depositing high quality SnS thin films via a two-step process. **Chapter 7** gives a description of the device fabrication and characterisation of RF sputtered films. This thesis concludes with a discussion of the important results found over the course of this project and suggestions for future work in **Chapter 8**, in order to carry these conclusions forward.

1.5 References

[1] A. E. Becquerel, "“Memoire sur les effets ´ electriques produits ´sous l’influence des rayons solaires," *Comptes Rendus des Seances Hebdomadaires,* vol. 9, pp. 561–567, 1839.

[2] M. D. A. a. R.Hill, *Clean Electricity from Photovoltiacs*. Chichester, UK, 2001.

[3] D. C. Reynolds, G. Leies, L. L. Antes, and R. E. Marburger, "Photovoltaic Effect in Cadmium Sulfide," *Physical Review,* vol. 96, pp. 533-534, 10/15/ 1954.

[4] M. A. Green, *Clean Electricity from Photovoltaics*. Hackensack N.J.: World Scientific Publishing Co., 2001.

[5] Y. W. Yoshikawa K, Irie T, Kawasaki H, Konishi K, Ishibashi H and Yamamoto K, "Exceeding conversion efficiency of 26% by heterojunction interdigitated back contact solar cell with thin film Si technology," *Solar Energy Materials & Solar Cells,* vol. 173, pp. 37-42, 2017.

[6] S. M. Masuko K, Hashiguchi T, Fujishima D, Kai M, Yoshimura N and Yamanishi T, "Achievement of more than 25% conversion efficiency with crystalline silicon heterojunction solar cell," *(IEEE) Journal of Photovoltaics,* vol. 4, pp. 1433-1435, 2014.

[7] A. N. Nakamura J, Hieda T, Okamoto C, Katayama H and Nakamura K, "Development of heterojunction back contact Si solar cells," *(IEEE) Journal of Photovoltaics,* vol. 4, pp. 1491-1495, 2014.

[8] H. J. Q. W. Shockley, "Detailed Balance Limit of Efficiency of p-n Junction Solar Cells," *Journal of Applied Physics,* vol. 32, pp. 510-519, 1961.

[9] L. M. Peter, "Towards sustainable photovoltaics: the search for new materials., Philosophical Transactions. Series A," *Mathematical, Physical, and Engineering Sciences,* vol. 369, pp. 1840–1856, 2011.

[10] K. E. M.A. Green, Y. Hishikawa, W. Warta, E.D. Dunlop, "Solar cell efficiency tables (version 42).pdf," *Progress in Photovoltaics : Research and Applictions,* vol. 21, pp. 827–837, 2013.

[11] K. L. Chopra, Paulson, P. D. and Dutta, V., "Thin-film solar cells: an overview," *Progress in Photovoltaics: Research and Applications,* vol. 12, pp. 69-92, 2004.

[12] C. R. W. a. D. E. Carlson, *Clean Electricity from Photovoltaics (Series on Photoconversion of Solar Energy* vol. 1. London: London: Imperial College Press, 2001.

[13] e. a. S. Amirudden, presented at the Technical Digest of the 14th International Photovoltaic Science and Engineering Conference (PVSEC-14), Bangkok, Thailand, 2004.

[14] R. e. t. C. A. S. S. Photovoltaics, ed, 2012.

[15] D. L. S. a. C. R. Wronski, "Reversible Conductivity Changes in Discharge-Produced Amorphous Si," *Applied Physics Letters,* vol. 31, pp. 292-294, 1977.

[16] Y. Yan and M. M. Al-Jassim, "Transmission electron microscopy of chalcogenide thin-film photovoltaic materials," *Current Opinion in Solid State and Materials Science,* vol. 16, pp. 39-44, 2012.

[17] J. J. Lofersk, "Theoretical Considerations Governing the Choice of the Optimum Semiconductor for Photovoltaic," *Journal of Applied Physics,* vol. 27, pp. 777-784, 1956.

[18] J. J. Loferski, in *Proceedings of the 12th IEEE Photovoltaics Specialists Conference*, New York, USA, 1976, p. 853.

[19] J. J. L. N.A. Gokcen, *Solar Energy Materials and Solar Cells,* vol. 1, pp. 271-286, 1979.

[20] R. H. B. D, "New results on the development of a thin film p-CdTe–n-CdS heterojunction solar cell," in *Proceedings of the 9th IEEE Photovoltaics Specialists Conference*, New York, 1972, pp. 129-131.

[21] J. C. K. X. Wu, R.G. Dhere, C. DeHart, D.S.. Albin, A.Duda, T.A. Gessert, S. Asher, D.H. Levi and P. Sheldon, "16.5%-Efficient CdS/CdTe polycrystalline Film Solar Cel," in *In: Proceedings of the 17th European Photov. Solar Energy Conf*, Munich, Germany, 2001, p. 995.

[22] "First Solar builds the highest efficiency thin film PV cell on record," ed: First Solar Media, August 5,2014.

[23] M. J. de Wild-Scholten, "Energy payback time and carbon footprint of commercial photovoltaic systems," *Solar Energy Materials and Solar Cells,* vol. 119, pp. 296-305, 2013.

[24] F. R. W. a. G. K. M. L. L. Kazmerski, "Thin-film $CuInSe_2$/CdS heterojunction solar cells," *Appllied Physical Letters,* vol. 29, pp. 268–269, 1976.

[25] R. A. M. a. W. S. C. W. E. Devaney, presented at the Proc. 18th IEEE Photovoltaic Specialists Conference, 1985.

[26] S. F. P. Release, "Solar Frontier Sets Thin-Film PV World Record with 22.3 % CIS Cell," ed: Online, http://www.solar-frontier.com/eng/news/2015/C051171.html (accesed January 2016), 2015.

[27] M. A. Contreras, Mansfield, Lorelle M., Egaas, Brian, Li, Jian, Romero, Manuel, Noufi, Rommel, Rudiger-Voigt, Eveline and Mannstadt, Wolfgang, "Wide bandgap Cu(In,Ga)Se_2 solar cells with improved energy conversion efficiency," *Progress in Photovoltaics: Research and Applications,* vol. 20, pp. 843-850, 2012.

[28] I. Repins, Contreras, Miguel A., Egaas, Brian, DeHart, Clay, Scharf, John, Perkins, Craig L., To, Bobby and Noufi, Rommel, "19.9%-efficient ZnO/CdS/CuInGaSe_2 solar cell with 81.2% fill factor," *Progress in Photovoltaics: Research and Applications,* vol. 16, pp. 235-239, 2008.

[29] C. H. L. Goodman, "The prediction of semiconducting properties in inorganic compounds," *Journal of Physics and Chemistry of Solids,* vol. 6, 1958.

[30] "Solibro beats world record for solar cells," ed: Solibro Press Release, 2014.

[31] M. Green, "The path to 25% silicon solar cell efficiency: History of silicon cell evolution. Progress in Photovoltaics: Research and Applications," vol. 17, pp. 183-189, 2009.

[32] U. S. D. o. Energy, *Critical material strategy,* December 2010.

[33] S. Delbos, "Kësterite thin films for photovoltaics: a review," presented at the EPJ Photovoltaics 3, 2012.

[34] D. B. G. Mitzi, O.; Todorov, T. K.; Wang, K.; Guha, S, "The path towards a high-performance solution-processed kesterite solar cell," *Solar Energy Materials & Solar Cells,* vol. 95, p. 1421−1436, 2011.

[35] W. Wang, M. T. Winkler, O. Gunawan, T. Gokmen, T. K. Todorov, Y. Zhu*, et al.*, "Device Characteristics of CZTSSe Thin-Film Solar Cells with 12.6% Efficiency," *Advanced Energy Materials,* vol. 4, pp. n/a-n/a, 2014.

[36] H. Katagiri, Jimbo, K., Maw, W. S., Oishi, K.; Yamazaki, M., Araki, H., Takeuchi A., "Development of CZTS-based thin film solar cells

" *Thin Solid Films,* vol. 517, p. 2455−2460, 2009.

[37] C. S. F. T.M. Razykov, D. Morel, E. Stefanakos, H.S. Ullal, H.M. Upadhyaya, "Solar photovoltaic electricity: Current status and future prospects," *Solar Energy,* vol. 85, pp. 1580–1608, 2011.

[38] M. Grätzel, "Solar energy conversion by dye-sensitized photovoltaic cells," *Inorganic Chemistry,* vol. 44, pp. 6841–6851, 2005.

[39] M. B. J. M. Liu, H.J. Snaith, "Efficient planar heterojunction perovskite solar cells by vapour deposition," *Nature,* vol. 501, pp. 304–312, 2013.

[40] R. Herzenberg, *Rev. Mineral* vol. 4, 1932.

[41] R. G. E. D. J. Payne, A. Walsh, G. W. Watson, J. Guo, P.-A. Glans, T. Learmonth, and K. E. Smith, "Electronic Origins of Structural Distortions in Post-Transition Metal Oxides: Experimental and Theoretical Evidence for a Revision of the Lone Pair Model," *Phys. Rev. Lett.,* vol. 96, 2006.

[42] M. D. N. Koteeswara Reddy, M. Prashantha, K. Ramesh, and K.R. Gunasekhar, "In situ structural studies on orthorhombic SnS micro-crystals," *The European Physical Journal Applied Physics,* vol. 60, 2012.

[43] J. H. P. Sinsermsuksakul, W. Noh, A.S. Hock, and R.G. Gordon, "Atomic Layer Deposition of Tin Monosulfide Thin Films," *Advanced Energy Materials,* vol. 1, 2011.

[44] H. G. W. von Schnering, "The high temperature structure of .BETA.-SnS and .BETA.-SnSe and the B16-to-B33 type .LAMBDA.-transition path.," *Cryst. Mater.,* vol. 156, pp. 143-150, 1981.

[45] A. N. C. Mariano, K. L, "Polymorphism in some IV-VI compounds induced by high pressure and thin-film epitaxial growth," *Appl. Phys. Lett,* vol. 10, 1967.

[46] M. T. S. N. a. P. K. N. David Avellaneda, "Polymorphic Tin Sulfide Thin Films of Zinc Blende and Orthorhombic Structures by Chemical Deposition," *Journal of The Electrochemical Society,* vol. 155, 2008.

[47] S. S. Rabkin Alexander, Abutbul Ran E., Ezersky Vladimir,Meshi Louisa and Golan Yuval, "New Nanocrystalline Materials: A Previously Unknown Simple Cubic Phase in the SnS Binary System," *Nano Letters,* vol. 15, pp. 2174-2179, 2015/03/11 2015.

[48] J. M. Skelton, Burton, Lee A. Oba, Fumiyasu and Walsh, Aron, "Chemical and Lattice Stability of the Tin Sulfides," *The Journal of Physical Chemistry C,* vol. 121, pp. 6446-6454, 2017/03/30 2017.

[49] H. Pelabon, Moissan, M. H., "On the sulfides, selenides and tellurides of tin," *Compt. Rend,* vol. 142, pp. 1147-1149, 1906.

[50] W. B. W. Mecklenburg, "Über die Zustandsdiagramme von Zinn mit Schwefel, Selen und Tellur," *Zeitschrift fur Anorg. nd Alg. Chemie,* vol. 64, pp. 226-235, 1906.

[51] C. H. W. Albers, and F. van der Maesen, "The preparation and the electrical and optical properties of SnS crystals," *Journal of Physics and Chemistry of Solids,* vol. 15, 1960.

[52] R. C. Sharma, Chang, Y. A., "The S−Sn (Sulfur-Tin) system," *Bulletin of Alloy Phase Diagrams,* vol. 7, pp. 269-273, June 01 1986.

[53] G. Lindwall, Shang, ShunLi, Kelly, Neal R., Anderson, Tim and Liu, Zi-Kui, "Thermodynamics of the S–Sn system: Implication for synthesis of earth abundant photovoltaic absorber materials," *Solar Energy,* vol. 125, pp. 314-323, 2016/02/01/ 2016.

[54] B. Meyer, "Elemental sulfur," *Chemical Reviews,* vol. 76, pp. 367-388, 1976/06/01 1976.

[55] W. A. C. H. F. v. d. Maesen, "The preparation and the electrical and optical properties of SnS crystals," *J. Phys. Chem. Solids,* vol. 15, pp. 306-310, 1960.

[56] K. T. Ramakrishna Reddy, N. Koteswara Reddy, and R. W. Miles, "Photovoltaic properties of SnS based solar cells," *Solar Energy Materials and Solar Cells,* vol. 90, pp. 3041-3046, 2006/11/23/ 2006.

[57] N. Koteswara Reddy and K. T. Ramakrishna Reddy, "Growth of polycrystalline SnS films by spray pyrolysis," *Thin Solid Films,* vol. 325, pp. 4-6, 1998/07/18/ 1998.

[58] R. A. k. B.G. Jeyaprakash1, K.Kesavan and A. Amalarani, "STRUCTURAL AND OPTICAL CHARACTERIZATION OF SPRAY DEPOSITED SnS THIN FILM " *Journal of American Science* vol. 6, pp. 22-26, 2010.

[59] R. C. a. J. Drowart, "Thermodynamic Study of Tin Sulfide and Lead Sulfide Using a Mass Spectrometer," *The Journal of Chemical Physics,* vol. 37, 1962.

[60] M. Devika, K. T. Ramakrishna Reddy, N. Koteeswara Reddy, K. Ramesh, R. Ganesan, E. S. R. Gopal*, et al.*, "Microstructure dependent physical properties of evaporated tin sulfide films," *Journal of Applied Physics,* vol. 100, p. 023518, 2006.

[61] K. T. R. R. P.A.Nwofe, J.K.Tan,I.Forbes and R.W. Miles, "Onthe structural and optical properties of SnS films grown by thermal evaporation method," presented at the J.Phys.Conf., 2013.

[62] J. Y. a. G. Kim, Steven M., "Tin Monosulfide Thin Films Grown by Atomic Layer Deposition Using Tin 2,4-Pentanedionate and Hydrogen Sulfide," *The Journal of Physical Chemistry C,* vol. 114, pp. 17597-17603, 2010/10/21 2010.

[63] G. Ham, Shin, Seokyoon, Park, Joohyun, Choi, Hagyoung, Kim, Jinseo, Lee, Young-Ahn, Seo, Hyungtak and Jeon, Hyeongtag, "Tuning the Electronic Structure of Tin Sulfides Grown by Atomic Layer Deposition," *ACS Applied Materials & Interfaces,* vol. 5, pp. 8889-8896, 2013/09/25 2013.

[64] K. H. P. Sinsermsuksakul, S. B. Kim, J. Heo, L. Z. Sun, H. H. Park, R. Chakraborty, T. Buonassisi and R. G. Gordo, "Enhancing the efficiency of SnS solar cells via band-offset engineering with a zinc oxysulfide buffer layer," *Appl. Phys. Lett,* vol. 102, 2013.

[65] L. S. P. Sinsermsuksakul, S.W. Lee, H.H. Park, S.B. Kim, C. Yang and R.G. Gordon,, "Overcoming Efficiency Limitations of SnS-Based Solar Cells," *Advanced Energy Materials,* vol. 4, 2014.

[66] A. Ortiz, J. C. Alonso, M. Garcia, and J. Toriz, "Tin sulphide films deposited by plasma-enhanced chemical vapour deposition," *Semiconductor Science and Technology,* vol. 11, p. 243, 1996.

[67] T. G. Hibbert, M. F. Mahon, K. C. Molloy, L. S. Price, and I. P. Parkin, "Deposition of tin sulfide thin films from novel, volatile (fluoroalkythiolato)tin(iv) precursors," *Journal of Materials Chemistry,* vol. 11, pp. 469-473, 2001.

[68] L. S. Price, I. P. Parkin, M. N. Field, A. M. E. Hardy, R. J. H. Clark, T. G. Hibbert*, et al.*, "Atmospheric pressure chemical vapour deposition of tin(ii) sulfide films on glass substrates from $Bun_3SnO_2CCF_3$ with hydrogen sulfide," *Journal of Materials Chemistry,* vol. 10, pp. 527-530, 2000.

[69] T. G. H. G. Barone, M. H. Mahon, K. C. Molloy, L. S. Price, I. P.Parkin, A. M. E. Hardy, M. N. Field, *Journal of Materials Chemistry,* vol. 11, p. 464±468, 2000.

[70] H. Zhang, Y. Balaji, A. Nalin Mehta, M. Heyns, M. Caymax, I. Radu*, et al.*, "Formation mechanism of 2D SnS2 and SnS by chemical vapor deposition using SnCl4 and H2S," *Journal of Materials Chemistry C,* vol. 6, pp. 6172-6178, 2018.

[71] Z. Z.-L. W. Guang-Pu, Z. Wei-Ming, G. Xiang-Hong, C. Wei-Qun, H. Tanamura, M. Yamaguchi, H. Noguchi, T. Nagatomo, O. Omoto, in *1st IEEE World Conference on Photovoltaic Energy Conversion*, Honolulu, USA, 1994.

[72] S. S. K. Shinichi, 9 July 1996.

[73] J. L. J. K. Hartman, M.I. Bertoni, D. Recht, M.J. Aziz, M.A. Scarpulla, *Thin Solid Films,* vol. 519 pp. 7421–7424, 2011.

[74] R. E. Banai, J. C. Cordell, G. Lindwall, N. J. Tanen, S.-L. Shang, J. R. Nasr*, et al.*, "Control of Phase in Tin Sulfide Thin Films Produced via RF-Sputtering of SnS2 Target with Post-deposition Annealing," *Journal of Electronic Materials,* vol. 45, pp. 499-508, January 01 2016.

[75] H. L. R. E. Banai, M. A. Motyka, R. Chandrasekharan, N. J. Podraza, J. R. S. Brownson and M. W. Horn, "Optical Properties of Sputtered SnS Thin Films for Photovoltaic Absorbers," *IEEE Journal of Photovoltaics,* vol. 3, pp. 1084-1089, 2013.

[76] R. S. Takashi Ikunoa), Kosuke Kitazumi, Naoko Takahashi, Naohiko Kato, and Kazuo Higuchi, "SnS thin film solar cells with $Zn_{1-x}Mg_xO$ buffer layers," *Applied Physical Letters,* vol. 102, 2013.

[77] K. B. M. Sharon, " Photoelectrochemical behaviour of tin monosulphide," *Sol. Cells,* vol. 25, pp. 97–107 1988.

[78] A. S. H. Noguchi, H. Tanamura, T. Nagatomo and O. Omoto *Sol. Energy Mater. Sol. Cells,* vol. 35, 1994.

[79] N. Koteswara Reddy and K. T. Ramakrishna Reddy, "Tin sulphide films for solar cell application," in *Photovoltaic Specialists Conference, 1997., Conference Record of the Twenty-Sixth IEEE*, 1997, pp. 515-518.

[80] N. K. R. K.T.R. Reddy, R.W. Miles, *Sol. Energy Mater. Sol. Cells,* vol. 90, p. 3041, 2006.

[81] M. D. B. Ghosh, P. Banerjee and S. Das,, *Energy Mater. Sol. Cells,* vol. 92, 2008.

[82] B. K. D. Avellaneda, T.K. Das Roy, G.A. Castillo and S. Shaji,, *J.Mater.Sci.Mater.Electron.,* vol. 110, pp. 667-672, 2013.

[83] S. A. Bashkirov, Gremenok, V. F., Ivanov, V. A., Lazenka, V. V. and Bente, K., "Tin sulfide thin films and Mo/p-SnS/n-CdS/ZnO heterojunctions for photovoltaic applications," *Thin Solid Films,* vol. 520, pp. 5807-5810, 2012/06/30/ 2012.

[84] S. S. Hegde, Kunjomana, A. G. ,Prashantha, M., Kumar, C. and Ramesh, K., "Photovoltaic structures using thermally evaporated SnS and CdS thin films," *Thin Solid Films,* vol. 545, pp. 543-547, 2013/10/31/ 2013.

[85] K. H. Prasert Sinsermsuksakul, Sang Bok Kim, Jaeyeong Heo , Leizhi Sun, Helen Hejin Park Rupak Chakraborty, Tonio Buonassisi, and Roy G. Gordon and H. Affiliations, "Enhancing the efficiency of SnS solar cells via band-offset engineering with a zinc oxysulfide buffer layer," *Applied Physical Letters,* vol. 102, 2013.

[86] L. S. P. Sinsermsuksakul, S.W. Lee, H.H. Park, S.B. Kim, C. Yang and R.G. Gordon, " Overcoming Effi ciency Limitations of SnS-Based Solar Cells " *Advanced Energy Materials,* vol. 4, 2014

[87] J. Vidal, S. Lany, M. d'Avezac, A. Zunger, A. Zakutayev, J. Francis*, et al.*, "Band-structure, optical properties, and defect physics of the photovoltaic semiconductor SnS," *Applied Physics Letters,* vol. 100, p. 032104, 2012.

[88] M. B. Alex Niemegeers, and Alexis De Vos, "On the CdS/CuInSe2 conduction band discontinuity," *Applied Physics Letters,* vol. 67, pp. 843-845, 1995.

Chapter 2 Principles and Operation of Photovoltaic Solar Cells

2.1 Introduction

Photovoltaics deals with the conversion of sunlight into electrical energy. Practically all PV devices, such as solar cells incorporate a pn-junction in which the photovoltage is developed. To obtain high-efficiency solar cells involves a wide range of knowledge of solar radiation reaching the earth, fundamental operation of solar cell, materials that are able to exhibit photovoltaic characteristics, etc. Detailed information and understanding of the basics of PV technology will be discussed briefly in this section.

2.2 The Solar Spectrum

Solar energy is simply energy based on the sun's electromagnetic radiation comprising electromagnetic radiation of various wavelengths or frequencies. The energy of solar radiation is directly utilised in solar cells that convert this energy into electricity, which is referred as photovoltaic conversion. Solar energy is incident on the earth as a spectrum of photons with a range of energies which are determined by the properties of the sun.

The sun can be approximated to a black body radiator operating at an effective temperature of 5777 K [1]. The rate of energy received from the sun by earth on its unit surface area is 1.353 kW/m^2, this quantity is called solar constant. Once the light has left the sun’s surface, it travels through atmosphere and gets attenuated due to absorption and scattering by the molecules and particles present in the atmosphere. The degree of this attenuation (the reduction in the power of light) is quantified by an important parameter called the “air mass”. The air mass (AM) is defined as the amount of atmosphere which solar radiation must pass through to reach the surface of the earth and depends on the position of the sun. It is an indicator of the distance travelled by solar radiation in the earth’s atmosphere. This is simple defined as the ratio of the optical path length (L) of the solar spectrum through the atmosphere to the vertical path length (L_o) normal to the earth’s surface at sea level when the sun is at the zenith as shown in Figure 2.1.

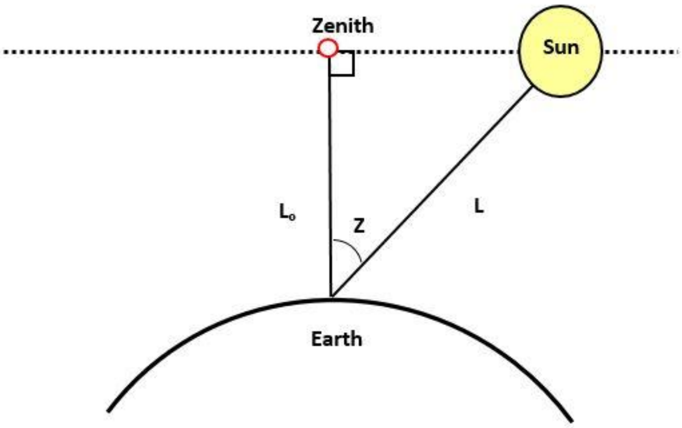

Figure 2.1 Schematic of the sun's position for determination of air mass (AM).

Then,

$$AM = \frac{L}{L_o} \approx \frac{1}{\cos Z} \qquad \text{eq. 2.1}$$

where, the ratio $\frac{L}{L_o}$ is called the air mass coefficient (AM) and where Z is the angle between the zenith and the position of the sun at the time in question. Because Z varies with time of the day and seasons of the year, the air mass varies, depending on the sun's elevation and with the position of the observer on the Earth's surface. AM1.0 refers to the spectrum that has travelled through the atmosphere when the sun is directly at its zenith above the point on the Earth under consideration. The AM1.5 spectrum is the most widely used in terrestrial standard for evaluating solar cells. It is the solar spectral irradiance distribution incident at sea level from the sun at 48.2 °.

2.3 Photovoltaic Concepts

2.3.1 PN Junction

Solar cells essentially work by utilising the PV effect. This is where incident sunlight is directly converted into electricity by a p-n semiconductor junction [2]. The p-n junction essentially arises when a p-type semiconductor material is brought into contact with a n-type semiconductor material meet. A p-type semiconductor has a high concentration of holes and a n-type semiconductor has a high concentration of electrons. Free electrons from the n-type region and free holes from the p-type region diffuse across the junction when they are brought in contact. At the junction, recombination takes place when an electron meets a hole and as a result it becomes depleted. The diffusion of electrons leaves positively charged ionised donors on the n-side and on the p-side negatively charged ionised acceptors are left behind after the diffusion of holes. The positive and negative ions create an electric field which leads to drift of electrons and holes until the diffusional fluxes are cancelled out. Eventually, the p-n junction reaches a steady state condition that is charge neutral but has a built in electric field. This built in electric field is the key to capturing the solar radiation incident on the junction and converting it to usable electricity. Figure 2.2shows the schematic diagram of a simple p-n junction and formation of a built-in field.

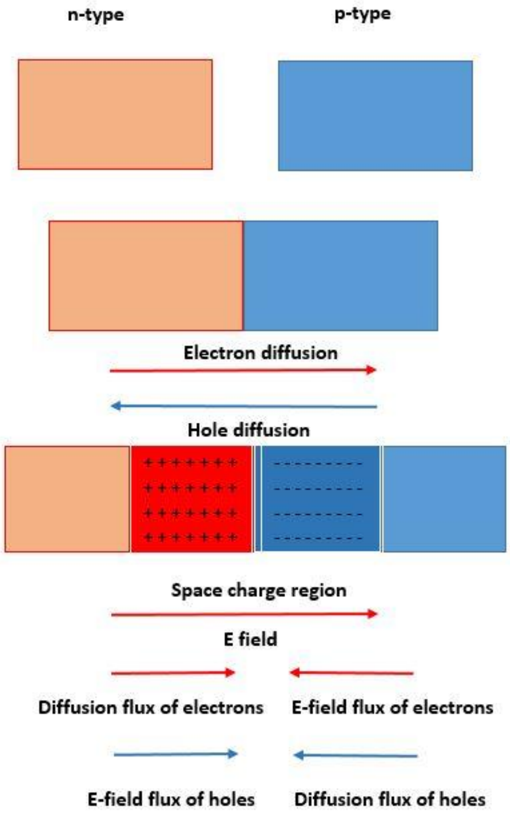

Figure 2.2 The formation of a p-n junction. A p-type and an n-type semiconductor in contact resulting in diffusion flux of charged carriers and formation of a built in field.

When p-type and n-type semiconductors are in contact, three things happen:

(a) Fermi level line up
(b) Potential barrier develops
(c) Electrical field sets up

The difference in the potential energy of electrons at the two sides of the junction, the built-in potential, V_{bi}, are given by:

$$V_{bi} = \frac{kT}{q} \ln \left[\frac{N_A N_D}{n_i^2} \right] \qquad \text{eq. 2.2}$$

where k is the Boltzmann constant, T is the temperature, q is the magnitude of electronic charge, N_A is the acceptor concentration on the p-side, N_D is the donor concentration in the n-side and n_i is the intrinsic charge carrier density and:

$$w = \left[\frac{2\varepsilon}{q}\left(\frac{N_A+N_D}{N_A N_D}\right)V_{bi}\right]^{\frac{1}{2}} \qquad \text{eq. 2.3}$$

where w is the width of the depletion layer.

2.3.2 Dark Forward I-V Characteristics of Solar Cells

The I–V characteristics of solar cells measured under dark and illuminated conditions provide an important tool for the assessment of their performance. The dark characteristics are the easiest way to estimate the quality of the diode.

The typical dark I–V relationship for a diode is given by:

$$I = I_o(\exp\left(\frac{V - IR_s}{nV_T}\right) - 1) \qquad \text{eq. 2.4}$$

where I_o is the reverse saturation current, R_s is the series resistance, n is the diode ideality factor and V_T is the thermal voltage:

$$V_T = \frac{k_B T}{q} \qquad \text{eq. 2.5}$$

The above equation is for a single p–n junction diode.

2.3.3 Light Absorption and Carrier Generation

The key property of each solar cell is its capability to absorb effectively the wide spectrum of photons contained in solar radiation. This feature depends on the incident energy spectrum and optical and electronic properties of semiconductor material used as an absorber layer in a PV device [3].

The light excites an electron from the valence band to the conduction band, creating an electron-hole pair. Due to the built in electric field, the electron (negatively charged) will flow down the potential gradient while the hole flows up it (positively charged), creating a current under steady state illumination. By placing a load between these two charge carriers, it is then possible to extract usable electrical power from the junction. The absorption of a particular semiconductor is determined by its bandgap. Photons with energy greater than the bandgap can be absorbed, exciting an electron from the valence band (VB) to the conduction band (CB) or a higher energy state. Photons with energy less than the bandgap can in general not be absorbed, as there is no state suitable for an electron to be excited from the VB into. Therefore, solar cells typically can only absorb usefully light below a certain wavelength. It then may appear as though the smallest bandgap possible would be ideal, but this is not the case: photons excited to states higher than the CB will rapidly thermalize back down to the CB due to energetic considerations; the excess energy will simply be lost as heat. This is shown schematically in Figure 2.3, photons with energy lower than E_g cannot promote an electron and so are not absorbed (left). Photons with energy = E_g promote an electron with no energy wastage, leaving a hole in the valence band (centre). Photons with energy > E_g promote an electron to a higher state, which then rapidly thermalizes to the band edge, losing the excess energy as heat (right).

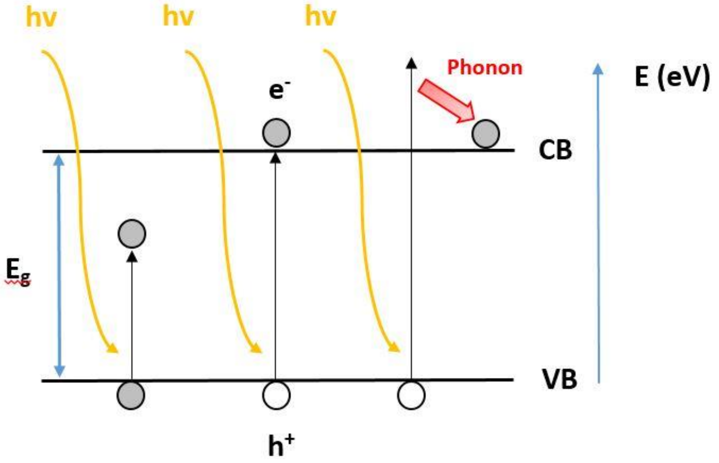

Figure 2.3 Photon absorption in a semiconductor.

In addition to having a bandgap that will allow absorption of photons, it is also important to know the absorption coefficient of the material at particular energies and how effectively photons are absorbed per unit length in the material. Optical absorption can be intrinsic, when energy of each absorbed photon is consumed by raising an electron from the valence band to the conduction band thereby creating an electron-hole pair or extrinsic in which case absorption is via deep localised states. Intrinsic absorption occurs in both direct and indirect bandgap materials. In direct bandgap materials the CB minimum and VB maximum occur at the same value of crystal momentum, 'k' and momentum is conserved when an electron is promoted from the top of the VB to the bottom of the CB. For photon energies hv just above the funemntal edge, the absorption coefficient $\alpha(hv)$ is given by Tauc law for direct allowed transition [4]:

$$\alpha(hv) = B(hv - E_g)^n \qquad \text{eq. 2.6}$$

where B is an energy-independent constant that depends on the material [5]. The exponent n indicates the type of electronic transition responsible for the absorption, n=1/2, 2, 3/2 and 3 corresponds to the direct allowed transition, indirect allowed transition, forbidden transition and indirect forbidden transitions, respectively.

The optical bandgap can be depicted as a barrier beyond which an exciton will gain enough energy jumping from the valence band to the conduction band by absorbing a photon. Exciton is an electron and a hole combined together to form a neutral pair by Coulomb interaction.

2.3.4 Heterojunctions

In a p-n junction, the semiconductor used for the p-type and n-type parts is usually the same material that is doped with p and n dopants. The solar cells discussed in this work are heterojunctions rather than homojunctions. A heterojunction is created by combining p-type and n-type semiconductors that are not the same material. Real solar cells are more complicated and cannot be represented simply by a p-n junction. They are measured under illumination, have other factors that contribute to power losses and are represented by the more complicated circuit. This will be discussed briefly in the next section.

2.3.5 Current Density-Voltage Characteristics of Photovoltaic Devices

In its simplest form, a solar cell can be described as a light absorbing material connected to an external circuit in an asymmetrical manner, allowing physical separation of photoexcited charge carriers to generate current and voltage.

At the core of photovoltaic operation is the generation of current and voltage under illumination. The current produced when the two terminals are connected (i.e. the voltage between them is zero) is known as the short-circuit current (I_{sc}); the voltage when the terminals are isolated (i.e. there is no current flow) is known as the open-circuit voltage (V_{oc}). For an intermediate load connected with resistance R, the cell will produce a voltage V (between 0 and V_{oc}) and a current I (between 0 and I_{sc}), where the current-voltage relation I(V) is described by the current-voltage characteristics of the solar cell under that specific illumination. Hence, the current-voltage characteristic of a particular solar cell determines its functionality and is the most important metric when characterising a photovoltaic device. Typically, currents (I) are expressed as current densities (J) as the current is generally proportional to area of device.

The amount of current that can be generated by a given solar cell depends on the incident light spectrum and the amount of this light that the solar cell can absorb. The absorption of a particular semiconductor is determined by its bandgap. Photons with energy greater than the bandgap can be absorbed, exciting an electron from the VB to the CB or a higher energy state. Photons with energy less than the bandgap can in general not be absorbed, as there is no state suitable for an electron to be excited from the VB into. Therefore, solar cells typically can only absorb usefully light below a certain wavelength. It then may appear as though the smallest bandgap possible would be ideal, but this is not the case: photons excited to states higher than the CB will rapidly thermalize back down to the CB due to energetic considerations; the excess energy will simply be lost as heat.

In addition to this photogenerated current, when a solar cell is under load it generates a voltage. The potential difference between electrodes provided by this voltage causes some current to flow in the opposite way to the photocurrent, i.e. in the wrong way compared to useful current generation. In the case of the open-circuit voltage, this reverse current would equal the forwards photocurrent, providing a net zero current. Since the photovoltaic device will exhibit this reverse current even in the dark, with no photogenerated current, it is termed the 'dark current'. Most photovoltaic devices behave like a diode in the dark, as a consequence of the asymmetry mentioned earlier that is necessary to achieve charge separation and collection. Thus, the dark current normally follows an ideal diode equation [6]:

$$J_{dark} = J_o(e^{\frac{qV}{k_B T}} - 1) \qquad \text{eq. 2.7}$$

Where J_o is a constant, J_{dark} represents the diode dark current that is a reverse current that opposes and therefore reduces the generated photocurrent, k_B is Boltzmann's constant and T is the temperature in Kelvin. The net current under illumination can then be approximated as a superposition of the performance in (reverse) dark current and the (forwards) short circuit photocurrent. This becomes, for an ideal diode,

$$J = J_{SC} - J_o(e^{\frac{qV}{k_B T}} - 1) \qquad \text{eq. 2.8}$$

Realistically however, under bias, parasitic resistances have a significant effect on the current-voltage characteristics. These are generally split into two types of resistance: series resistance and shunt resistance. Series resistance (R_S) arises from resistance of the cell materials to current flow and from contact resistance, Figure 2.4.

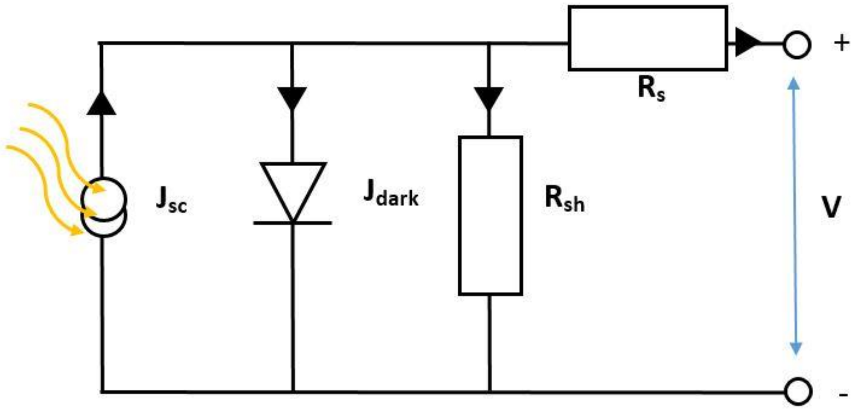

Figure 2.4 Schematic of solar cell equivalent circuit diagram.

This is particularly a problem at high charge densities or high illumination levels. Shunt, or recombination, resistances (R_{sh}) arise due to leakage channels such as pinholes and recombination at badly selective contacts causing shunt between contact terminals. Furthermore, the ideal diode behaviour is not often seen in real materials; a more realistic approach is to include an ideality factor m in the diode equation, representing a different dependence of current on bias. This arises due to additional recombination mechanisms in different materials.

We can add all these modifications into the diode equation, to now get a realistic current-voltage dependence for a solar cell:

$$J = J_{SC} - J_o\left(e^{\frac{qV}{k_B T}} - 1\right) - \frac{V + JAR_s}{R_{sh}} \qquad \text{eq. 2.9}$$

where J_{sc} represents the current generated from absorbed photons and A is the area of the device. This current voltage relation can now well describe the behaviour of most solar cells. This equation can be more intuitively represented by an electrical circuit diagram, which is shown in Figure 2.3. There is a current generation source, related to the semiconductor photoexciting charge, a diode in parallel, related to the asymmetry within the device that is necessary to extract charge selectively, and resistors in parallel and series representing the shunt and series resistances respectively.

A typical current-voltage (JV) relation for a real solar cell measured in the light and dark is shown in Figure 2.5.

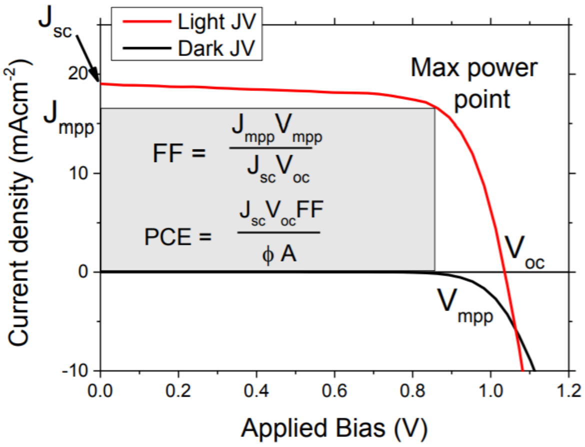

Figure 2.5 Current-Voltage (I-V) curve for photovoltaic device under illumination (red) and in dark (black)) [6].

The previously defined short-circuit current, defined as positive, is observed where the light curve intersects V=0, and the open-circuit voltage where J=0. The photovoltaic device is producing power in the whole region where J and V are positive, in the standard convention. Power density is given by P=JV; the point at which this product is maximum is called the maximum power point. This power (P_{mpp}) occurs at a particular voltage V_{mpp} and current density J_{mpp}. The ratio of this product to the theoretically ideal power $J_{sc} \times V_{oc}$ is defined as the fill factor (FF), which describes the sharpness of the JV curve, representing the severity of resistive and recombination losses:

$$FF = \frac{J_{mpp}V_{mpp}}{J_{sc}V_{oc}} \qquad \text{eq. 2.10}$$

This leads on to the essential value of solar cells, which is the solar cell power conversion efficiency.. The power conversion efficiency (PCE or η) is a measure of how well a solar cell converts the power of sunlight into usable electrical power. It is defined as the ratio of the power density produced to the power density of the incident light (P_I):

$$PCE\ (\eta) = \frac{J_{sc}V_{oc}FF}{P_I} \qquad \text{eq. 2.11}$$

From these equations we can identify several factors that affect the resulting efficiency of solar devices. The dark saturation current, dictated by recombination of charge carriers before they can be collected, decreases the V_{oc} and consequently the device efficiency. To maximize cell efficiency, a device design that minimizes bulk and surface recombination while simultaneously maximizing the amount of incident light absorbed is required

2.4 Conclusions

This chapter has outlined the background information on the principles and operation of photovoltaics. In addition, the principles of operation of solar cells are discussed in detail. The characterisation of semiconductor devices (including solar cells) was presented in this chapter. I-V characterisation is seen to reveal the behaviour of the electrical current through the diode (device) under external bias. In addition, the result of the IV measurement can help to obtain the total current deliverable from the solar cell as well as help to understand the possible loss mechanisms that come into play in the solar cell.

2.5 References

[1] P. A. Lynn, *Electricity from Sunlight :An Introduction to Photovoltaics*. United Kingdom: John Wiley & Sons, Ltd, 2010.

[2] H. K. Miles RW, Forbes I., "Photovoltaic solar cells: An overview of state-of-the-art cell development and environmental issues," *Progress in Crystal Growth and Characterization of Materials,* vol. 51, 2005.

[3] S. Adachi, *Earth-Abundant Materials for Solar Cells:* Cu_2*-II-IV-VI4 Semiconductors* 12/06 ed.: Wiley, 2015.

[4] J. Tauc, "Optical properties and electronic structure of amorphous Ge and Si," *Materials Research Bulletin,* vol. 3, pp. 37-46, 1968.

[5] F. J. B. a. L. H. H. J. Bardeen, in *Proceedings of the Conference on Photoconductivity*, Atlantic City, 1954.

[6] A. L. a. S. Hegedus, "The Physics of the Solar Cell," in *Handbook of Photovoltaic Science and Engineering*, ed United states: John Wiley and Sons Ltd, 2011.

[1] P. A. Lynn, *Electricity from Sunlight :An Introduction to Photovoltaics*. United Kingdom: John Wiley & Sons, Ltd, 2010.

[2] H. K. Miles RW, Forbes I., "Photovoltaic solar cells: An overview of state-of-the-art cell development and environmental issues," *Progress in Crystal Growth and Characterization of Materials,* vol. 51, 2005.

[3] S. Adachi, *Earth-Abundant Materials for Solar Cells:* Cu_2*-II-IV-VI4 Semiconductors* 12/06 ed.: Wiley, 2015.

[4] J. Tauc, "Optical properties and electronic structure of amorphous Ge and Si," *Materials Research Bulletin,* vol. 3, pp. 37-46, 1968.

[5] F. J. B. a. L. H. H. J. Bardeen, in *Proceedings of the Conference on Photoconductivity*, Atlantic City, 1954.

[6] A. L. a. S. Hegedus, "The Physics of the Solar Cell," in *Handbook of Photovoltaic Science and Engineering*, ed United states: John Wiley and Sons Ltd, 2011.

[1] P. A. Lynn, *Electricity from Sunlight :An Introduction to Photovoltaics*. United Kingdom: John Wiley & Sons, Ltd, 2010.

[2] H. K. Miles RW, Forbes I., "Photovoltaic solar cells: An overview of state-of-the-art cell development and environmental issues," *Progress in Crystal Growth and Characterization of Materials,* vol. 51, 2005.

[3] S. Adachi, *Earth-Abundant Materials for Solar Cells: Cu_2-II-IV-VI4 Semiconductors* 12/06 ed.: Wiley, 2015.

[4] J. Tauc, "Optical properties and electronic structure of amorphous Ge and Si," *Materials Research Bulletin,* vol. 3, pp. 37-46, 1968.

[5] F. J. B. a. L. H. H. J. Bardeen, in *Proceedings of the Conference on Photoconductivity*, Atlantic City, 1954.

[6] A. L. a. S. Hegedus, "The Physics of the Solar Cell," in *Handbook of Photovoltaic Science and Engineering*, ed United states: John Wiley and Sons Ltd, 2011.

[1] P. A. Lynn, *Electricity from Sunlight :An Introduction to Photovoltaics*. United Kingdom: John Wiley & Sons, Ltd, 2010.

[2] H. K. Miles RW, Forbes I., "Photovoltaic solar cells: An overview of state-of-the-art cell development and environmental issues," *Progress in Crystal Growth and Characterization of Materials,* vol. 51, 2005.

[3] S. Adachi, *Earth-Abundant Materials for Solar Cells: Cu_2-II-IV-VI4 Semiconductors* 12/06 ed.: Wiley, 2015.

[4] J. Tauc, "Optical properties and electronic structure of amorphous Ge and Si," *Materials Research Bulletin,* vol. 3, pp. 37-46, 1968.

[5] F. J. B. a. L. H. H. J. Bardeen, in *Proceedings of the Conference on Photoconductivity*, Atlantic City, 1954.

[6] A. L. a. S. Hegedus, "The Physics of the Solar Cell," in *Handbook of Photovoltaic Science and Engineering*, ed United states: John Wiley and Sons Ltd, 2011.

[1] P. A. Lynn, *Electricity from Sunlight :An Introduction to Photovoltaics*. United Kingdom: John Wiley & Sons, Ltd, 2010.

[2] H. K. Miles RW, Forbes I., "Photovoltaic solar cells: An overview of state-of-the-art cell development and environmental issues," *Progress in Crystal Growth and Characterization of Materials,* vol. 51, 2005.

[3] S. Adachi, Earth-Abundant Materials for Solar Cells: Cu_2-II-IV-VI4 Semiconductors 12/06 ed.: Wiley, 2015.

[4] J. Tauc, "Optical properties and electronic structure of amorphous Ge and Si," *Materials Research Bulletin,* vol. 3, pp. 37-46, 1968.

[5] F. J. B. a. L. H. H. J. Bardeen, in *Proceedings of the Conference on Photoconductivity*, Atlantic City, 1954.

[6] A. L. a. S. Hegedus, "The Physics of the Solar Cell," in *Handbook of Photovoltaic Science and Engineering*, ed United states: John Wiley and Sons Ltd, 2011.

Chapter 3 Thin film Synthesis & Characterisation Methods

3.1 Introduction

As mentioned in section 1.2.4, various methods have been employed to deposit SnS thin films. Among these methods, sputtering and CVD are favourable techniques. In the following section, a brief discription of the basic principles of CVD and RF sputtering is discussed. In addition, a brief descriptions of the equipment used to characterize the thin films in this work is given.

3.2 Thin film Synthesis

3.2.1 Chemical Vapour Deposition (CVD)

Fundamental CVD Processes

Chemical Vapour Deposition (CVD) is a widely used materials fabrication process that deposits a thin film on substrates from a vapour phase by chemical reaction of vapour precursors. The theory of CVD is based on chemical kinetics, fluid mechanics, chemical engineering principles, and an understanding of growth mechanisms. The main applications of CVD include thin film coating, production of high purity bulk materials and powders. The advantage of CVD over PVD is its conformal deposition profile, the capability of creating films of widely varied stoichiometry. Other advantages include relatively low cost of the equipment and operating expenses. The trade-off is that CVD is generally a much more complex process that requires knowledge about the reaction chemistry, and its interaction with the reactor hydrodynamics is necessary. Hence, many variants of CVD processing have been researched and developed in recent years, including low-pressure (LPCVD), plasma-enhanced (PECVD), metal-organic (MOCVD) and laser-enhanced (LECVD) chemical vapour deposition.

In a general overview of the CVD process, one or more of the volatile precursors are transported in the gas phase into the reaction chamber. This is achieved either by sublimation or evaporation of the precursors and introduction to a vacuum or bubbling an inert carrier gas through the precursor.

It is thought that within the reaction chamber gas phase reactions may occur between the precursor, and in some cases intermediate species can be formed. These gas phase species, chemically changed or otherwise, may be transported to the substrate and adsorbed onto the substrate. It is during this step that volatile by products of the precursors are also formed, which desorb, along with any unrequired ligands, from the substrate and are transported out of the chamber via the inert carrier gas, or vacuum, depending on the type of CVD being used. Initially, at this stage, the atoms of the film are only weakly bound to the substrate and so are free to diffuse across the surface of the film. Eventually, these weak van der Waals type interactions between the deposited material and substrate are replaced as the nucleation of the film occurs with several atoms bonding together. In addition, substrate defects act as nucleation points to which further atoms migrate, resulting in the growth of clusters of the desired material. The resulting island of material continues to grow, forming the film over time. An overview of the process is shown below in Figure 3.1.

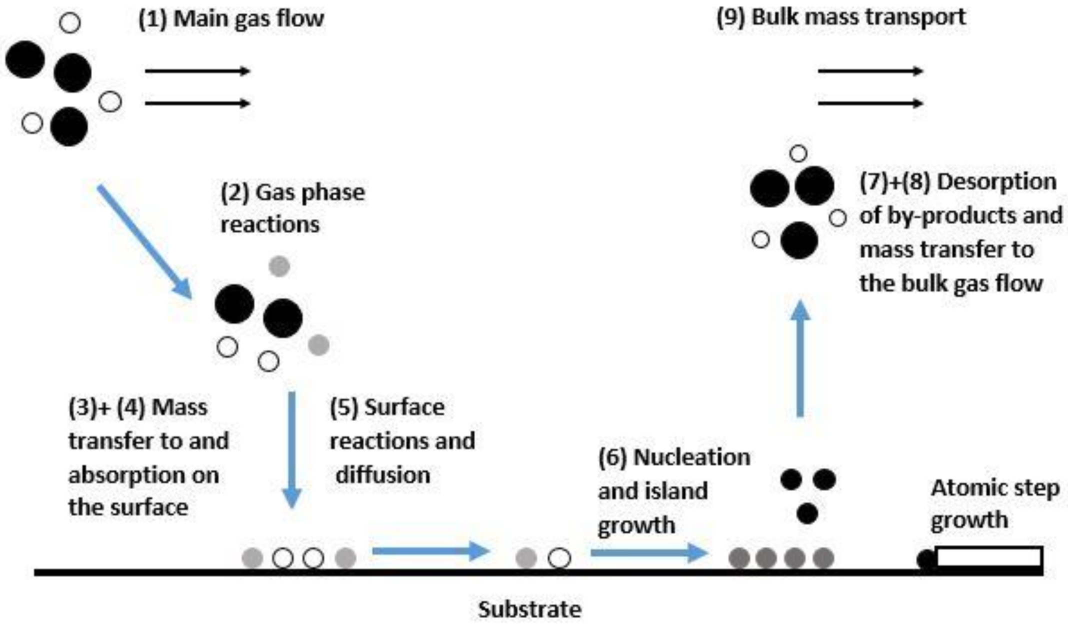

Figure 3.1 Schematic summary of the most important reactions involved in film synthesis by CVD.

Desirable Precursors of a CVD Process

In order to deposit thin films of high quality, there are certain requirements which need to be met by the precursor. Generally whatever the form of CVD is used the same precursor requirements apply. Typically for CVD, metals, metal hydrides and halides, and metalorganic compounds are employed as precursors. Metal halides, especially chlorides, are commonly used as metal precursors in CVD are relatively inexpensive and readily available. In addition, many of them are highly volatile. Precursors can be designed for optimal performance, dependant on the desired outcome, however, in general the characteristics of an ideal CVD precursor are listed below:

- Precursors should have sufficient volatility to generate active gaseous reactant species for achieving suitable growth rates within reasonable temperatures.
- The chemical reactions of the precursors need to be thermodynamically predicted to result in a solid film.
- Precursors should aim to exhibit low toxicity and low risk for safe handling.
- Decomposition should occur below the temperature that the substrate would melt or undergo phase transformation.
- It is essential that precursors are remain stable at room temperature, and do not decompose and react with air.
- Following this, the temperature difference between stable gas phase and decomposition for film growth should be considerable to prevent early decomposition.
- Be cost effective and readily available at a high purity.
- It is vital that precursors decompose cleanly with all by products being removed via exhaust.
- When synthesising precursors for CVD it is important to tailor the design of the precursor towards the above optimum requirements.

Chemical Reaction Feasibility of CVD

When a CVD system is proposed for consideration, the first task is to evaluate the feasibility of its underlying chemical reaction. If this reaction is infeasible, an alternative system should be selected and considered. Thermodynamic equilibrium compositions give the most stable chemistry of an elemental mixture at a fixed temperature and pressure. The most stable state is that with the least energy available to drive chemical processes and so is reached when the Gibbs free energy (ΔG) has its minimum value [1]. In order to calculate the Gibbs free energy of a chemical reaction, it is necessary to work out the Gibbs free energy of each reactant and product. The Gibbs free energy ΔG_r for a given species can be calculated using eq. 3.1 [2].

$$\Delta G_r = \sum \Delta G_f(products) - \sum \Delta G_f(reactants) \qquad \text{eq. 3.1}$$

The free energy of formation is not a fixed value but varies as a function of several parameters which include the type of reactants, the molar ratio of these reactants, the process temperature, and the process pressure. This relationship is represented by the following equation [3]:

$$\Delta G_r = \Delta G_f^{\circ} + RTlnQ \qquad \text{eq. 3.2}$$

Where

$$\Delta G_f^{\circ} = \sum z_i^i \Delta G_{fi}^{\circ}$$ eq. 3.3

z_i = the stoichiometric coefficient of species "i" in the CVD reaction (negative for reactants, positive for products)

ΔG_{fi}°=standard free energy of formation of species "i" at temperature T and 1 atm.

R=gas constant

T=absolute temperature

Q=$\prod_i a_i^{zi}$

a_i = activity of species "i" which is =1 for pure solids and $= p_i = x_i P_T$ for gases

p_i = partial pressure of species "i"

x_i = mole fraction of species "i"

P_T=total pressure

For a given chemical reaction, the equilibrium constant K_T is related to the Gibbs free energy ΔG_r by the following expression

$$K_T = exp\left(-\frac{\Delta G_r}{RT}\right)$$ eq. 3.4

By definition, the free energy change for a reaction at equilibrium is zero, hence:

$$\Delta G = -RT\ ln(K_T)$$ eq. 3.5

The likely direction of reversible reactions between species in the equilibrium compositions can be assessed using a simplified model. For a reaction in chemical equilibrium, the reduction in Gibbs free energy when the reactants are converted to the products,ΔG, is a function of the equilibrium constant K_{ieq} at room temperature T [4],

$$\Delta G = k_B T\ ln(K_{ieq})$$ eq. 3.6

A negative ΔG implies that the reaction may occur, whereas a positive ΔG indicates that the reaction would not take place. If several possible reactions are proposed and all are thermodynamically feasible, the reaction with the most negative ΔG should be ideally selected.

Kinetics and Mass-Transport Mechanisms

As shown above, a thermodynamic analysis indicates what to expect from the reactants as they reach the deposition surface at a given temperature. The phenomena of mass transport mechanism to reach the deposition surface involved determines the reaction rate and the design and optimization of the CVD reactor. The vaporised precursor materials are transported to the reaction chamber by an inert carrier gas. In CVD processes the rate of film growth is governed by two factors, the mass transport of precursors into the reactor and the surface kinetics of the reaction. The mass transport can be controlled by the rate precursors arrive at the substrate surface, it also has a maximum theoretical rate. The surface kinetics are controlled by the temperature of the substrate, initially a higher substrate temperature will increase the reaction rate due to increased decomposition of precursors. The rate can slow, however, due to increased desorption of precursors or exhaustion of precursors at very high deposition temperatures [3].

The CVD System Setup

In this PhD project, a custom-built CVD system was designed and set up for chalcogenide thin film depositions by my co-supervisor Kevin Haung within the Novel Glass Group at the ORC. The setup design is shown schematically in Figure 3.2. The main components include a vacuum system, substrate loading mechanism, and cylindrical quartz tube and gas delivery system. For a vapour delivery system, the precursor was loaded into a bubbler. The bubbler has one inlet where the carrier gas (Ar) is introduced and carries the precursor vapour by passing through the liquid, and one outlet where the carrier gas and the precursor vapour is transported to the reactor. The temperature of the bubbler was set by vapour pressure of the precursor and the desired flow rate of the carrier gas. A gas mass flow controller is used to control the flow rate of the input gases, Ar and H_2S. An electrical pressure controller (EPC) is used to adjust the downstream pressure of the precursor, which is associated to the precursor flow rate.

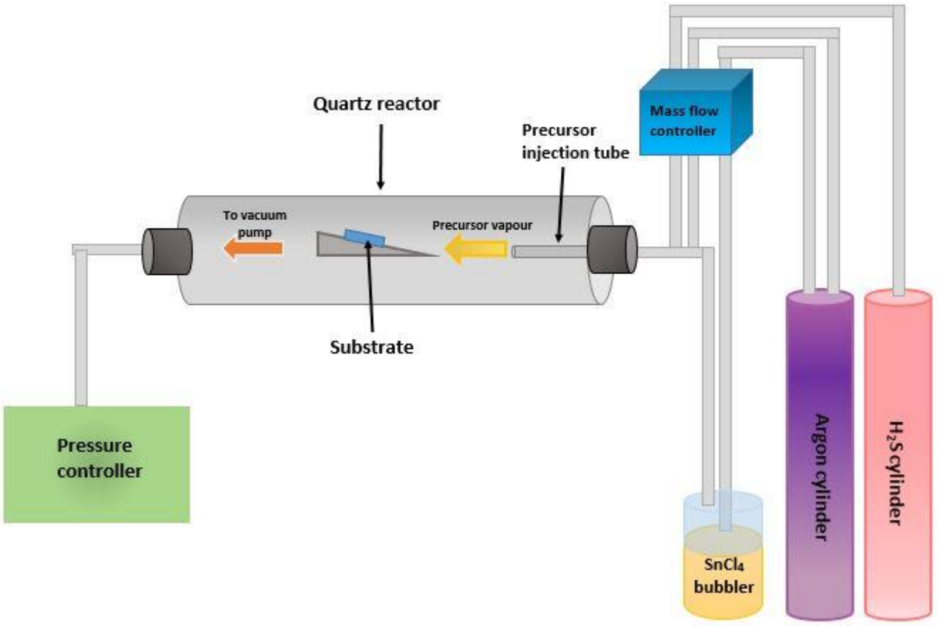

Figure 3.2 Schematic of the CVD reactor system.

For SnS thin film deposition H_2S is the reactant gas. The gas delivery system comprised two separate gas cylinders (argon 99.995% pure) and hydrogen sulphide (99.95% pure) (H_2S) cylinders. Mass flow controllers were used to regulate the flow of gases, as shown in Figure 3.3. Point of use purifications have been used to remove moisture and impurities in the gas lines before entering the CVD reaction chamber. In addition, a dew-point sensor was used to monitor the moisture level of H_2S gas line and the typical moisture level in H_2S gas line was less than 1 ppm.

Often the precursor chemicals used in CVD processes are liquids or solids, whose vapours are transported into the deposition chamber by a carrier gas. In the case of this study the metal halide precursor ($SnCl_4$) was liquid in a glass bubbler and the reactive precursor (H_2S) was gas. The glass bubbler has manual valves at its inlet and outlet for isolation during connection and removal. The bubbler is kept in a glove box in a constant-temperature bath in order to control the precursor's vapour pressure.

Figure 3.3 Gas flow control panel with all MFC's.

The carrier-gas flow through the bubbler, Ar, is measured with an electronic mass-flow controller (MFC). The vapours from the $SnCl_4$ precursors is transported into the reactor chamber by flowing a carrier gas through the bubbler, Figure 3.4. The tin precursor vapour is thus entrained in the carrier gas flow, such that the gas exiting the bubbler is a saturated mixture of the tin precursor vapour dissolved in the carrier gas. The absolute flow of tin precursor ($F_{v,out}$) is governed by Dalton's Law of partial pressures, and can be metered by controlling three parameters: (1) the flow of carrier gas ($F_{c,in}$) (2), the total pressure in the bubbler and (3) the temperature [5]:

$$F_{v,out} = F_{c,in} \frac{P_v}{P_{head} - P_v} \qquad \text{eq. 3.7}$$

where $F_{v,out}$ is the molar fraction of vapour, $F_{c,in}$ is the molar fraction of carrier gas, P_v is the equilibrium vapour pressure of precursor and P_{head} is the pressure inside the bubbler as shown in Figure 3.4.

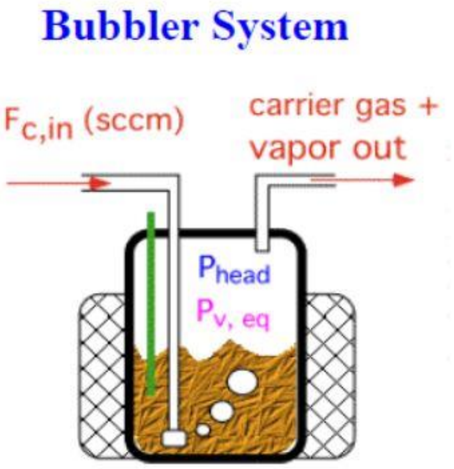

Figure 3.4 Schematic of the bubbler system for liquid precursor [3].

3.2.2 Radio Frequency (RF) Sputtering

Sputtering belongs to the physical vapour deposition (PVD) processes. It is successfully used in many application areas, particularly in microelectronics and surface engineering, for the production of films and coatings. Some of the advantages of the technique are that it is a fast, scalable process, simple and reliable, and capable of meeting the economic and functional requirements in industrial productions. More ever, the sputtering deposition process operates under physical conditions which makes it possible to synthesize films with new physical and functional properties [6, 7].This method also offers a more reproducible deposition control compared with other methods.

Figure 3.5 shows the schematic of the sputtering system. A target of the material deposited is located inside a vacuum chamber where it is connected to the negative terminal of the power supply. Facing the target is the substrate which may be electrically grounded or biased.

This process depends on the kinetic ejection of vapour species from the surface of a material known as the target or cathode by bombardment with energetic and non-reactive ions, resulting in the removal of fractions of a material from the sputtering target and depositing them on a substrate [8, 9].

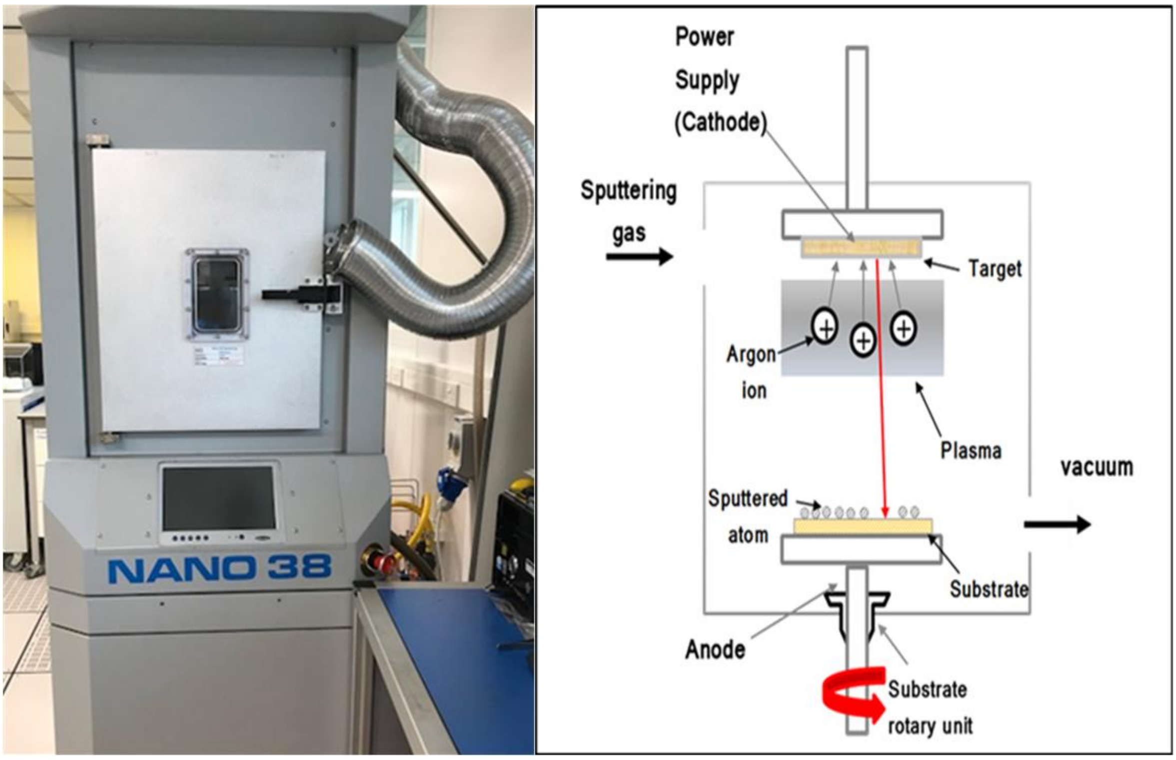

Figure 3.5 image of a NANO sputter facility in ORC clean room (left) and Schematic of a sputtering system (right).

A film is formed when the ejected atoms condenses on the surface of the substrate. During the deposition, a high voltage is applied (by DC or RF power supply between the target (cathode) and the ground. The ions are formed by what is known as a glow discharge process, this is the ionisation of inert gas atoms through electric discharge, resulting in the creation of plasma. A heavy, chemically inert gas, such as argon, is frequently used as a major constituent of a sputtering gas and is fed into the chamber. The gas pressure is relatively high (10^{-4} to 10^{-6} mbar). Plasma can be defined as a gas with charged and neutral particles, for example, electrons, positive ions, atoms and molecules. Overall the plasma is charge neutral. Due to the natural cosmic radiation, there are always some ionized Ar+ ions present in the chamber to ignite the plasma.

There are several variations of the sputtering process. If a conducting target, such as a metal, is used, then a DC voltage can be applied to it to maintain the plasma discharge that accelerates the argon ions. This is referred to as a diode arrangement. Sometimes, a grid is included in the system to help stabilize the discharge, and these are called DC triode systems. If the target is not conductive, then it is not possible to use it to carry the direct current. One then uses an alternating current and couples it capacitively to the plasma. A frequency of 13.56 MHz is used for this purpose. Power levels may range from a few hundred watts to a few kilowatts.

Sputtering from binary or even ternary targets is commonly used in industrial and research-related processes it is a fast, relatively easy to implement and scalable process [10]. One of the great advantages of sputtering is that it allows the deposition of alloy thin films that maintain the composition of the target due to the fact that the material is ejected layer by layer. The relationship between sputtering parameters, target composition and film composition was investigated for binary targets. Compound sputtering can be explained as follows. Elements composing the target material typically have different sputtering yields called partial sputtering yields. The surface composition then differs from the bulk as atoms with higher yield are ejected at an increased rate. This is called preferential sputtering. When steady state sputtering conditions are reached and if diffusion within the target is neglected, the partial sputtering yields evolve towards an equilibrium where constituents are ejected with proportions corresponding to the target bulk composition[11]. When it comes to complex compounds, co-sputtering of elemental and/or binary targets is usually preferred because it allows to control the composition of the sputtered film by varying the power supplied to the different targets.

The depositions were completed using a Kurt J Lesker NANO38-SPUTTER radio frequency RF 13.56 MHz) magnetron sputtering. With the help of a roughing pump connected to the chamber, low vacuum (10-1 Torr) can be achieved. After roughing the chamber to low vacuum, the chamber is pumped down with a turbo molecular pump.

3.3 Thin-Film Material Characetrsiation Methods

The characterisation done will be discussed under four major headings: structural, optical and electrical and device characterisation. The main material characterisation this chapter concentrates using Raman Spectroscopy, X-ray Diffractometer (XRD), Energy Dispersive X-ray Spectroscopy (EDX). Scanning Electron Microscopy SEM. Electrical and device characterisation will be discussed in chapter

3.3.1 Raman Spectroscopy

Raman spectroscopy is a structural characterisation tool used in characterising thin films from their characteristic spectral pattern (finger prints) of the material. This method proved to be successful in the identification of structural information for both qualitative and quantitative analysis. Moreover, Raman technique is highly sensitive, meanings it is able to differentiate molecules in chemical species that are very similar.

Raman measurement is a vibrational spectroscopy whose principle is based on the inelastic scattering of a monochromatic excitation source (usually a laser). This is because phonons in crystals or molecular vibrational modes have frequencies which are characteristic of the particular crystal or molecular structure. When we illuminate a material by monochromatic light beam, this exciting radiation is transmitted, reflected, absorbed or scattered by the material.

The mechanism for the Raman effect lies in the irradiation of the sample with monochromatic light, causing a change in the vibrational quantum states of the molecules being illuminated. As a result, a small fraction of the scattered radiation is shifted to frequencies which correspond to the sample's vibrational transitions. With sample illumination being monochromatic, most scattering taking place is elastic with no loss of energy and, therefore, no frequency change. This type of elastic scattering, which appears as an intense, unshifted component of the scattered light is called Rayleigh scattering. Raman scattering, however, is due to the inelastic scattering of incident photons, wherein the energy is transferred to or received from the sample due to changes in the vibrational or rotational modes of the sample molecules, causing a change in the energy, and therefore the frequency of the scattered light. Lines shifted to energies lower than the source are generated by molecules in the ground-state, while the slightly weaker lines at higher frequency are due to molecules in excited vibrational states [11]. These lines, the result of inelastic scattering of light are referred to as Stokes and anti-Stokes lines, respectively, Figure 3.6.

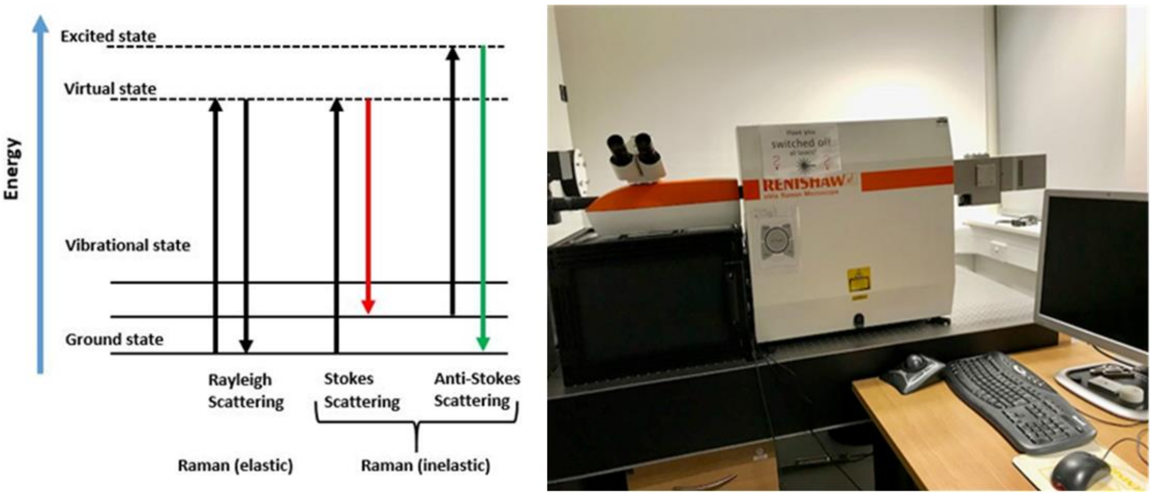

Figure 3.6 Schematic of energy level showing the states involved in Raman spectra (left), Renishaw inVia Raman microscope used to characterise the thin films in this thesis (right).

Raman microscopy in this thesis was carried out with a Raman spectrometer (Renishaw inVia system) which consisted of a light microscope coupled to a Raman spectrometer with diode-pumped solid state laser at λ=633 nm with an excitation power of with an excitation power of 10 mW. The microscope was equipped with a 50 x objective (N-plan). The microscope optics were used to focus the laser beam onto the sample and to collect the scattered light to a focus of approximately 1.2 µm.

3.3.2 X-ray diffraction (XRD)

X-ray diffraction (XRD) technique is a non-contact and non-destructive method generally used in the analysis of thin films. XRD is an extremely important technique in the field of material characterization and provides information of phase of the material, lattice parameters of the unit cell and atomic positions as well as crystallite size and crystallite strain.

The crystal atoms act as diffraction centres; constructive and destructive interference of the diffracted beam constrain this beam to certain angles in relation to the incident beam [12]. The angular relationship between incident beam and diffracted beam leading to constructive interference is given using Bragg's law of diffraction [13].

$$2dsin\theta = n\lambda$$ eq. 3.8

where d is the lattice plane spacing, θ is the is the angle between the incident (or diffracted) ray and the corresponding crystal plane (Bragg angle), n is an integer and is referred to as the order of diffraction and is often unit, and λ is the wavelength of the radiation.

A typical schematic of the XRD is shown in Figure 3.7. X-rays radiation has property to pass through a material and be diffracted by the atoms. The technique allowed to determine the inter-spacing and ordering of atoms in the crystal lattice. The geometrical alignment of source, sample and detector needs to allow the detection of diffraction maxima. During a scan, either sample and detector or source and detector are moved to keep the correct angular relationship. The diffracted intensity measured is plotted versus 2θ degree depends on the energy of the incident radiation and spatial distribution of atoms (crystal structure). The diffraction angles, at which a signal is detected, correspond to a lattice spacing d. Together with intensity ranking of peaks this allows to identify present phases and orientations from known standards. Further quantities commonly sought from thin-film diffraction are lattice parameter, coherency length (related to peak width in the measured spectra) and volume fraction.

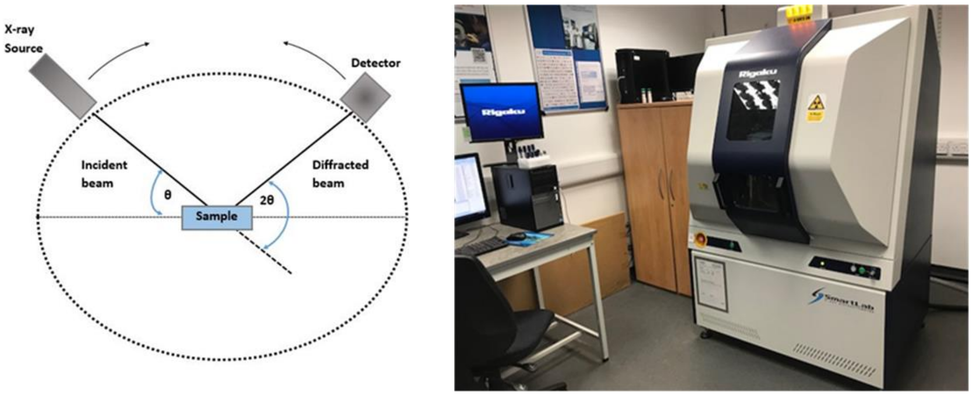

Figure 3.7 Schematic diagram of XRD experiment (left), image XRD system used in this thesis.

The phases and crystal structure of thin films in this chapters 4 and 6 were examined by X-ray diffraction (XRD) (Rigaku-2000 X-ray diffractometer), using Cu-Kα radiation and an angle of incidence of 1.5418^o. The 2θ-range for the diffractometer was set from 10^o to 80^o with a step size of 0.04. The observed phases were determined by comparing the d-spacing with the Inorganic Crystal Structure Database (ICSD) files.

3.3.3 Scanning Electron Microscopy (SEM) and Energy Dispersive X-ray Spectroscopy (EDX)

SEM uses a high energy electron beam focussed on a sample to produce high resolution images of the sample surface. A primary electron beam generated by an electron source. The electron beam is usually generated using a thermionic or field emission electron source. Bombardment of the sample surface with high energy electrons results in the formation of secondary electrons and backscattered electrons. A schematic diagram of a typical SEM setup is given in Figure 3.8.

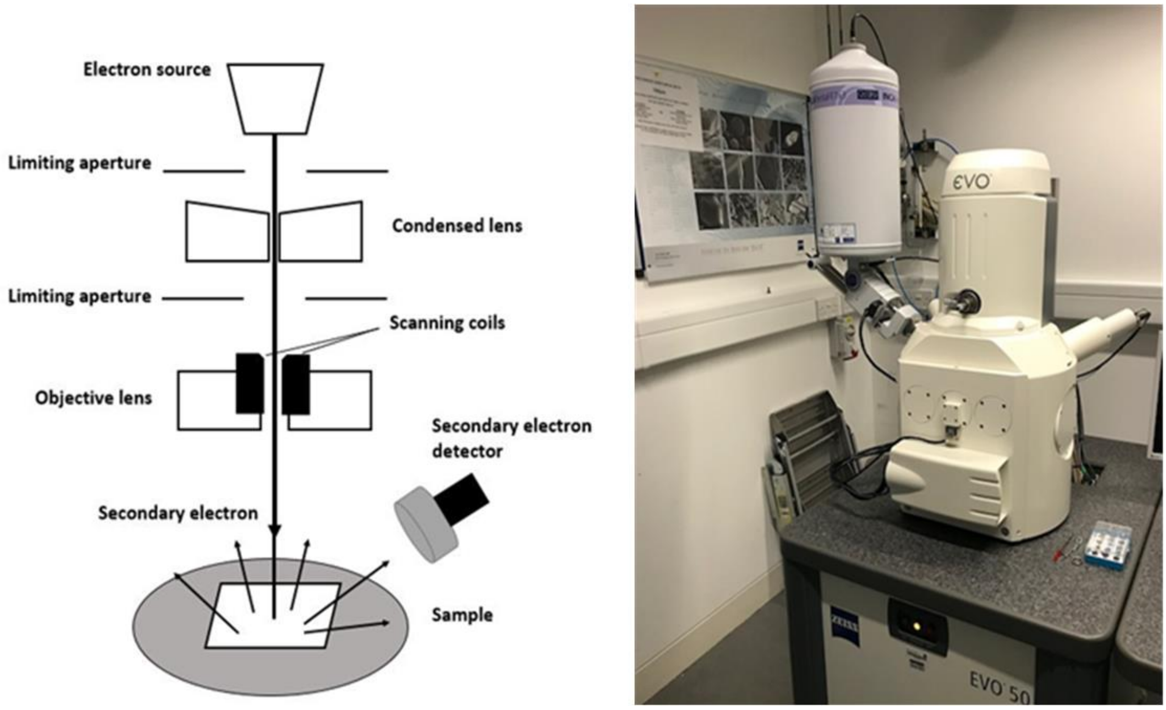

Figure 3.8 Schematic diagram of scanning electron microscope (SEM) (left), image of the ZEISS SEM facility in ORC (right).

Electron microscopes usually operate in high vacuum, to avoid electron interaction with gas molecules. The sample is grounded to prevent it from charging up. The electromagnetic lens system (condenser and objective) focuses the beam into a very fine spot with sizes of 1 to 10 nm. A set of scan coils placed closer to the objective lens is used to detect the beam in two orthogonal lateral directions so that it scans a rectangular area of the sample surface [14].

Secondary electrons are electrons ejected from the sample as a result of high energy electrons incident bombarding the sample. As the kinetic energy of secondary electrons is generally low compared to that of backscattered electrons, they are normally recaptured by ionized atoms within the sample and thus can only escape from the surface of the sample. Backscattered electrons are electrons that have undergone elastic or inelastic scattering with the sample surface. The kinetic energy of backscattered electrons is higher than that of secondary electrons. The intensity of backscattered electrons depends greatly on the atomic number. The scattering intensity is increased with atomic number due to regions of higher electron density. Regions with higher electron density across a sample appear brighter in backscattered electron images. SEM was performed to determine surface morphology using a ZEISS EVO 10 SEM at an accelerating voltage 5 keV and aperture of 20µ.

Usually installed as part of an SEM system, Energy Dispersive X-ray Spectroscopy (EDX) analyses the x-rays emitted from a sample that have been generated by the electron beam. This quick and convenient technique allows the quantitative measurement of relative amounts of individual elements in a sample based on the detection of electrons escaping from a material as a result of an incident electron beam excitation.

The observations of Scanning Electron Microscopy can be local, qualitative and quantitative by measuring the energy of X-rays produced by the sample. Indeed, the arrival of an incident electron into contact with an electron of heart from an atom of the sample may cause the expulsion of the latter. Penetration of high energy electrons in a material also induces excitation of some core electrons without enough energy to eject them. When those electrons relax to lower energy states, x-ray radiation is emitted again the emitted characteristic X-rays are used to generate an energy dispersion spectrum of atoms of the elements in the sample by means of the software programs incorporated into the equipment. From this spectrum the approximate atomic composition of the sample can be obtained. The analysis of these rays permits sample identification. All EDX measurements reported in this thesis were carried out using EDX detector (Oxford Instruments, UK) attached to an SEM

3.4 Electrical Characerisation

3.4.1 Hall Effect

When a current goes through a conductor subjected to a perpendicular external magnetic field, a voltage difference will appear, transverse to the electric current and to the magnetic field. This phenomenon is called Hall effect, which was discovered in 1879 by Edwin Herbert Hall while he was working on his doctoral degree at Johns Hopkins University in Baltimore, Maryland [43]. Hall effect can provide some essential parameters of a semiconductor such as conductivity type, carrier concentration, carrier mobility etc. It is now one of the most important methods for characterizing semiconductor materials.

3.4.2 Current-Voltage (IV) curves

Current-voltage characterisation is the main electrical measurement for solar cells. The parameters used to define a cell performance are short circuit current (Isc) or current density (Jsc), open circuit voltage (Voc), Fill Factor (FF) and combining these parameters, cell efficiency (η). The current-voltage curve is

generated by measuring the current as a function of the input Voltage. The intercepts with the y- and x- axis are then obtained and, correspond to the Isc and Voc respectively. The shape of the curve gives information on the FF, shunt and series resistances and roll-over effect. The electrical measurements are generally carried out using a Keithley electrometer

3.5 References

[1] B. Smith, *Basic Chemical Thermodynamics; 4th ed.;*. NewYork: Oxford University Press, 1990.

[2] P. J. d. Atkins P, *Atkins' physical chemistry, 8th edn*. Oxford: Oxford University Press, 2006.

[3] H. O. Pierson, Handbook of Chemical Vapor Deposition: Principles, Technology and Applications. New York, USA: William Andrew Publishing I.I.C., 1999.

[4] M. Ohring, Materials Science of Thin Films Deposition and Structure. 2nd Edition. San Diego: Academic Press, 2002.

[5] Z. Y. a. C. C. David Bour, "Simple technique for measuring the filled volume of liquid or solid CVD precursor chemicals in bubblers," *Journal of Crystal Growth,* vol. 310, pp. 2673-2677, 2008/05/01/ 2008.

[6] L. W. Boydens F, Persoons R and Depla D, "The influence of target surface morphology on the sputter deposition flux," *Thin Solid Films,* vol. 531, pp. 32-41, 2013.

[7] M. K. K. Wasa, and H. Adachi, *"3 - sputtering phenomena" in Thin Film Materials Technology*. Norwich, NY: William Andrew Publishing, 2004.

[8] J. A. Thornton, "Influence of apparatus geometry and deposition conditions on the structure and topography of thick sputtered coatings," *Journal of Vacuum Science and Technology of Advanced Materials,* vol. 11, pp. 666-670, 1974.

[9] H. H. Andersen, Sputtering by Particle Bombardment I: Physical Sputtering of Single-Element Solids vol. 47: Springer Berlin Heidelberg, 2014, 1981.

[10] M. B. O. Knotek, and T. Leyendecker, "On structure and properties of sputtered Ti and Al based hard compound films," *Journal of Vacuum Science & Technology A: Vacuum, Surfaces, and Films,* vol. 4, pp. 2695–2700, 1986.

[11] J. D. M. J. A. Frantz, R. Y. Bekele, V. Q. Nguyen,.J. D. M. J. A. Frantz, R. Y. Bekele, V. Q. Nguyen, B. M. Sadowski, S. I. Maximenko, M. P. Lumb, R. J. Walters, and J. S. Sanghera, "Quaternary sputtered Cu(In,Ga)Se_2 absorbers for photovoltaics: A review

" IEEE Journal of Photovoltaics, vol. 6, pp. 1036–1050, 2016.

[12] L. C. F. T. L. Alford, and J. W. Mayer, *Fundamentals of Nanoscale Film Analysis*. New York,: Springer, 2007.

[13] B. D. Cullity, *Elements of X-Ray Diffraction, 2nd Edition*: Addison Wesley, Massachusetts, 1978.

[14] J. Goldstein, Newbury, D.E., Echlin, P., Joy, D.C., Romig Jr., A.D., Lyman, C.E., Fiori, C., Lifshin, E, *Scanning Electron Microscopy and X-ray Microanalysis. 2nd ed.*: New York, London: Plenum Press, 1992.

Chapter 4 Synthesis and Characterisation of Single Phase Tin Sulphide Thin Films by Chemical Vapour Deposition

4.1 Introduction

The industrial demand for inexpensive and scalable PV devices drives this research and here the results for a low-cost method to synthesize high quality tin sulphide thin films with electrical and optical properties are reported.

The deposition was achieved by using a metal halide precursor, which allows the deposition to take place at room temperature, despite most studied cases, where the deposited films were formed at relatively high temperatures. As SnS has a high vapour pressure, losses of material occur at high processing temperatures. In addition, SnS films grown at such high temperatures have a very high surface roughness [1]. Moreover, recrystallization requires much more energy than producing a crystalline phase from an amorphous film [2].

This chapter demonstrates a successful route and provides a detailed study to grow high quality, stoichiometric SnS from the reaction of $SnCl_4$ and H_2S by CVD. A description of the growth process and its optimization to obtain SnS samples with good quality in terms of phase stability, composition control and homogeneity is presented. The control of the different phases in the CVD process, and how this is affected by the process conditions is discussed. The dependence of the SnS phase on both the $SnCl_4$ to H_2S.concentration ratio and on the post annealing temperature is explored. By adjusting the conditions of the CVD process, the product can be tuned to p-type SnS as demonstrated by a pn junction in the Chapter 5.

4.2 Feasibility of Reaction by Thermodynamics

Before considering the use of CVD reaction, it must first be determined if the reaction is thermodynamically possible. To study the possible reactions in this CVD process, we perform thermodynamic calculations to analyse their changes in standard Gibbs free energy. The feasibility of the chemical reaction relies on the change in Gibbs free energy. When the change of Gibbs free energy of the reaction is negative, then the reaction is feasible at the given conditions [6]. When $SnCl_4$ reacts with H_2S, the reactions forms SnS or SnS_2 at a temperature of 20 ℃ according to the following reactions:

$$SnCl_4(g) + 2H_2S(g) \rightarrow SnS(s) + 4HCl(g) + \frac{1}{2}S_2(g) \qquad \text{eq. 4.1}$$

$$SnCl_4(g) + 2H_2S(g) \rightarrow SnS_2(s) + 4HCl(g) \qquad \text{eq. 4.2}$$

Thermodynamic calculations of the formation of SnS (eq. 4.1 and eq. 4.2) were used to evaluate the value of the standard Gibbs energy of gas specie using the standard enthalpy and entropy, Appendix A1. Figure 4.1 shows that Gibbs free energy of the SnS growth is positive but negative for SnS_2 growth. That shows that SnS growth from $SnCl_4$ and H_2S at temperature of 20 °C is not spontaneous.

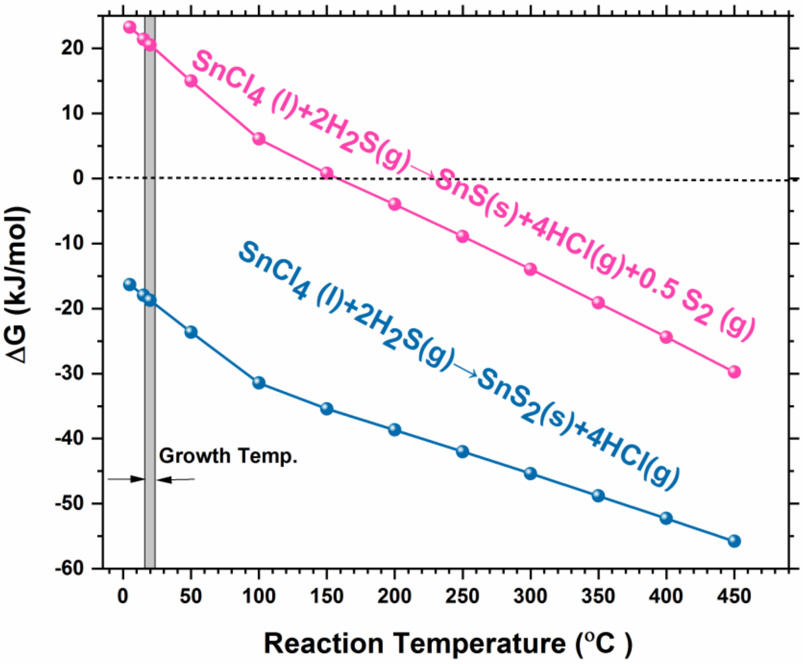

Figure 4.1 Changes in Gibbs free energy of possible reactions in the CVD process.

The Gibbs free energy for the reaction eq. 4.2 shows it is more feasible than reaction described in eq. 4.1. The high volatility of sulphur requires excess sulphur in the system to ensure the deposition of stoichiometric material. Moreover, according to the thermodynamic calculations the amount of SnS_2 material is favourable at low temperatures (20-150 °C), Figure 4.2

Inspired by the result of this thermodynamic calculation, we designed a series of reactions to grow SnS thin films which will be a two-step process. First, we preform the reaction at room temperature (20 °C). Secondly, a post annealing treatment was performed to adjust the Sn to S ratio and enhance the grain growth.

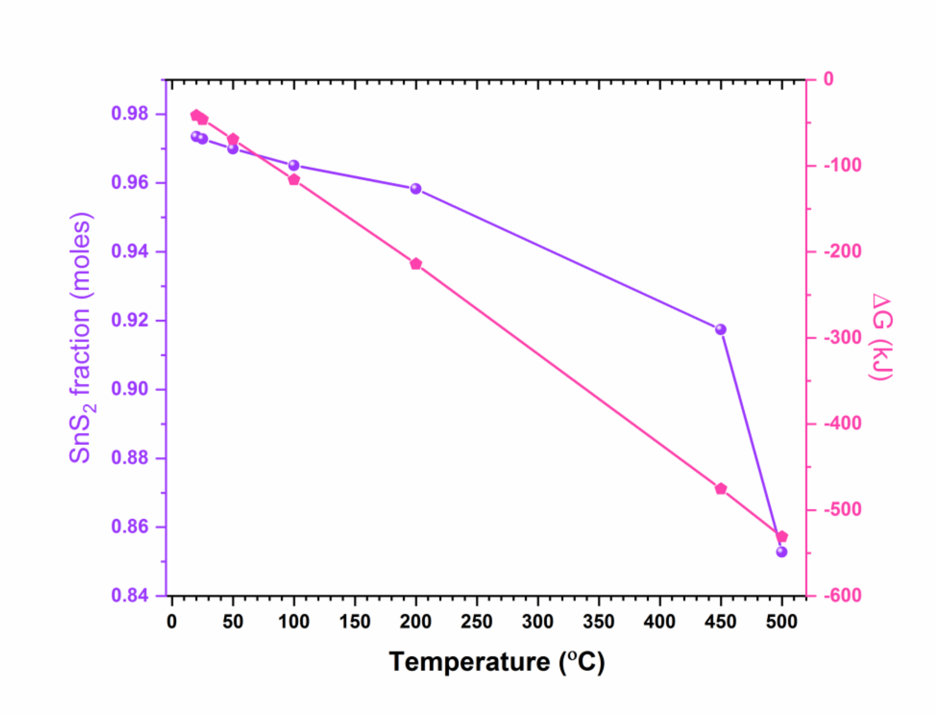

Figure 4.2 Change in reaction product concentration according to eq. 4.2 and Gibbs free energy at different deposition temperatures.

4.3 The First Step: Room Temperature Growth of the SnS Thin Films

In this PhD project, SnS thin films were grown by a two-step process. The first step is a low vacuum deposition by room temperature CVD which results in amorphous phase sulphur rich tin sulphide thin films. This step is followed by a heat treatment of the films in a sulphur atmosphere (H_2S atmosphere), necessary to tune up the phase.

A in-house made CVD system was designed and built in the ORC by Dr.Haung [7]. The experimental set-up we used for the deposition of SnS thin films in this thesis is shown schematically in Figure 4.3. The main components include a vacuum system, substrate loading mechanism, and cylindrical quartz tube, gas delivery system and a bubbler. The tin and sulphur source materials were $SnCl_4$ (99.995% from Sigma Aldrich Chemical Co.) and H_2S 99.95% pure. The vaporisation is done in a bubbler, by passing a carrier gas through the precursor. Tin tetrachloride was used as supplied and placed into a glass bubbler as in Figure 4.3. The bubbler was kept at room temperature in a nitrogen purged glove box as the whole system was as well. In these experiments three gas lines were used, two for argon and one for argon/ hydrogen sulphide. H_2S is highly toxic and corrosive. To ensure safe operation, both the H_2S lines and annealing furnace are stored within a glovebox. The glovebox is equipped with an H_2S detector with an alarm that is sensitive to detect less than 5 ppm of H_2S.

$SnCl_4$ was introduced into the gas streams by passing argon gas through the liquid using mass flow controllers for the inert argon carrier gas. The $SnCl_4$ was diluted with another argon line using a Tee connection of 0.5 inch. The diluted $SnCl_4$ stream and H_2S stream were mixed by using connection tubes before introduced to the reactor by a quartz injection tube. The injection tube was inserted directly to the quartz reactor. Soda lime glass (SLG) and thermally oxidized 298 nm SiO_2 layer on a p-type silicon (Si) substrate (2 × 2 cm^2) were used as substrates placed on an inclined substrate holder, Figure 4.4. The downstream was connected to a pressure controller which allowed deposition to go on at a pressure of 100 mbar (1 mbar = 0.75 Torr = 100 Pa).

Gas flows were adjusted using suitable regulators and mass flow controllers. The pressure controller was connected to the extraction system. The film growth rate is determined by several parameters: the temperature of the substrate (reaction zone), the operating pressure of the reactor, and the composition and chemistry of the gas-phase, etc. Deposition experiments were timed by stop watch and were 2 hours. At the end of the deposition the bubbler line was closed and only argon gas was passed over the substrate. The sample is unloaded from the quart tube and stored in a clean sample box.

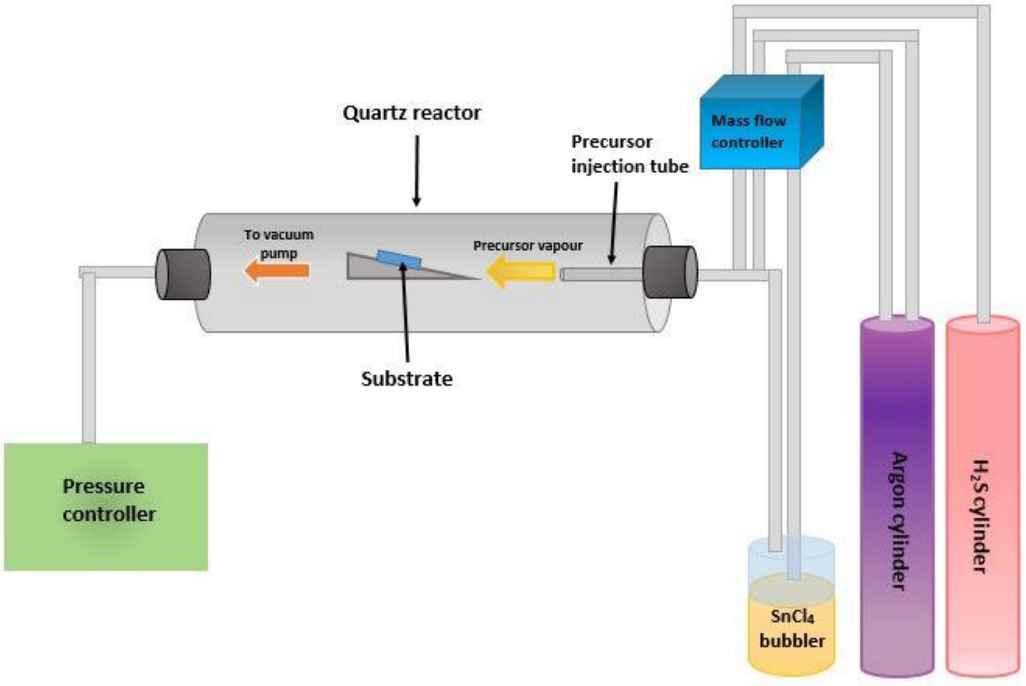

Figure 4.3 Schematics of CVD system used to grow SnS thin films in this thesis.

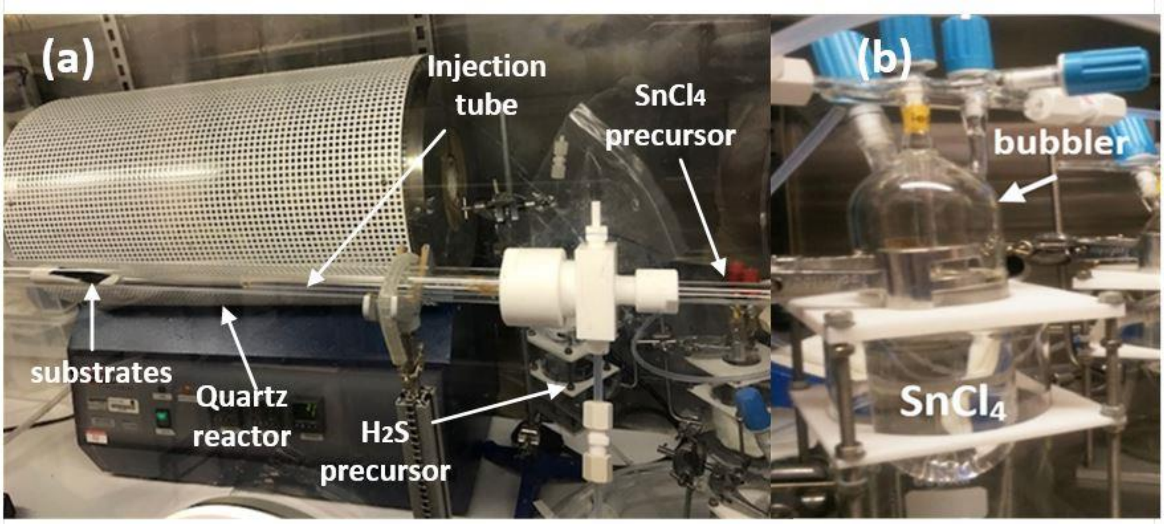

Figure 4.4 The CVD system in ORC (a) shows the reactor and injection of gases (b) shows the glass bubbler of tin precursor.

Figure 4.5 shows the SEM images of the as-deposited samples having a dense and good surface coverage. All films deposited were pinhole free and adhered strongly to the substrate.

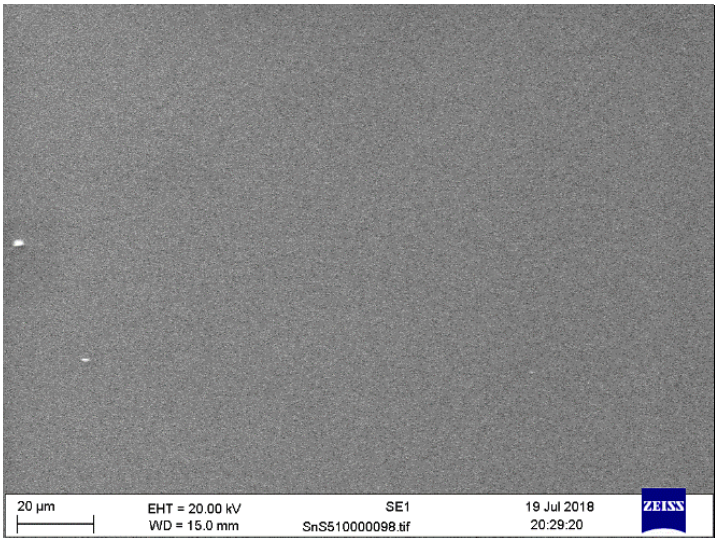

Figure 4.5 SEM image of as-deposited SnS films at optimised deposition conditions.

4.3.1 Influence of Precursor Concentration Ratio $H_2S/SnCl_4$ on the Morphology and Composition of SnS Thin Films

In this section the effect of variation of precursor concentration ratio $H_2S/SnCl_4$ on the morphology and composition of SnS thin films is studied. The deposition process in this study had three key challenges that had be overcome:

(1) The challenge of obtaining a uniform good quality film, free of cracks and with good adhesion to the substrate.
(2) The challenge of optimising the post annealing step to produce good quality single-phase SnS, without the incorporation of other sulphur-rich tin sulphides, such as SnS_2 and Sn_2S_3 as well as good crystallinity, section 4.4.
(3) The challenge of enhancing the electrical properties of thin films which will be discussed in Chapter 5.

To overcome the first challenge, the effect of precursor concentration ratio $H_2S/SnCl_4$ on the growth of SnS thin films was investigated keeping all other deposition parameters constant. According to the thermodynamic calculations solid SnS_2 is the main reaction product at the deposition conditions of this study. Nevertheless, additional reactions can occur at various precursor concentrations and are therefore also analysed by the thermodynamic calculations. Thermodynamic calculations were used to predict the amount of reaction products obtained (SnS_2 (solid) and unreacted $SnCl_4$ (liquid phase)), depending on the $H_2S/SnCl_4$ concentration ratio, Figure 4.6.

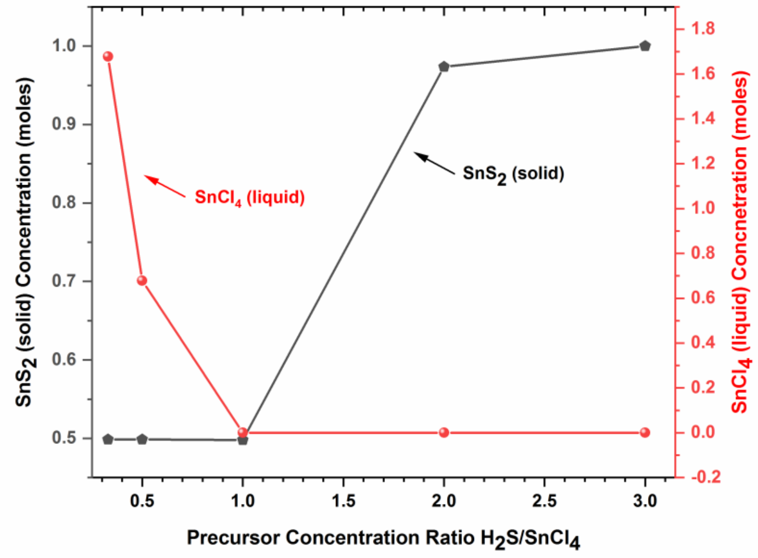

Figure 4.6 Effect of $H_2S/SnCl_4$ precursor concentration ratio on the reaction product concentration.

Figure 4.6 shows the impact of precursor concentration ratio on the reaction products according to the reaction in eq. 4.2. Interestingly, for high $SnCl_4$ concentrations unreacted liquid $SnCl_4$ is more likely to be formed with solid SnS_2 . This unreacted precursor will affect the growth of the thin film. Therefore, a low $SnCl_4$ concentration was applied in this study. A flow rate of 20 sccm was applied with varying the reactant precursor, H_2S. The mass flow rate measured in sccm is proportional to the number of molecules per minute flowing into the reaction chamber, the relationship is given by 1 sccm=2.69X10^{19} molecules per minute [8]. For the growth of $SnS_{2,}$, it is necessary to have one Sn^{4+} ion for every two S^{2-} ions to produce the products of the reaction in eq. 4.2. Table 4.1 shows the effect of precursor concentration ratio $H_2S/SnCl_4$ on the composition of the deposited films. There is no clear trend to the effect of $H_2S/SnCl_4$ on the Sn/S ratio or unreactive chlorine.

Table 4.1 The effect of the precursor $H_2S/SnCl_4$ ratio concentration on film composition.

Sample ID	Gas flow (sccm)		H_2S concentration (mole/min)	$SnCl_4$ concentration (mole/min)	Concentration ratio H_2S/ $SnCl_4$	Elemental composition (EDX)			
	H_2S	$SnCl_4$				Sn	S	Cl	Sn/S
SnS 55	10	20	0.44×10^{-03}	6.22×10^{-04}	0.71	40.61	40.68	18.72	1
SnS 57	20	20	0.88×10^{-03}	6.22×10^{-04}	1.42	43.16	30.60	26.25	1.64
SnS 51	50	20	2.21×10^{-03}	6.22×10^{-04}	3.55	31.34	37.62	31.04	0.83
SnS 37	100	20	4.42×10^{-03}	6.22×10^{-04}	7.10	41.25	30.40	28.35	1.36
SnS 53	150	20	6.62×10^{-03}	6.22×10^{-04}	10.65	41.93	34.97	23.10	1.20

To determine the effect of $H_2S/SnCl_4$ precursor on the morphology of the deposited films, SEM images were obtained Figure 4.7. Films deposited using $H_2S/SnCl_4$ ratio concentrations of 7.097 × 10^{-01} and 1.419 mole/min show poor film growth with obvious cracks, discontinuous and island distribution. This is attributed to unreacted $SnCl_4$ precursor incorporation in the film composition which causes degassing in the chamber leading to cracks and liquid precursor on the films. These results indicate that good quality SnS thin films are grown at a low $SnCl_4$ concentration.

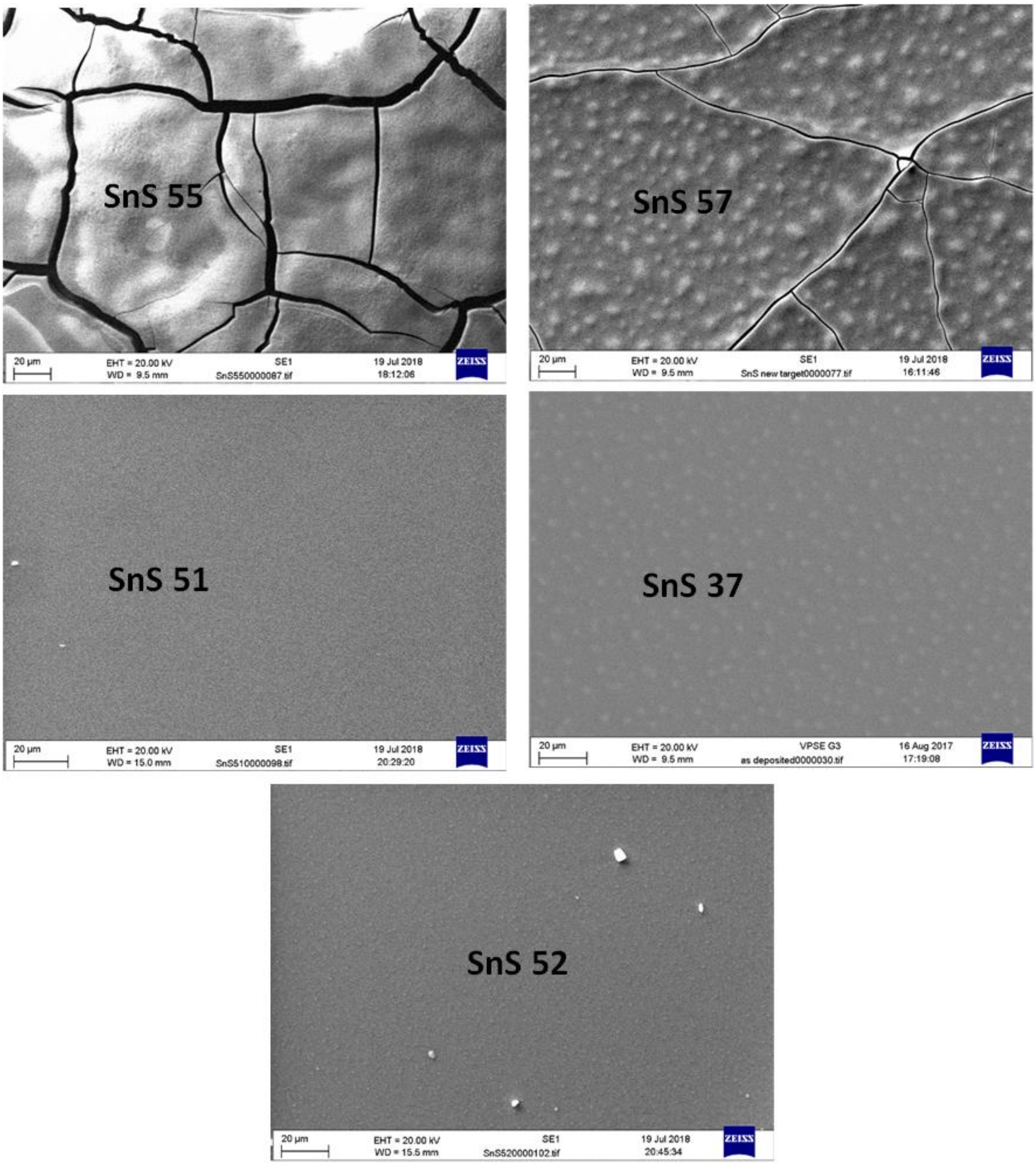

Figure 4.7 SEM images showing the effect of precursor concentration ratio on the morphology of SnS thin films.

4.4 The Second Step: Post-Depositon Annealing Procedure

The second step of the growth method in this study is post-deposition annealing. The low temperature growths generally results in amorphous films, Figure 4.9, that confirm the amorphous nature of the deposited films. Moreover, the as-deposited films in this work are containing unreacted chlorine, therefore annealing was performed. Due to the high volatility of sulphur, loss of sulphur from SnS is commonly observed after annealing in an inert atmosphere which affects the stoichiometry of the thin films. Therefore, the films here were annealed in a H_2S atmosphere. In the presence of H_2S atmosphere, SnS films also experience abnormal or secondary grain growth to form much larger grains and fewer grain boundaries.

It is evident that, during annealing, H_2S atmosphere significantly enhances the grain size of SnS compared to inert gases [9]. In the annealing process, temperature, time, pressure and type of atmosphere can strongly affect the morphology, crystallinity, and electrical properties of the thin films. Reddy et al. have reported that single phase SnS thin films can be obtained for a sulfurization temperature around 300 to 350 °C [10]. Additionally, Minemura et al. have shown that for a higher sulfurization temperature, both small and large area of SnS thin films have a single phase [11]. Despite the fact that the record efficiencies for this material are annealed in H_2S atmosphere [12].The effects of annealing temperature were studied. The impact of annealing on morphology, composition and structural properties was investigated and presented below.

The annealing treatment was performed in a tubular three-zone furnace system (Elite 3 zone horizontal tube furnace) that was enclosed in a nitrogen glove box. Figure 4.3 shows the setup of the tube furnace for annealing SnS thin films in this thesis work. A quartz tube with an inner diameter of 30 mm, and length of 900 mm was installed in the furnace. The as-deposited samples were placed on a quartz substrate holder which was fixed in a quartz tube where annealing was performed at a constant working pressure of 6 mbar. After the quartz tube was evacuated by a vacuum system, the tube was backfilled with a high-purity carrier gas of a carrier gas of Argon (Ar). Both ends of the quartz tube were connected to the gas-inlet and outlet, which allows the flowing of H_2S/argon gas with a flow rate of 50/150 standard cubic centimetres per minute (sccm) during the annealing process. The exhaust from the reactor was vented directly into the extraction system. Before starting heating, a pump was used to evacuate the quartz tube filling the tube with argon. The system was evacuated and the annealing process was performed for 2 hours at temperatures ranging from 350 C to 450 °C. The ramping heating rate was fixed at 10 °C/min in all cases. Afterwards, the furnace was left to naturally cool down to room temperature. The flowing system ensures that gaseous decomposition products from the samples are continuously removed, and therefore do not affect the controlled partial pressures in the annealing system.

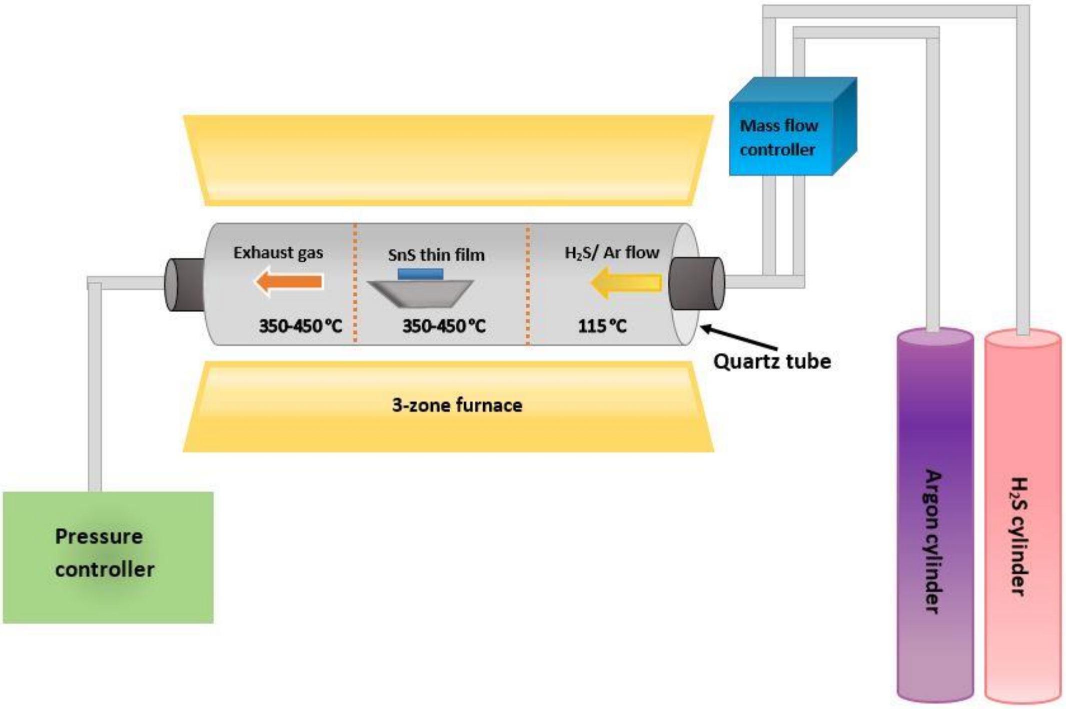

Figure 4.8 Schematic diagram of CVD annealing system.

4.4.1 Effect of Post-Deposition Annealing Temperature

To investigate the optimum annealing conditions, the effect of annealing temperature on phase and material quality was studied. The as-deposited samples were annealed at temperatures between 350 -450 °C. However, the goal with this work was to create the SnS phase with a stoichiometry of a 1:1 ratio of Sn:S. The high volatility of sulphur requires excess sulphur in the annealing system to ensure the stoichiometric material. The challenge to maintain stoichiometric SnS extends further for post deposition heat treatments. Slight tin deficiency is preferable, as tin vacancies will yield p-type material. Burton et al. found that tin vacancies form easily due to their low formation energy [12]. The high concentration of tin vacancies relative to sulphur vacancies will cause SnS to be p-type.

The phase transformation of SnS phases that occur during annealing may be interpreted as the result of different following decomposition reactions. Control of these reactions is important for guaranteeing the formation of a uniform phase [13] :

$$SnS_2(s) \leftrightarrows {}^1/_2\, Sn_2S_3(s) + {}^1/_4\, S_2(g) \qquad \text{eq. 4.3}$$

$$Sn_2S_3(s) \rightarrow 2SnS(s) + {}^1/_2\, S_2(g) \qquad \text{eq. 4.4}$$

$$SnS(s) \rightarrow SnS\ (g) \qquad \text{eq. 4.5}$$

$$Sn_2S_3(s) + SnS_2(s) \rightarrow 3SnS(s) + 5S(g) \qquad \text{eq. 4.6}$$

These reactions predict that the presence of sulphur gas will suppress the formation of single phase SnS as SnS_2 and Sn_2S_3 will form. The properties of the SnS film according to their deposition conditions and post annealing conditions were analysed using the following techniques.

4.4.2 Results of Compositional and Structural Analysis

Energy-dispersive X-ray (EDX) Analysis

Energy-dispersive X-ray (EDX) was used to analyse for the elemental compositions of the film using a Zeiss SEM scanning electron microscope with the Bruker ESPRIT 1.8 system at an acceleration voltages of 5 kV. Compositional analysis plays a role in understanding the stoichiometry of the as deposited films indicating the temperature range required for the second step of this growth process. However, annealing in a sulphur atmosphere, as preformed in this work, will restore this issue. The variation of Sn to S atomic percent ratio of the SnS films with respect to the annealing temperature has been determined from the EDX studies. In the as-deposited films, the EDX spectra reveals amounts of unreacted Cl, in addition the Sn/S ratio was about 0.8, Table 4.2. The contamination was attributed to the adsorption of radicals produced from H_2S and $SnCl_4$ onto the surface. Higher temperatures facilitated desorption of these contaminants and so minimised chlorine incorporation into the thin film. As the annealing temperature increased the Sn/S ratio slightly decreased which can be attributed to the low energy formation of Sn_2S_3 than SnS phase and to the difference in vapour pressure between the Sn and S atoms [14]. At a temperature of 400 °C the samples tended toward a stoichiometric ratio of 0.93. The observed changes in the formation of the various phases, with the increase of annealing temperature were mainly due to the changes in the composition of the film, particularly sulphur incorporation into the film. The higher temperature can be favourable for the growth of tin disulphide SnS_2.

Table 4.2 Composition of H_2S annealed SnS thin films obtained by EDX.

Annealing temperature (º C)	Cl (at.%)	Sn (at.%)	S (at.%)	[Sn]/[S]
RT	31.04	31.34	37.62	0.833
350	-	35.87	58.20	0.72
400	-	48.15	51.85	0.93
450	-	42.44	57.56	0.73

X-ray Diffraction (XRD) Analysis

To investigate the structural properties XRD was performed, Figure 4.9 shows the grazing incidence XRD patterns of the annealed SnS films for the various annealing temperatures. The phases and crystal structure of thin films were examined by X-ray diffraction (XRD) (Rigaku-2000 X-ray diffractometer), using Cu-Kα radiation and an angle of incidence of 1.5418º. The 2θ-range for the diffractometer was set from 10^o to 80^o with a step size of 0.04. The amorphous phase of the as-deposited SnS samples is shown without any noticeable crystalline peaks related to any of the SnS phases. For the lowest annealing temperature 350 ^oC, the sample consists on an orthorhombic SnS phase with a XRD peak noted at a 2θ value of ~31.7 ^{o} which was assigned to the (111) plane of orthorhombic SnS phase (PDF. No 39-0354). However, small peaks at 28.6° and 31.9° indicate that a secondary phase is also present in the film. These peak position matched that of the Sn_2S_3 orthorhombic phase and according to the Inorganic Crystal Structure Database (ICSD), (JCPFS No. 01-14-619). When the annealing temperature was increased to 400 ^oC the XRD peaks for Sn_2S_3 phase completely disappeared, along with an increase in the intensities of the peaks from the SnS phase. At 400 °C well defined peaks at match with the standard of SnS. In addition, the peaks intensity has increased indicating an improvement in the crystallinity of the film and the growth of orthorhombic SnS grains which can be seen in SEM images, Figure 4.14. It has been reported that as the sulphur content increases the SnS film self-compensates as the number of Sn vacancies increase, with the Sn oxidation state changing from +2 to +4. This would lead to higher probability of the Sn_2S_3 forming as an impurity, with mixed oxidation states for Sn. The narrow structured XRD peaks depend on better crystallinity and larger grain size which are strong functions of the annealing temperature.

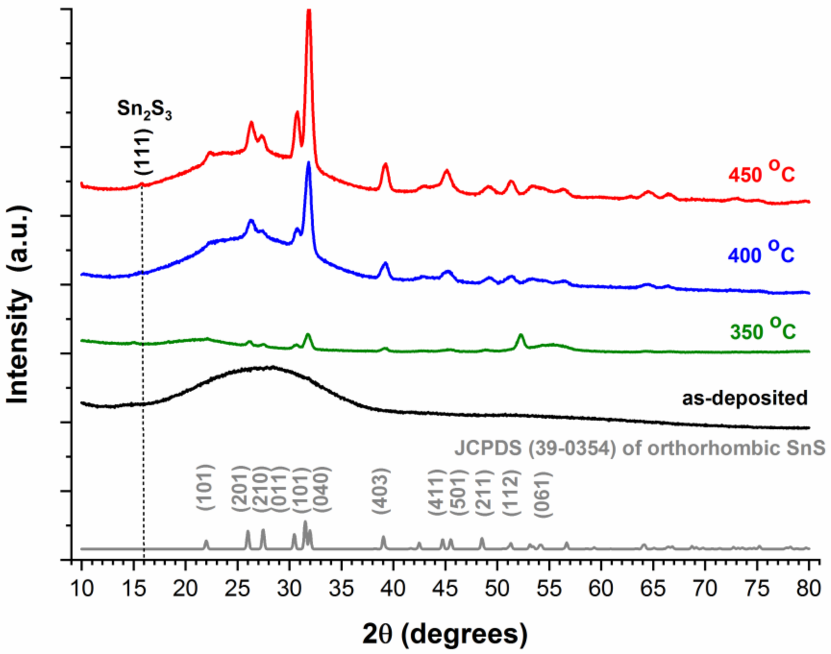

Figure 4.9 XRD patterns of SnS thin films annealed in H_2S atmosphere at different annealing temperatures.

It can be seen in Figure 4.10 that the similarities in diffraction patterns of the three SnS phases can lead to difficulties in distinguishing any traces of SnS_2 and Sn_2S_3 in the samples as the dominant Sn_2S_3 peak (211) overlaps the (400) peak of the desired SnS. Similarly SnS_2 (112) peak overlaps the (020) at ~ 42°.

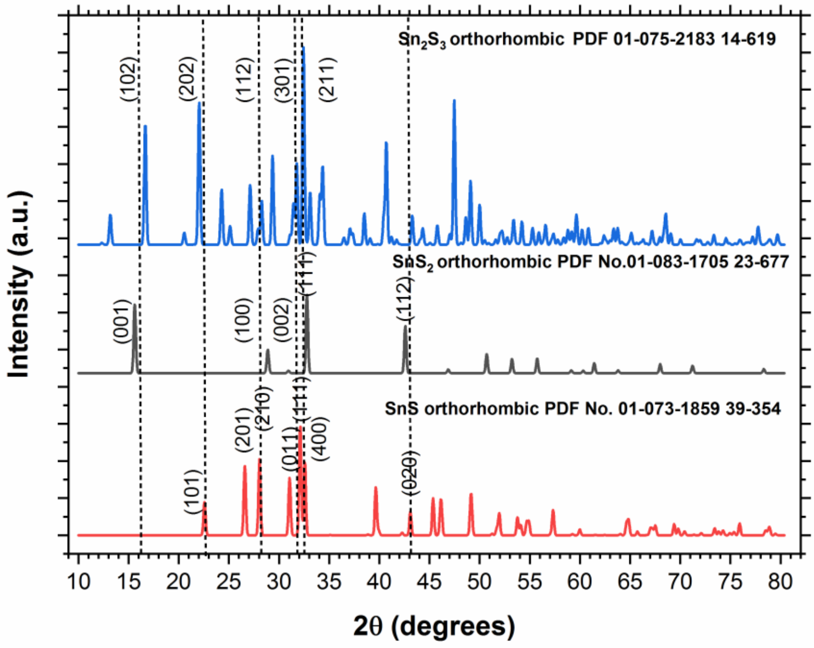

Figure 4.10 Standard XRD patterns for SnS, Sn_2S_3 and SnS_2 extracted from ICSD.

Therefore, another tool for characterising the impurity incorporation was required and Raman spectrometry was preformed to provide more information about the quality of the SnS films.

Raman Spectroscopy

A spectroscopic analysis was performed to more clearly identify the phases contained in each annealed thin film. This was carried out with a Raman spectrometer (Renishaw inVia system) in the backscattering configuration using a 50X objective lens, and diode-pumped solid state laser at λ=633 nm with n excitation power of 42.5 mW.

Generally, IV-VI compounds with an orthorhombic crystal structure exhibits 24 vibrational modes, which are represented by the following equation at the centre of the Brillouin zone as:

$$\Gamma = 4A_g + 2B_{1g} + 4B_{2g} + 2B_{3g} + 2A_u + 4B_{1u} + 2B_{2u} + 4B_{3u} \qquad \text{eq. 4.7}$$

On the other hand, SnS has 21 optical phonon modes of which, 12 are Raman active ($4A_g$, $2B_{1g}$, $4B_{2g}$ and $2B_{3g}$), 7 are infrared active ($3B_{1u}$, $1B_{2u}$ and $3B_{3u}$) and 2 are inactive ($2A_u$). The literature reported data on SnS single crystals showed that it exhibits nine longitudinal optic (LO) modes at 40cm^{-1}, 49 cm^{-1}, 78 cm^{-1}, 85 cm^{-1}, 160 cm^{-1}, 192 cm^{-1}, 208 cm^{-1}, 218 cm^{-1} and 290 cm^{-1}, and three transverse optic (TO) modes at 95 cm^{-1}, 178 cm^{-1} and 277 cm^{-1} [15, 16]. According to DiMare et al. vibrational frequencies for SnS occurred below 300 cm^{-1} [17]. For all the annealed samples the Raman spectra showed no peaks over 400 cm^{-1}. Indicating no traces of SnO_2.

Figure 4.11 shows a comparison of the Raman spectra of SnS_2, Sn_2S_3 and SnS. The Raman spectra of SnS_2 phase show two bands at 312 and 215 cm^{-1} , Figure 4.11 (a). The Raman spectra in Figure 4.11 (b) shows peaks at 251, 234, 183, 71, 60, and 52 cm^{-1}. This corresponds to the Raman reference spectrum for Sn_2S_3. The last spectra showed a very different Raman pattern, with bands at 288, 220, 189, 163, and 96 cm^{-1}. This pattern corresponds exactly to that given by a single crystal of SnS [16]. Figure 4.12 shows the Raman spectra of the annealed samples. Calibration of the spectrometer was performed by measuring the 520 cm^{-1} Raman line of the silicon wafer. Baseline correction has been applied to Raman graphs to subtract back round. The sample annealed at 350 ^{o}C shows multi-phase containing a peak at 307 cm^{-1}, which is in close agreement with reported Raman data to the Sn_2S_3 phase, and broad peaks at 158 cm^{-1}, 182 cm^{-1}, 224 cm^{-1} presenting the appearance of traces of the SnS phase [2, 18]. Increasing further temperature, two types of phonon modes assigned to A_g and B_{3g} of SnS (highlighted with blue in figure 4.3) are clearly seen at the samples annealed at 400 ^{o}C. The A_g Raman peaks are located at 186 cm^{-1} and 220 cm^{-1} , and the B_{3g} Raman peaks are located at 162 cm^{-1}. These peaks match very well with those in the previous study on bulk single-crystalline SnS [19-21].

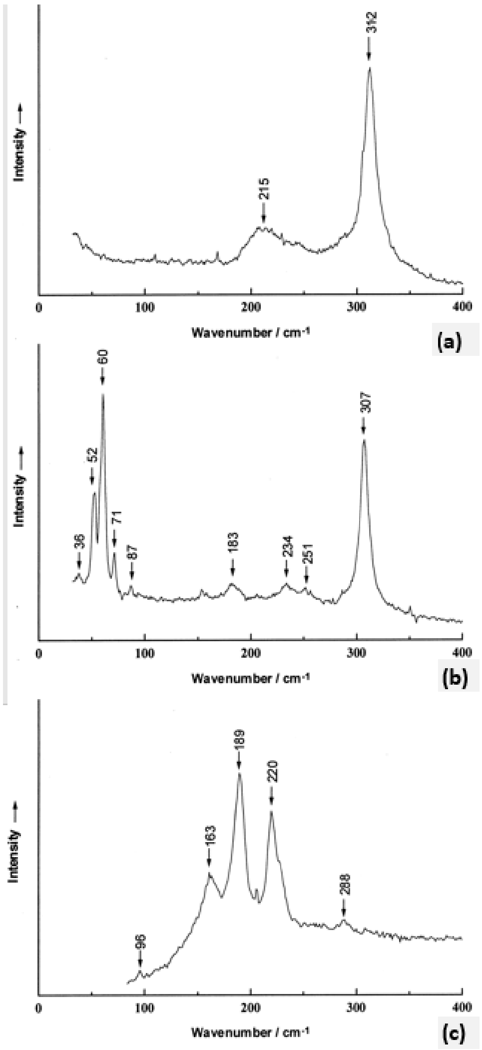

Figure 4.11 Raman spectra of (a) SnS_2 (b) Sn_2S_3 (c) SnS [16].

According to the reaction of equation 4.4, the formation of SnS from Sn_2S_3 and H_2S vapour may be interpreted as the result of the dissociation as defined in the equation. As the annealing temperature goes to 450 ^oC and additional H_2S encourages the increase of the sulphur content in the composition which leads to the appearance of a 312 cm^{-1} peak which corresponds to the SnS_2.

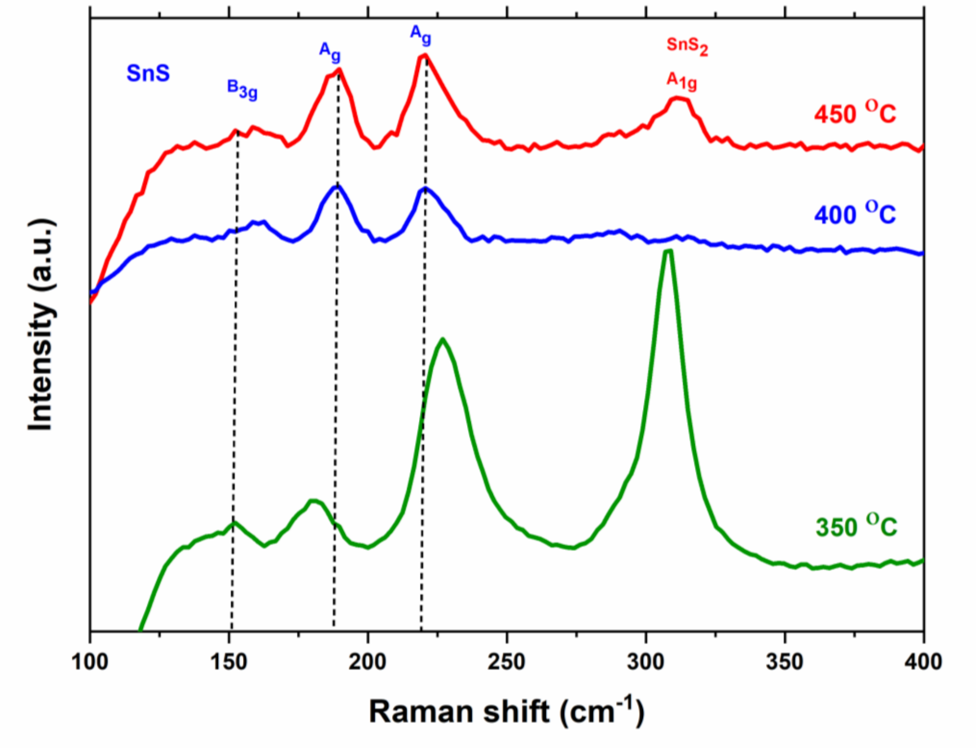

Figure 4.12 Raman spectra of the samples annealed at various temperatures.

Fluorescence background of SiO_2/Si substrate can appear in some of the Raman spectroscopy in this thesis. Such fluorescence background occurs if the substrate is excited to the higher electronic state by the absorption of a photon and subsequently relaxes back to the ground electronic state by emitting a fluorescence photon. The silicon Raman peak at 520 cm^{-1} is appearing sharp when the films are amorphous. As the annealing temperature increases the films crystalline and the Si peak appearance decreases. The Raman Si peaks were used as a reference showing the improvements in crystallinity of the annealed SnS films in some graphs in this thesis

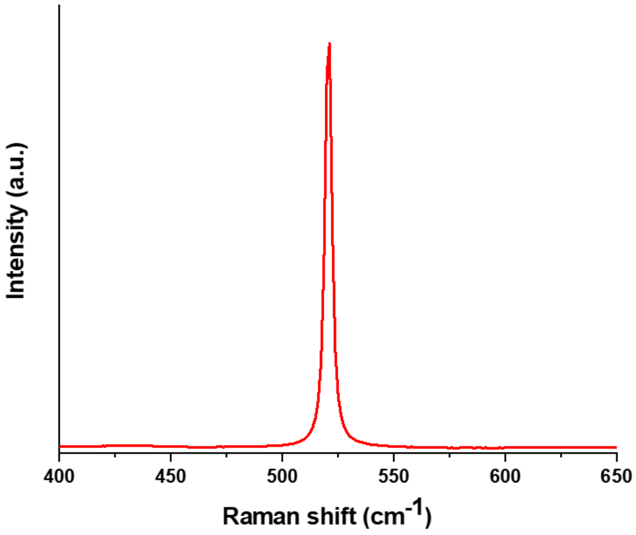

Figure 4.13 Raman spectra of the Si wafer at 520 cm^{-1}.

It is clear that a temperature of 400 °C is required for the complete reaction of the precursors, and the formation of the pure SnS phase. Annealing at temperatures above 450 °C resulted in an apparent mass loss due to evaporation of SnS from the films. Therefore pure single-phase SnS thin films were successfully synthesized.

SEM analysis

The surface topology of the SnS films annealed at different temperatures is examined with SEM and the images are shown in Figure 4.14. The images demonstrate that there is good surface coverage, good crystallinity and no cracks (pin hole) on the surface of the films. It was found that with increasing annealing temperature a change in the growth of grains is observed. The crystallites are packed densely and grown with different sizes in different directions. The images show that annealed samples exhibit a grain structure uniformly distributed and experience secondary grain growth. The crystals grain sizes ranging from 300 and 500 ± 50 nm. The improvement in crystallinity and grain size at higher temperature is associated with the decrease of grain boundaries. Thus it has been seen annealing at temperatures above 500 °C resulted in an apparent mass loss due to evaporation of SnS. Film thickness after annealing was estimated at 404 nm by SEM cross-section analysis, Figure 4.15.

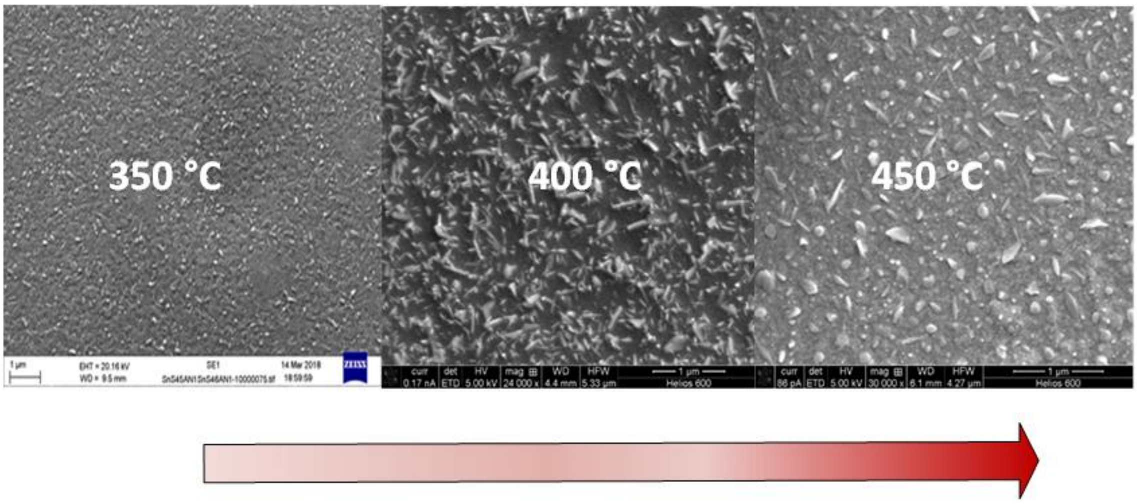

Figure 4.14 SEM images of the films annealed at various temperatures.

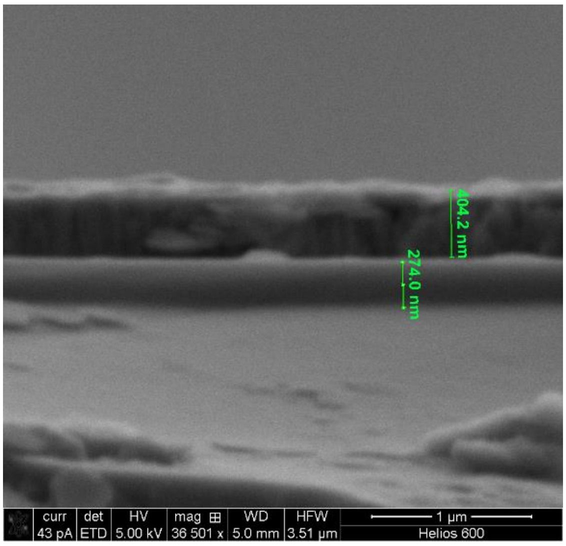

Figure 4.15 SEM cross section of the sample annealed at 350 °C on soda lime substrate.

4.5 Conclusions

This chapter demonstrates a simple novel two step method, for the growth of smooth amorphous SnS thin films by CVD at room temperature and followed by an H_2S annealing at controlled temperatures. Before synthesis, thermodynamic calculations of the reactions from precursors was performed. According to the thermodynamic calculations, the formation of SnS_2 is more favourable at room temperature. The ΔG for the formation of SnS_2 is negative in the temperatures range between 25-500 °C. In contrast, the change in Gibbs free energy for the formation of SnS is positive at the same temperature range. This seems contradictive with the above experimental results. Thus, we can principally exclude the formation of SnS from the direct reaction of $SnCl_4$ and H_2S. By adjusting the deposition conditions of the $SnCl_4/H_2S$ CVD process, uniform, pinhole free thin films are grown. The impact of $H_2S/SnCl_4$ concentration ratio on the formation of thin films was studied. A higher $H_2S/SnCl_4$ concentration ratio was found to increase the formation of good quality SnS thin films. The XRD patterns of the as-deposited films shows the amorphous nature of the films which can be related to the halide element in the composition of the films gown at room temperature. A second step was required to adjust the Sn/S stoichiometry and for the removal of the unreacted chlorine. Moreover, the annealing step was required to promote grain growth and reduce grain boundaries which is procedure frequently used to improve the material property of an absorber layer. The above results emphasized that annealing the films in H_2S atmosphere at 400 °C changes the stoichiometry of the as-deposited SnS films and leads to the formation of single phase SnS films. In conclusion, the present scheme to prepare high-quality SnS films is useful for fabricating PV devices which will be shown in the next chapter.

4.6 References

[1] H. M. Manasevit, "The Use of Metalorganics in the Preparation of Semiconductor Materials IV . The Nitrides of Aluminum and Gallium," *Journal of Electrochemical Society,* vol. 118, 1971.

[2] R. E. Banai, J. C. Cordell, G. Lindwall, N. J. Tanen, S.-L. Shang, J. R. Nasr*, et al.*, "Control of Phase in Tin Sulfide Thin Films Produced via RF-Sputtering of SnS2 Target with Post-deposition Annealing," *Journal of Electronic Materials,* vol. 45, pp. 499-508, January 01 2016.

[3] C.E.Morosanu, Thin Films Science and technology, Thin films by Chemical Vapour Deposition vol. 7: Elsevier, Amsterdam, 1990.

[4] C. C. Huang, F. Al-Saab, Y. Wang, J. Y. Ou, B. Gholipour, and D. W. Hewak, "Nanoscale MoS2 thin films fabricated by atmospheric pressure chemical vapour deposition at ambient temperature," 2013.

[5] B. Chapman, Glow Discharge Processes: Sputtering and Plasma Etching. Canada: John Wiley & Sons, 2016.

[6] C. V. Thompson, "Grain Growth in Thin Films," *Annual Review of Materials Science,* vol. 20, pp. 245-268, 1990.

[7] K. T. R. R. Reddy, P. P.; Datta, P. K.; Miles, R. W, "Formation of Polycrystalline SnS Layers by a Two-Step Process," *Thin Solid Films,* vol. 403-404, p. 116−119, 2002.

[8] K. M. T. Minemura, K. Noguchi, K. Ohtsuka, H. Nakanishi, and H Sugiyama, "Preparation of SnS Films by Low Temperature Sulfurization," *Physics Status of Solidi C,* vol. 6, p. 1221−1224, 2009.

[9] V. Steinmann , R. Jaramillo , K. Hartman , R. Chakraborty , R. E. Brandt , J. R. Poindexter, Y. Seog Lee , L. Sun , A. Polizzotti , H. Hejin Park , R. G. Gordon , and T. Buonassisi, "3.88% Efficient Tin Sulfi de Solar Cells using Congruent Thermal Evaporation", Advanced materilas, vol. 26, pp. 7488-7492, 2014.

[10] D. C. Lee Burton, Ruben Abellon, Ferdinand Grozema , L M Peter, Tom Savenije , Gilles Dennler, A Walsh, "Synthesis, Characterization, and Electronic Structure of Single-Crystal SnS, Sn_2S_3, and SnS_2," *Chemistry of Materials,* vol. 25, 2013.

[11] A. F. d. C. M.G. Sousa, P.A. Fernandes, "Annealing of RF-magnetron sputtered SnS_2 precursors as a new route for single phase SnS thin films," *Journal of Alloys and Compounds* vol. 44, pp. 80-85, 2014.

[12] B. H. Baby, Vaisakh, V. M.,Bharathi Mohan, D., "Fabrication and phase characterization study of SnS thin films under controlled sulfur deposition temperature," *Materials Today: Proceedings,* vol. 3, pp. 2077-2084, 2016.

[13] P. M. a. B. L. P. M. Nikolic, "Splitting and coupling of lattice modes in the layer compound SnS," *Journal of Physics C: Solid State Physics,* vol. 10, p. L289, 1977.

[14] H. R. Chandrasekhar, Humphreys, R. G. and Cardona, M., "Pressure dependence of the Raman spectra of the IV-VI layer compounds GeS and GeSe," *Physical Review B,* vol. 16, pp. 2981-2983, 1977.

[15] S. Di Mare, Menossi, Daniele, Salavei, Andrei, Artegiani, Elisa, Piccinelli, Fabio, Kumar, Arun, Mariotto, Gino and Romeo, Alessandro, "SnS Thin Film Solar Cells: Perspectives and Limitations," *Coatings,* vol. 7, p. 34, 2017.

[16] L. S. Price, I. P. Parkin, M. N. Field, A. M. E. Hardy, R. J. H. Clark, T. G. Hibbert, et al., "Atmospheric pressure chemical vapour deposition of tin(ii) sulfide films on glass substrates from Bun3SnO2CCF3 with hydrogen sulfide," Journal of Materials Chemistry, vol. 10, pp. 527-530, 2000.

[17] H. R. Chandrasekhar, Mead, D. G., "Long-wavelength phonons in mixed-valence semiconductor $Sn^{II}Sn^{IV}S_3$ " *Physical Review B,* vol. 19, pp. 932-937, 1979.

[18] J.-H. Ahn, Lee, Myoung-Jae, Heo, Hoseok, Sung, Ji Ho, Kim, Kyungwook, Hwang, Hyein and Jo, Moon-Ho, "Deterministic Two-Dimensional Polymorphism Growth of Hexagonal n-Type SnS_2 and Orthorhombic p-Type SnS Crystals," *Nano Letters,* vol. 15, pp. 3703-3708, 2015/06/10 2015.

[19] Z. Tian, Guo, Chenglei, Zhao, Mingxing, Li, Ranran and Xue, Jiamin, "Two-Dimensional SnS: A Phosphorene Analogue with Strong In-Plane Electronic Anisotropy," *ACS Nano,* vol. 11, pp. 2219-2226, 2017.

[20] H. R. Chandrasekhar, Humphreys, R. G., Zwick, U. and Cardona, M., "Infrared and Raman spectra of the IV-VI compounds SnS and SnSe," *Physical Review B,* vol. 15, pp. 2177-2183, 02 1977.

[21] C. V. Thompson, "Grain growth in thin films," *Annual Review of Materials Science,* vol. 20, pp. 245–268 1990.

[22] P. Sinsermsuksakul, J. Heo, W. Noh , A. S. Hock and R. G. Gordon, "Atomic Layer Deposition of Tin Monosulfide Thin Films", Advanced Energy Materials, vol. 1, 2011.

[23] H. Choi, J.Lee , S. Shin, J. Lee, S. Lee, H. Park, S. Kwon, N. Lee, M. Bang, S.Lee, and H.Jeon, "Fabrication of high crystalline SnS and SnS_2 thin films, and their switching device characteristics", Nanotechnology, vol. 29, 2001.

Chapter 5 Design, Fabrication and Characterization of p-SnS/n-Si Heterojunction by CVD

5.1 Introduction

The aim of this chapter, is to demonstrate the potential of using the novel CVD fabrication method (discussed in Chapter 4) to build heterojunction structures. To form a heterojunction, the SnS layers were grown on an n-type silicon substrate. Due to intrinsic p-type semiconducting property of SnS, the heterojunction was simultaneously formed by the growth of SnS on the *n*-type Si. The heterojunction device exhibited excellent photovoltaic characteristics which confirmed that the CVD fabrication method is a route that can be applied for photo electronic devices such as solar cells. The photovoltaic characteristics of SnS/n-type Si are evaluated and reported in this chapter.

5.2 Device Fabrication Process

The device characterisation and fabrication steps are discussed below. SnS was deposited by a bilayer method (two depositions). Figure 5.1, shows a schematic diagram of the device configuration fabricated in this chapter and a scanning electron microscopy (SEM) image of cross section of the SnS thin films. This configuration was used to investigate the electrical properties of the SnS films. Contact to silicon is made with aluminium from the backside whereas SnS is deposited on the front side and contacted by gold. This configuration has the substrate structure of a solar cell where illumination is applied on the front SnS side [1].

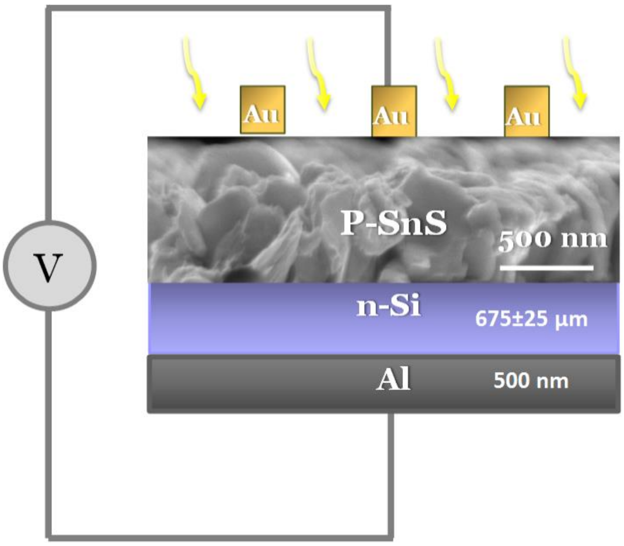

Figure 5.1 Schematic of SnS/n-Si heterojunction solar cell.

5.2.1 Substrtate Preperation

SnS thin films were deposited on (100)-oriented n-type silicon substrates (20 × 20 mm^2) with thickness of 675 ± 25 µm and a resistivity of 10 -30 Ω cm. Before depositing the films the substrates were ultrasonically cleaned in sequence by acetone, isopropanol (IPA) and then finally rinsed with deionized water. After sonication the substrates were dipped into a buffered HF solution (20:1) for 60 seconds to remove the native oxide layer from the substrates surface. After that, substrates were immediately loaded in the quartz tube of the CVD apparatus for deposition.

5.2.2 Growth of SnS Absorber Layer

SEM images of the SnS films grown by CVD (see section 4.4.2) show that the morphology of the films is composed of granular plate-like features. To ensure that there are no gaps between the grains that prevent conduction reducing the efficiency of devices, a double layer of SnS deposition was applied in this work. The basic idea was to form high density films by stacking two layers of the thin film. We test this approach on SnS thin-film heterojunction as a proof-of-concept.

A performance loss analysis of SnS solar cell suggests that the device performance is affected by a low shunt resistance which reduces the fill factor and open circuit voltage [2]. The low shunt resistance might result from pinholes in the SnS bulk and current pathways around the edges of the device. The two-step deposition method will allow the use of more conductive buffer layers in substrate-style device configurations.

Using multiple layers to improve device performance has been investigated by Theissmann et al. who noticed an improvement in device performance when coating a second layer of ZnO which could be due to an improved layer morphology in terms of density and interface smoothness [3]. Tellier et al. observed that while increasing the number of depositions when depositing ZnO thin films higher density films are obtained and the conductivity of multiple layer ZnO films improves [4]. Further studies have focused on approaches to improve the electrical and optical properties of thin films describing what is happening on a morphological level and why the additional layers improve the films over coating single, thick layers, are absent [2-4]. Moreover, the bilayer process leads to larger grain sizes compared with a single-stage process which can be seen alter in the SEM images [5,6].

SnS thin films were prepared consisting two layers. Both layers were deposited using the optimized growth conditions of the CVD procedure mentioned previously, see Chapter 4. Subsequently, the second layer was deposited using the same method. Each layer had a thickness of ~450 ± 50 nm (measured after the post-annealing step).

In order to ensure the phase purity of the SnS thin films, the composition and electrical properties of each layer were characterised. (XRD) analysis of the synthesized SnS film confirmed the formation of a single phase SnS phase for both layers, XRD analysis detected no impurities such as SnO_2 and SnS_2 on either layers, Figure 5.2 XRD of bilayer SnS thin films on n-type silicon substrates. It is observed that, all diffraction patterns belong to the SnS (JCPFS. No 39-0354) with preferential orientation along the (040) plane.

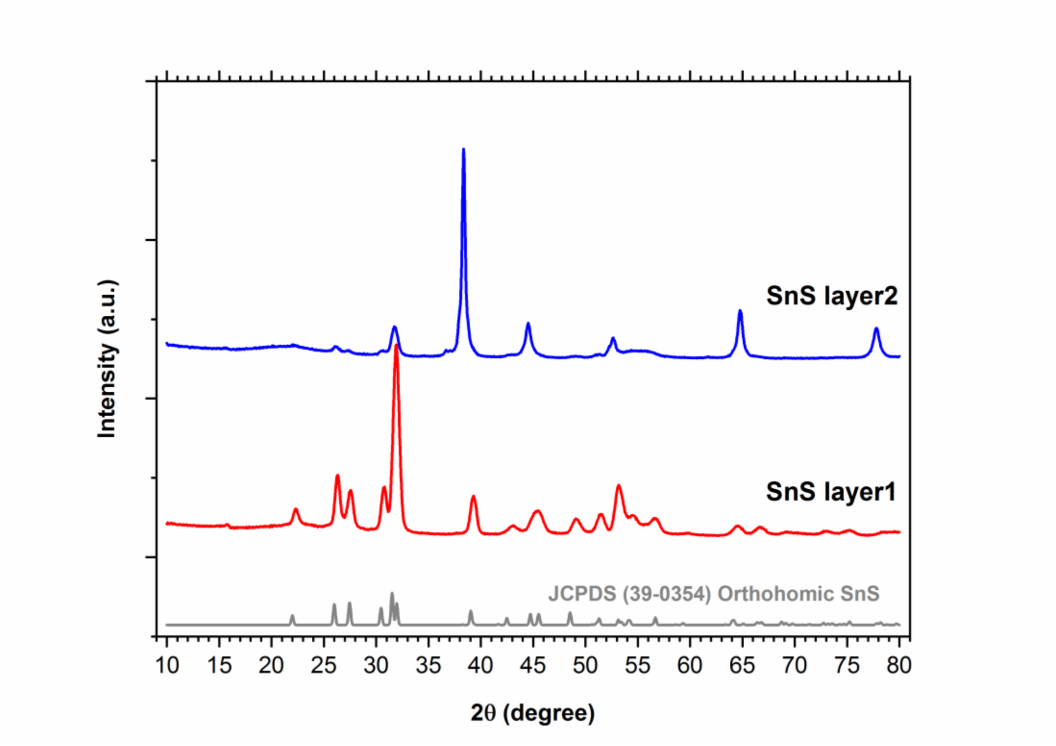

Figure 5.2 XRD of bilayer SnS thin films on n-type silicon substrates.

It also indicates that SnS crystallites grown at second-step are preferentially oriented along the (311) orientation. Devika et al. reported that the substrate has a strong influence on the structure of SnS [10]. EDX was carried out on both layers. Figure 5.3 shows the EDX spectrum and the atomic composition ratio estimated from the spectra. EDX reveals that both layers consist of Sn/S atomic % ratio of around 1.

Number of Layer	Cl (at.%)	Sn (at.%)	S (at.%)	[Sn]/[S]
First Layer	-	50.77	49.23	1.03
Second layer	-	50.57	49.43	1.02

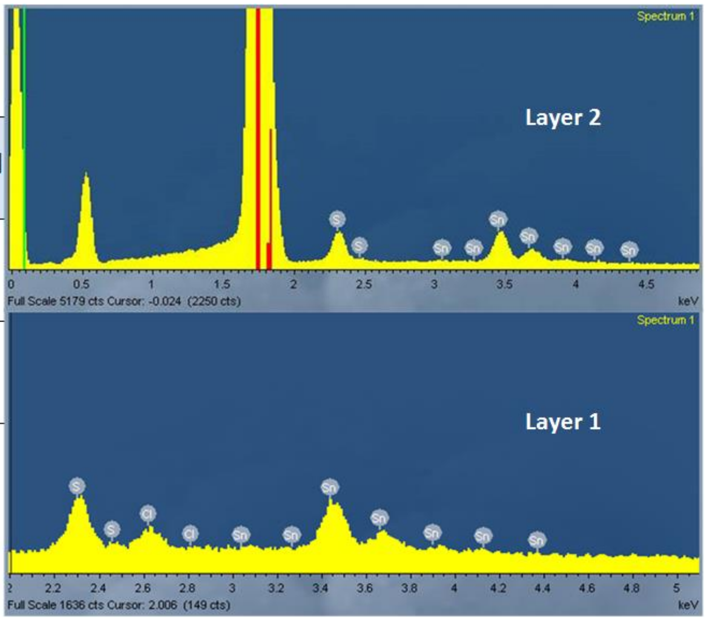

Figure 5.3 Energy Dispersive X-ray Analysis (EDX) of bilayer SnS thin films.

This indicates that the SnS layers have stoichiometric chemical composition between the two constituents. No traces of chlorine contamination was found in any layer.

The observed Raman spectra of both layers shows peaks related to the corresponding lines of SnS, Figure 5.4. The intensity of the lines for the second layer of SnS is relatively high and sharper, which emphasizes the effect of substrate on the morphology of the thin film. Importantly, we could not observe any peak related to either its binary phases like SnS_2 and Sn_2S_3 or other impurities. Therefore, both SnS layers contain purely SnS phase. These results are quite consistent with the XRD data. The surface structure of the films grown on the SnS thin film (the second layer) shows denser surface than that of the first layer of SnS films grown, Figure 5.4.

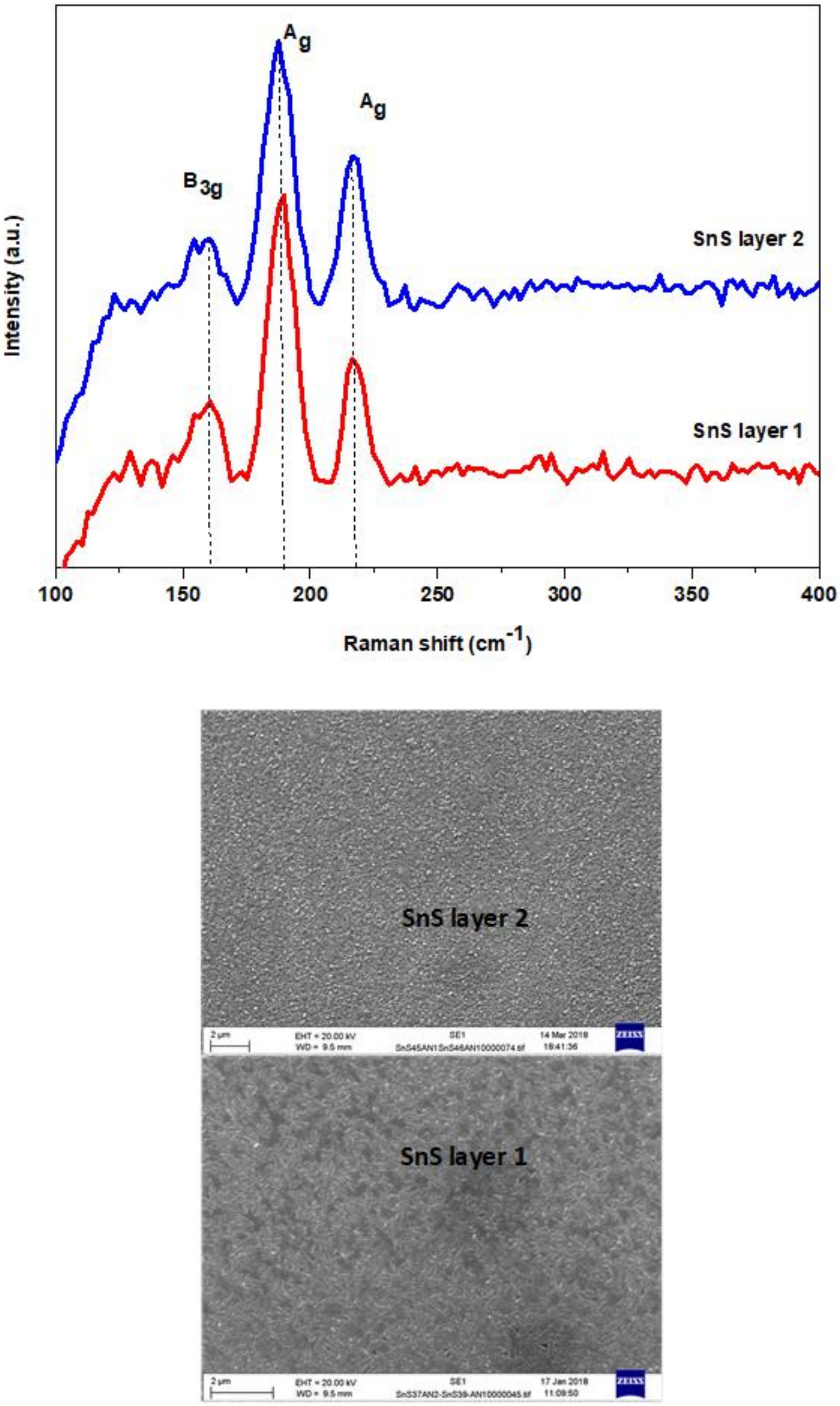

Figure 5.4 Raman spectra and SEM images of both layers of SnS thin films.

5.2.3 Front Contact Deposition

Gold contacts were deposited on the surface of SnS thin films, referred to as “front contacts.” All the front contacts described within this thesis were patterned by conventional optical lithography, metallization and lift-off using a dark field mask designed by the author and fabricated by

Compugraphics Ltd. The mask used contains a series of rectangular pads (1599 × 1697 ±5 µm). A positive S1813 photoresist (Shipley) was applied to the surface of SnS to pattern the surface using a spin-coating machine to prepare for pattering the surface. The samples were spun at high-speed (4500 rpm) for a period of 45 seconds. The spinning resulted in a photoresist of ~1.3 µm on the devices front surface. After that, samples were baked on a hotplate at 110 °C for 30 seconds for cross linking the resist. The samples were then exposed using filtered Hg lamp source with an exposure dose of 144 mWs/cm^2 and then developed in MIF 319 developer for 45 sec.

Metal contacts were deposited using an e-beam evaporator at room temperature. 5 nm of chromium (Cr) was deposited prior to gold as an adhesive layer. Gold electrodes were then deposited and both depositions were performed under a high vacuum of 1.05 X10^{-5} Torr at a deposition rate of 0.05 and 0.03 Å/s for Cr and Au respectively. The devices were subsequently left in acetone until lift off was complete, Figure 5.5.

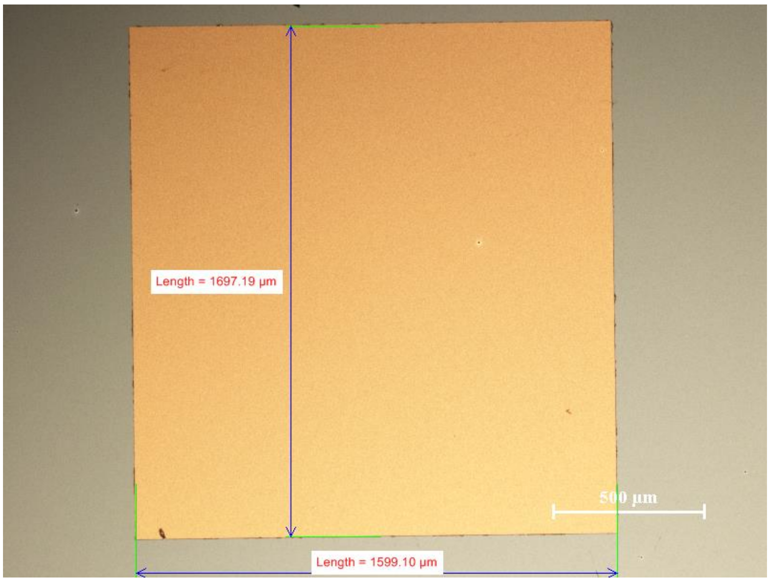

Figure 5.5 Optical microscope image of the Cr/Au (5nm/50nm) contacts deposited on SnS film.

The choice of metal is often dependent on the work function of the metal (ϕm) and semiconductor (ϕs). The work function of a metal is the energy required to remove an electron from its surface to the vacuum immediately outside the surface. The Fermi level of metals falls or pins between the valence and conduction bands of SnS. For a semiconductor, the work function is defined as:

$$\varphi_s = \chi_s + (E_c - E_F) \qquad \text{eq. 5.1}$$

where χs is the electron affinity of the semiconductor and E_F is the Fermi energy level. The energy band diagram of SnS film and metal SnS junction after formation is shown in Figure 5.6 [8]. In general, the metal contacts whose work function (ϕ_m) is closer to SnS work function (ϕ_s =4.2 eV) and/or greater than the electron affinity of (χ_s =3.14 eV) (i.e. $\phi_m \geq \chi$) can establish Ohmic or non-rectifying junction with SnS since their Fermi level exactly pins between conduction and valance bands. Thus, high work-function metals are expected to form low-resistance, Ohmic contacts with SnS. Gold (Au), with its high work function, would be expected to provide low-resistance contact to p-type semiconductors, such as SnS [9-11]. The electrical characterisation of the device was carried out with the Keysight B1500A semiconductor analyser. The illumination source was a continuous-wave laser installed in the semiconductor analyser (633 nm, output power of 0.85 mW). Obviously, the fabricated device does not have a solar cell configuration, therefore the heterojunctions fabricated were not tested under a solar simulator. The I-V curves were obtained by introducing voltage sweeps between and measuring the current across the sample.

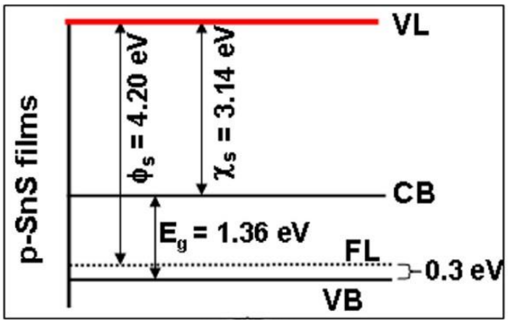

Figure 5.6 Energy band diagram of SnS film and metal structure [6].

There are few groups also studied the performance of SnS based devices using different non alloyed ohmic contacts. Noguchi et al. fabricated a SnS solar cell using Ag as an Ohmic contact and obtained a conversion efficiency of ~0.3% [12]. Yang et al. measured the contact resistivity between SnS thin films and three different metals (Au, Mo and Ti). They found that the contact resistance increases in the order Au< Mo< Ti, the contact resistance for Au and Mo are low enough so that they do not significantly decrease the efficiency of solar cells based on SnS as an absorber [13].

The current versus voltage characteristics of the M/SnS were measured are shown in Figure 5.7.

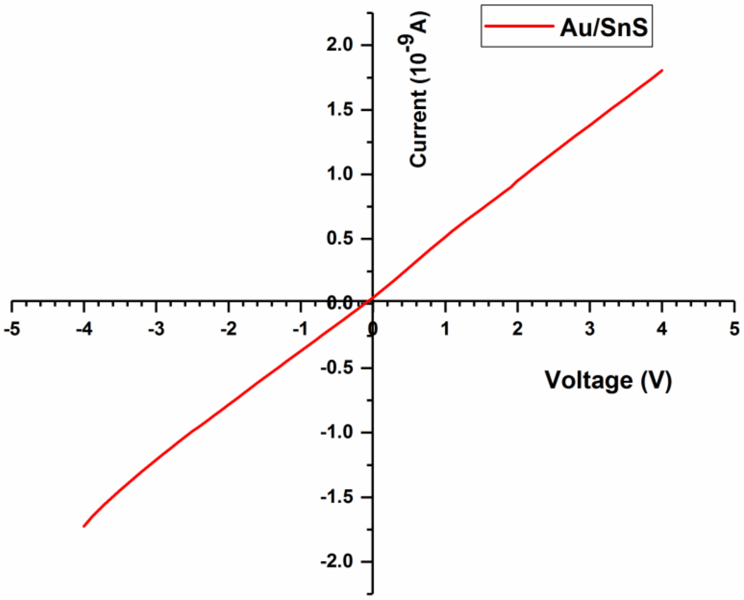

Figure 5.7 IV plot of Au/SnS measured at room temperature.

I-V measurements showed that Au formed Ohmic contacts with SnS, which is consistent with earlier findings Ohmic behavior with SnS film over the wide range of voltage varied from −5 to 5V.

5.2.4 Back Contact Deposition

The last important layer in the device is the back contact. This material must make an Ohmic contact with the junction material in order to minimize losses in device function. Therefore, selection of the back contact metal is based on the electronic properties of both the metal and semiconductor. The formation of back contacts to silicon solar cells by aluminium is well known method in industrial application, due to its high throughput (work function is 4.25 ± 0.05 eV) [9, 10, 11]. The removal of the oxide from the wafer directly before aluminium deposition ensured that there was no ‘native’ oxide between the aluminium and silicon. A positive S1813 photoresist (Shipley) of 1.3 µm was applied to the surface of Au/SnS to protect the front face of the heterojunctions at 4500 rpm and soft baked at 110 °C. The heterojunctions back surface native oxide was further removed by reactive ion etching (RIE) using suitable recipe (oxygen O_2 (5 sccm), Ar (10 sccm) and CHF_3 (15 sccm) using a power of 200 W) for 15 mins. A 500 nm universal backside contact was depositing using aluminium metal as a back Ohmic contact by e-beam evaporation at an evaporation pressure of 4×10^{-5} Torr at an evaporation rate of 0.1 nm/min. The samples with deposited back contacts were then washed with acetone to remove the photoresist covering the front side of device area.

5.3 Device Characterisation

5.3.1 Current-Voltage (I-V) Measurements

To evaluate the electrical performance of the heterojunction, current-voltage curves (I-V) measurements at room temperature were carried out. The presented current-voltage curves were measured in a MEMS probe station. The sample temperature is at 21 °C and for the measurements under illumination a HeNe 633 nm laser with a total power of ~ 0.85 mW was used (power intensity of 1.35 W/cm^2).

The current-voltage characteristics of the SnS/n-type Si heterojunction under dark is shown in Figure 5.8 proving the action of p-n junction. The dark I-V curve exhibits diode like rectifying behaviour. Ohmic behaviour of Au contact to SnS (Figure 5.7) proves that the diode like characteristic stems from SnS/n-type Si heterojunction.

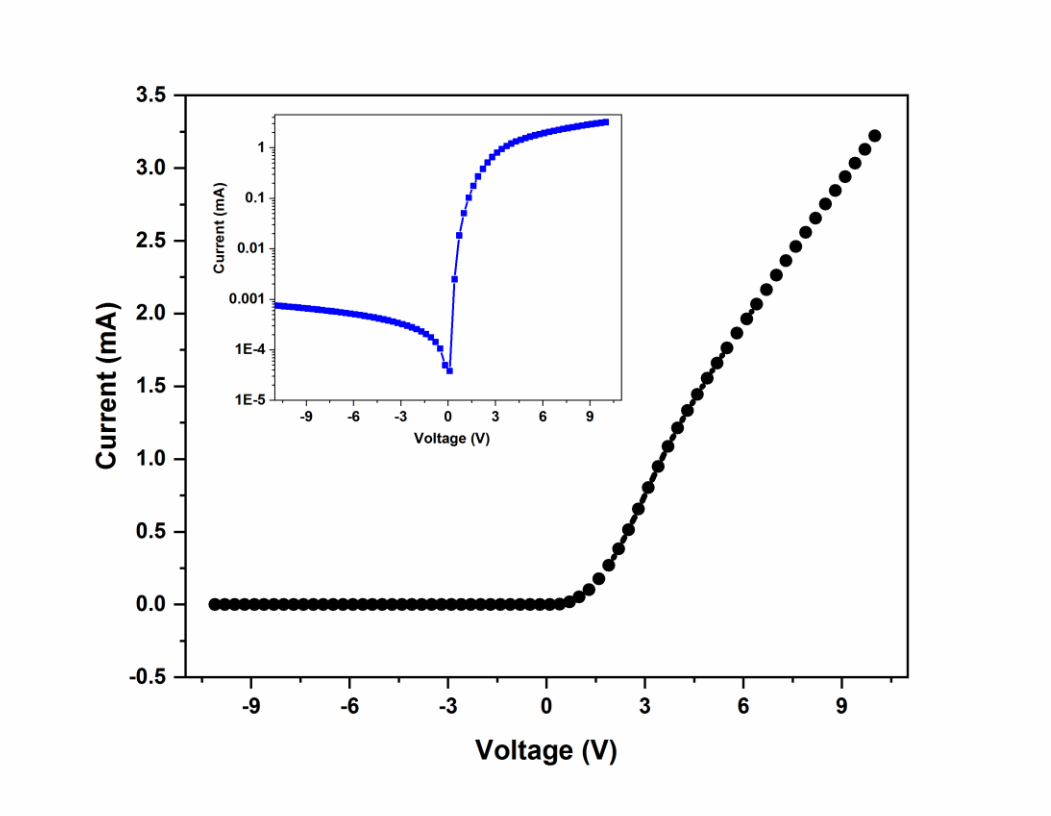

Figure 5.8 I-V curve of Au/SnS/n-type S/Al heterojunction under dark conditions showing clear current rectification (the inset shows the I-V plotted in semi-log scale).

The diode behaviour is a type II band alignment of heterojunction with an asymmetric I–V characteristic of rectifying behaviour which is attributed to the energy band bending in the heterointerface between the SnS thin film and the n-type Si substrate. SnS is considered to be p-type semiconductor intrinsically.

The diode parameters for the dark I–V relationship were determined by employing a non-linear implicit curve fitting method (section 2.3.2). The clear diode-like behaviour with current ratio of $>10^3$ at $\pm$ 4V reflects current rectification with a fairly low dark current (~ 1×10^{-3} A at -4 V). The turn-on voltage was found to be 1.3 V. From the dark characteristics of the graph diode quality factor was calculated to be 2.24 and the reverse saturation current has a value of 3.36×10^{-05} A. The ideality factor which is greater than unity implies the deviation from ideal diode. This deviation may be attributed to series resistance, barrier inhomogeneity.

Photovoltaic properties of heterojunction are investigated by illuminating the device with a 633 nm laser, Figure 5.9.

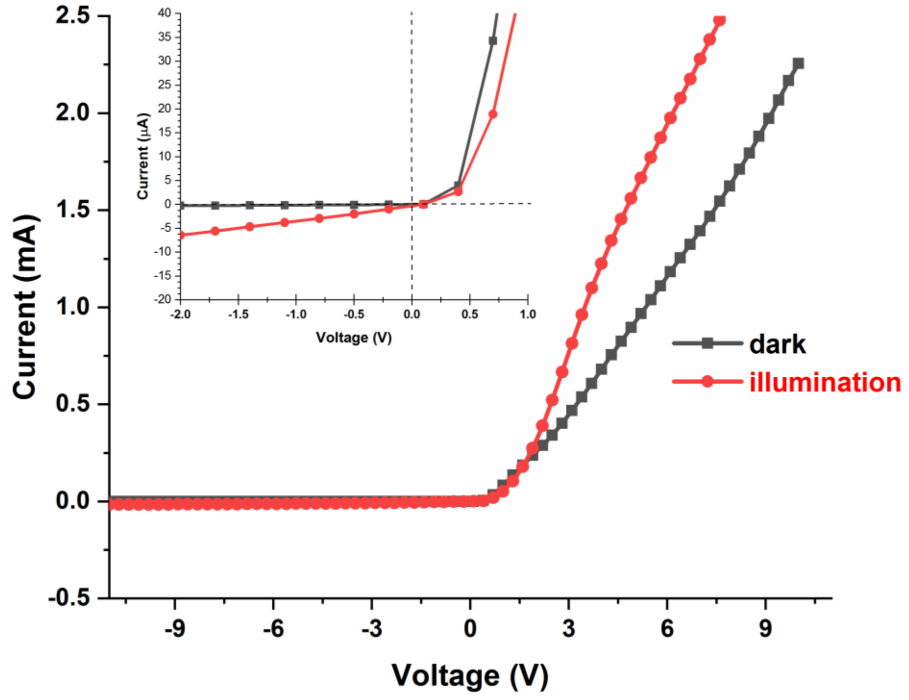

Figure 5.9 The I-V curve of SnS/n-Si under 633 nm laser illumination.

The photoresponse of the device was investigated and a photocurrent of 6.5×10^{-6} A was generated. The short-circuit current and the open circuit voltage under illumination were measured from Figure 5.10 and are 0.102 V and 3.3×10^{-7} A respectively. The fill factor is only 23%, which means that the device architecture need optimisation. It is believed that by designing a thin film solar cell structure, the conversion efficiency of SnS thin film solar cells will be enhanced greatly.

The spectral response and the quantum efficiency are both used in solar cell analysis. The spectral response is conceptually similar to the quantum efficiency. The quantum efficiency gives the number of electrons output by the solar cell compared to the number of photons incident on the device, while the spectral response is the ratio of the current generated by the solar cell to the power incident on the solar cell. The spectral respond of the fabricated devices in this thesis was found to be 0.08 and the quantum efficiencies is 0.16%. Both are low values which can be due to the architecture of the devices and band alignments between the different layers.

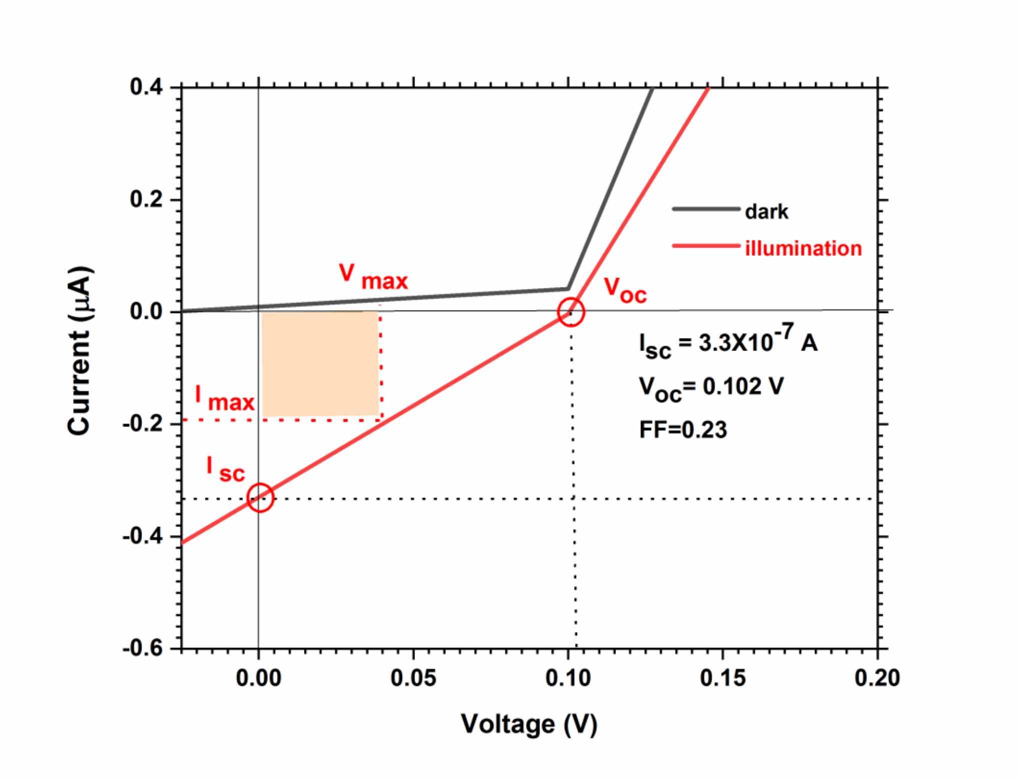

Figure 5.10 I-V characteristics of SnS/n-Si heterojunction solar cell under 633 nm laser.

5.3.2 Hall-Effect Mobility Measurements

Hall measurements are useful for extracting several electronic properties of a material and were applied in this thesis using a typical square Van der Paw structure at room temperature. Au contacts were deposited on post-annealed RF sputtered SnS thin films deposited on (100) n-type Si wafers. Contacts were spaced 5 to 10 mm apart. Contacts were checked prior to each Hall measurement by probing all combinations by sourcing current and measuring voltage. Films annealed below 400 °C were had high resistivity and their electrical properties could not be measured. The SnS films exhibited p-type conductivity with a Hall coefficient R_H of R_H, $+6.26\times10^{+03}$ m^2/C and a carrier concentration of $+1.66\times10^{+15}$ $/cm^3$. The mobility of about 1.7 cm^2/Vs and obtained for the SnS sample is which is relatively low when compared to the values reported in the literature for evaporated films [12]. This decrease in mobility can be a consequence of the film thickness which leads to carrier scattering at the grain boundaries as the grain size increases. This decrease in mobility can be a consequence of the film thickness which leads to carrier scattering at the grain boundaries as the grain size increases [13].

5.4 Conclusions

The results from the characterisation of the CVD films and devices showed that by using the double layer method it is possible to produce thin films of phase-pure SnS that are suitable for use in thin film solar cell structures. X-ray diffraction (XRD) analysis and micro-Raman studies confirm the formation of single phase SnS films. Hall effect measurements confirm the p-type nature of the SnS thin films with a mobility of 1.7 cm^2/Vs. SnS/n-type Si diode which are a type-II heterojunction have been fabricated. From the current-voltage measurements, the heterojunction exhibited diode like behaviour in dark. The diode shows typical rectification behaviour, the saturation current has a value of 3.36×10^{-05} A and the estimated diode factor of this junction was 2.24. Under illumination, the photoresponse behaviour of the device was explored and the device was highly sensitive to 633 nm laser. The heterojunction exhibited photovoltaic performance. The V_{OC} and I_{SC} are 0.12 V and 3.3×10^{-07} A respectively. This low photovoltaic performance can be due to conduction band offset, recombination at grain boundaries and interface defects. In addition, it was demonstrated that the presented method for SnS films can be employed to successfully fabricate photovoltaic cells and therefore is also suitable for photodetectors and optoelectronic heterostructures. Further improvements in the device structure can enhance the efficiency of the heterojunctions.

5.5 References

[1] K. Lal Chopra, S. Das (1983), “Thin film Solar Cells”, New York and London, Plenum Press.

[2] V.Steinmann, R. Jaramillo, K. Hartman, R. Chakraborty, R.E. Brandt, J.R. Poindexter, Y.S. Lee, L. Sun, A. Polizzotti, H.H. Park, R.G. Gordon, T. Buonassisi, “ 3.88% Efficient Tin Sulfide Solar Cells Using Congruent Thermal Evaporation”, Advanced Materials vol.26, pp. 7488−7492, 2014.

[3] R.Theissmann, S. Bubel, M. Sanlialp, C. Busch, G. Schierning and R. Schmechel, High performance low temperature solution-processed zinc oxide thin film transistor, *Thin Solid Films*, 2011, 519.

[4] J.Tellier, D.Kuscer,B.Malic,J.Cilensek,M.Skarabot,J.Kovac,G.Goncalves,I.Musevic and M.Kosec, “Transparent, amorphous and organics-free ZnO thin films produced by chemical solution deposition at 150 °C”, “*Thin Solid Films”*, vol. 518, pp 5134-5139,2010.

[5] E.J.J Martin, M. Yan, M. Lane, J. Ireland, C.R. Kannewurf and R.P.H.Chang, “Properties of multilayer transparent conducting oxide films”, “Thin Solid Films”, vol.461.pp 309-315, 2004.

[6] L. Ji, L. Huang, Y. Liu, Y. Xie, F. Liu, A. Liu and W.Shi, “Optical and electrical properties of zinc oxide/indium/zinc oxide multilayer structures”, “Thin Solid Films”, vol. 519, pp. 3789-3791, 2011.

[7] J. Kim, J. Moon, H. Kim and H. Lee, “Transparent Multilayer Indium-Zinc-Oxide Films Deposited by DC Sputtering” , “Journal of the Korean Physical Society”, vol. 55, pp. 1931-1935, 2009.

[8] R. Klenk, T. Walter, H. W. Schock, and D. Cahen, “A Model for the Successful Growth of Polycrystalline Films of $CuInSe_2$ by Multisource Physical Vacuum Evaporation,” Adv. Mater., vol. 5, pp. 114–119, 1993.

[9] J. R. Tuttle, M. A. Contreras, A. Tennant, D. Albin, and R. Noufi, “High efficiency thin-film $Cu(In,Ga)Se_2$-based photovoltaic devices: Progress towards a universal approach to absorber formation,” in Conference Record of the Twenty Third IEEE Photovoltaic Specialists Conference, pp. 415–421, 1993.

[10] M.Devika, N.Reddy, M.Prashantha, K.Ramesh, S.Venkatramana Reddy, Y.B.Hahn, and K.R.Gunasekhar, “The physical properties of SnS films grown on lattice-matched and amorphous substrates”, Physica Status Solidi A, vol. 207, pp. 1864–1869, 2010.

[11] H. Noguchi, A. Setiyadi, H. Tanamura, T. Nagatomo, and O. Omoto, “Characterization of vacuum- evaporated tin sulfide film for solar cell materials”, Sol. Energy Mater. Sol. Cells, vol.35, pp. 325–331, 1994.

[12] Chuanxi Yang, Leizhi Sun, Riley E. Brandt, Sang Bok Kim, Xizhu Zhao, Jun Feng, Tonio Buonassisi, and Roy G. Gordon, “Measurement of contact resistivity at metal-tin sulfide (SnS) interfaces”, “JOURNAL OF APPLIED PHYSICS 1”, vol. 122,pp 045303 ,2017.

[13] P. Sinsermsuksakul, J. Heo, W. Noh , A. S. Hock and R. G. Gordon, “Atomic Layer Deposition of Tin Monosulfide Thin Films”, Advanced Energy Materials, vol. 1, 2011.

Chapter 6 Synthesis and Characterisation of Single Phase Tin Sulphide Thin Films by RF sputtering via Post-Deposition Annealing Method

6.1 Introduction

Sputtering is suitable for the continuous deposition of high quality films in large-area. In this chapter, the method used for the growth of SnS thin films by radio frequency (RF)-magnetron sputtered thin films is presented. This method was applied as a comparative study to the SnS thin films deposited by the two step CVD method, discussed in Chapter 4.

To date, there are few reports of SnS sputtering in the literature, that explore a limited range of deposition and annealing conditions, as discussed in section 0. Previous reported results, established a baseline for producing SnS layers via (RF) sputtering of a SnS target [1-5]. One of the main methods to achieve stoichiometric SnS thin films reported in the literature has been by sputtering from a SnS_2 target by post-annealing treatment [1-3]. Due to the higher volatility of sulphur over tin when depositing from a SnS target, sulphur loss during deposition has been a concern. The challenge to maintain a 1:1 ratio of Sn:S requires excess sulphur in the deposition or post-annealing process to ensure the final stoichiometry of the material. Therefore, fin this work films deposited by using a SnS target, were post annealed in a sulphur environment to prevent sulphur loss. Johnson et al. reported that dark- and photo-conductivity of evaporated SnS thin films can be increased by post-deposition annealing [4]. J.R. Nasr et al. reported a study of the effect of post annealing in a sulphur atmosphere on structural and electrical properties. They found that pure SnS phase was obtained by annealing at 400 °C and 425 °C for 60 min and displayed strong p-type behaviour [5]. The literature points towards a favourable change in the quality of the SnS films after post-deposition annealing in a sulphur environment. Post-Annealing is a required process used to improve crystallinity and grow grains in absorber layers (Section 4.4). In addition, the highest efficiency SnS thin film solar cell recorded were annealed in H_2S atmosphere to form larger grains with fewer grain boundaries [6].

The aim of this work was to try to find a route to produce single phase SnS thin films from a SnS (50:50) target. Due to the targets 1:1 composition the as-deposited films are sulphur deficient as opposed to those sputtered from SnS_2 targets [1, 2]. Since sulphur is more volatile than tin, room temperature deposition, which allows for better stability, has been used to deposit SnS in this study. This step was followed by a post annealing treatment in an H_2S atmosphere. The post-annealing step was used to improve the materials electrical properties by promoting grain growth and reducing the number of grain boundaries that can catalyse recombination.

Few studies have investigated sputtered SnS, but none have fully explored the effect of post annealing parameters in H_2S atmosphere on the properties of the final films. A systematic and detailed study on the effects of the annealing conditions on the phase and composition of the tin sulphide films is discussed in this chapter. The effects of the post annealing step on the structural (including crystal structure, phase, composition, and morphology), optical and electrical properties of the grown films have been investigated. Only few studies have investigated sputtered SnS, and none have fully explored the parameters available for fabricating and treating the films for electronic applications. To the author’s knowledge, this is the first report of a study of the phase change as a result of post-deposition heat treatments sputtered from a SnS target.

6.2 Growth of SnS Absorber Layer by RF-Sputtering

6.2.1 Stoichiometry of Sputtering Target

The SnS target was obtained commercially from Testbourne Ltd. UK with a purity of 99.999% (2.00” diameter X 0.25” thick). EDX analysis was used to determine the composition of the target to compare with as deposited films, Figure 6.1.

Element	Atomic%
S	50.23
Sn	49.77
[Sn]/[S]	0.99
Totals	100.00

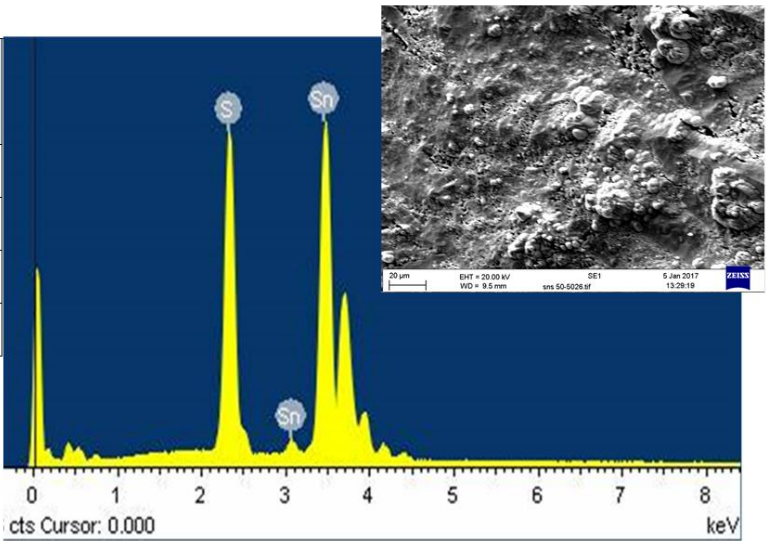

Figure 6.1 Energy dispersive X-ray of SnS (1:1) target showing atomic ratio of target elements and SEM image of SnS target.

EDX revealed a sulphur to tin target composition of Sn: 49.77 and S: 50.23 at. %. SnS layers were first deposited on n-type Si and soda lime glass (SLG) by RF sputtering. The deposition rate was 0.44 A° /sec.

6.2.2 Sputtering Conditions

Depositions took place in the IPC cleanroom using a Kurt J Lesker NANO38-SPUTTER thin film deposition system, described in Section 3.2.2. The pre-cleaned substrates were loaded into the sputtering chamber. SnS thin films were deposited on both quartz and n-type Si substrates (20 × 20 cm^2) at room temperature. High purity argon was used as the sputtering gas and the distance between the target and the substrate was 150 mm. A base pressure of 10^{-5} Torr was achieved prior to flowing the Ar gas. The RF power for film deposition also was varied between 35 to 50 W. To avoid any contaminants being deposited on the substrate and to stabilise the plasma, the target was pre sputtered for 10 minutes with the shutter closed. All films were deposited at a base pressure range of $1–6 \times 10^{-5}$ Torr, and a substrate temperature of 25 °C. All depositions were carried out at a working pressure of 3.01×10^{-3} Torr. The film thicknesses were confirmed using a KLA Tencor P16 Stylus Profiler. Film thicknesses in the order of 600 nm were deposited for samples in this study.

The SEM images of the as-deposited samples are shown in Figure 6.2, showing uniform thin films with good coverage of the substrate surface. As-deposited samples were also studied in comparison to the target. The EDX measurements of the samples compared to the target indicated that the target had a Sn/S ratio of 0.99, but the resulting films are slightly tin rich suggesting that sulphur was lost during the deposition process (Table in Figure 6.2).

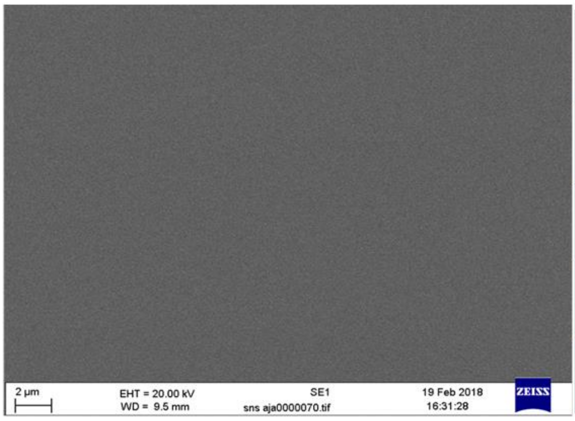

Element	Atomic % Sputtering target	Atomic % As-deposited thin films
S	50.23	49.10
Sn	49.77	50.9
[Sn/S]	0.99	1.03
Totals	100	100

Figure 6.2 Table shows EDX composition of the SnS target compared to the as-deposited thin films sputtered from the SnS target and SEM image of the as-deposited thin films.

Sputtering from a SnS target produces films of multiphase and poor electrical properties (high resistivity) which can be annealed to produce various tin sulphide phases depending on anneal temperatures and time

6.3 Systematic Studies of the Influence of Post-Annealing Treatment

The work reported in this study aims at establishing a suitable route to prepare single phase SnS thin films. Understanding the phase relationship as a function of temperature, pressure, and annealing time is important for developing the best process for sputtered SnS thin films. In order to optimize the processing of films using the RF sputtering system, three series of post annealing conditions were explored. The effects of annealing temperature, pressure and time were studied. Material properties such as structural, compositional and electrical properties were measured for every set of annealing conditions. A series of anneals were investigated at temperatures ranging from 300 °C to 450 °C under H_2S atmosphere, for a fixed time of two hours. The samples were SnS thin films deposited on n-type Si substrates. At relatively high temperature (> 450 °C) films were destroyed due to SnS evaporation. The annealing pressure was kept constant at 6 mbar. The annealing was done immediately after deposition in the same annealing system mentioned in Section 4.4. The furnace was heated to the pre-determined temperature, allowed to stabilise, and then flooded with a gas mixture of 6 % H_2S in Ar. The gas mixture flow was cut off after the annealing time and the quartz tube flushed with pure Ar gas. The temperature ramping rate was fixed 10 °C/min in all cases when ramping up and down. The H_2S concentration was constant for all runs. Finally, the furnace was allowed to cool to room temperature under steady vacuum, prior to the sample being removed. The phase purity of SnS was confirmed by XRD and Raman spectroscopy and the results are shown below.

6.3.1 Phase Investigation of Effects of Post-Deposition Annealing Treatment in Vacuum at Various Temperatures

The structure for each of the phases of the films annealed at different temperatures was determined by XRD analysis, as shown at Figure 6.3. The as-deposited films are amorphous, as were all films grown at room temperature. The peak at 33.5° corresponds to the overlap and cross bonding between (204) Sn_2S_3 and (111) peaks of SnS due to the low crystallinity. The formation of secondary phases at low deposition temperatures can be attributed to the high nucleation of formation energy for SnS compared to those for secondary phases (Sn_2S_3 and SnS_2). However, formation and growth of SnS becomes dominant with increasing deposition temperature because enough thermal energy can be provided [7].

As the annealing temperature increased to 350 °C, the films consist of mixed phases of orthorhombic SnS and Sn_2S_3 according to the standard diffraction peaks (JCPDS No. 14-0619 and JCPDS No. 39–0354). This peak is due to the evaporation of SnS and tin from the substrate surface. These phases are undesirable for materials used in solar cell applications. Discontinuity in the phase is likely to yield a larger number of recombination sites for generated carriers. Increasing the temperature to 400 °C, the amount of Sn_2S_3 present decreased and SnS became the dominant phase and the crystallinity of the films was also improved. The recrystallization of grains was increased resulting in an intense narrow peak that corresponds to the (111) plane of SnS. Well defined peaks at 2θ= 22.2°, 26.1°,27.5°, 31.5°, 30.5°, 39.1° match well the standard pattern of orthorhombic SnS. At a higher temperature of 450 °, a small additional peak appeared which comes from trace amounts of hexagonal SnS_2 phase (JCPDS No. 23–0677) in addition to SnS, which was due to the evaporation of SnS and tin from the substrate surface. A similar behaviour was also observed by Noguchi et al. in vacuum evaporated SnS films with varying substrate temperature [8].

These changes in the XRD patterns, lead to the conclusion that as the annealing temperature increases the formation of the SnS phase may be attributed to the conversation of the Sn_2S_3 phase according to the dissociation reaction, eq. 4.3 and eq. 4.4. The chemical process behind the decomposition is the reduction of Sn (IV) to Sn (II). In other words, this is analogous to the phase transformation of Sn_2S_3 to SnS.

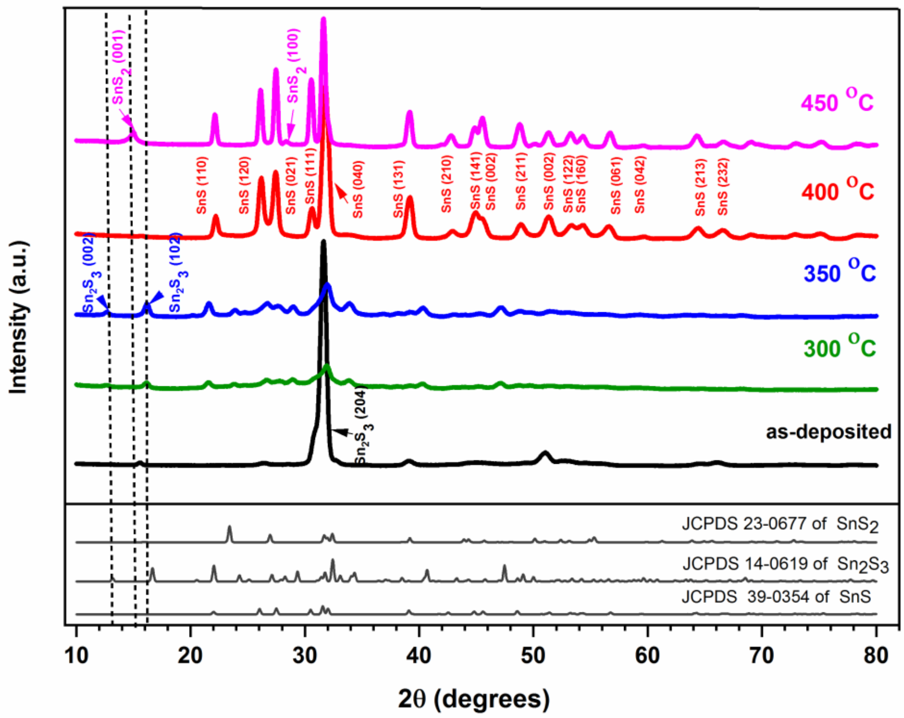

Figure 6.3 XRD spectra of the annealed samples at different temperatures at fixed pressure and annealing time.

XRD results implied that the crystallinity of the films could be improved by increasing the sulfurization temperature which is due to the acceleration of diffusion process of sulphur atoms into SnS layer. This indicates that higher sulfurization temperature accounts for the release of more sulphur atoms with sufficient thermal energy to diffuse into the film, hence more diffusion of sulphur into the film is possible. This results in an improvement of the crystallite size. Further, the secondary phases such as SnS_2 and Sn_2S_3 that had low formation energies dissociate with sulfurization temperature, leading to the growth of SnS [7].

To detect the impurity phases more precisely Raman analysis was performed. Raman measurement were performed to determine the phase purity of as deposited films and films annealed at different temperatures, Figure 6.4. The room temperature deposited film showed peaks at 130, 225 and 303 cm^{-1}. The Sn_2S_3 phase appears at the 303 cm^{-1}. The 130 and 225 cm^{-1} correspond to SnS phases with the desirable phase being at, 225 cm^{-1}. The shift of the peaks is attributed to the amorphous phase of the films. This indicates that SnS was not the main product of the films when formed in room temperature. This agrees with the XRD data of Figure 6.3, where the as deposited thin films showed a mixture of SnS and Sn_2S_3 phase. Steinmann et al. observed the same issue where the purchased SnS powder used for thermal evaporation was found to contain significant quantities of Sn_2S_3 (55% by weight) and SnS_2 (2%) in addition to the desired SnS phase (43%) [9].

The spectrum of the films annealed at 300 and 350 °C consists of mixed phases of Sn_2S_3 and SnS. Increasing the temperature to 400 °C, the Sn_2S_3 phase decreases substantially and promotes the formation of SnS as dominant phase as is evident by the three intense band peaks 162, 190 and 220 cm^{-1}. The characteristic peaks from the other secondary phases such as Sn_2S_3 cannot be observed, which indicate that a phase-pure SnS film was successfully obtained at an annealing temperature of 400 °C. The formation of this phase can occur through the reactions of eq. 4.4 and may be attributed to conversion of Sn_2S_3 phase into SnS. When increasing the temperature further, the reverse process of this reaction appears to occur, eq. 4.1, and although the Raman spectra suggests that the films are mostly SnS however there are apparent traces of SnS_2 appear, at a temperature of 450 °C. This is expected since, a continuous supply of sulphur is provided during the annealing procedure. This is in agreement with the observation made by XRD.

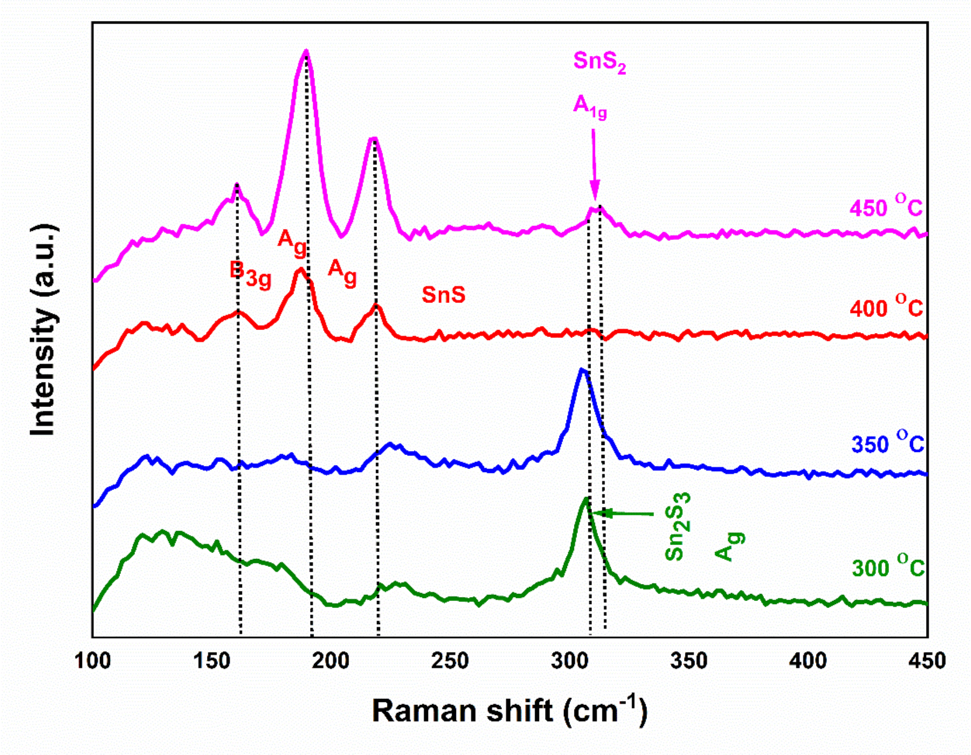

Figure 6.4 Raman spectra of the annealed samples at different temperatures at fixed pressure and annealing time.

The change in the microstructure due to the increase in the annealing temperature is also confirmed by the SEM observations. The SEM images of the samples are shown in Figure 6.5. It can be observed that annealing resulted in densification of the material and a significant increase in grain size, which are oriented perpendicular to the surface. This analysis revealed that the samples annealed at lower temperatures exhibited smaller grain structure. All annealed films were found to be pinhole free, and they consisted of densely packed columnar grains. The films annealed at 400 °C show larger grains, tightly bonded dense network with crystallites that are oriented uniformly and exhibit nearly equal size. For an absorber layer in traditional planar photovoltaic devices, it is generally desirable to have large textured grains and densely packed crystallites with well-passivated grain boundaries [8]. It has to be mentioned that when annealing at temperatures higher than 450 °C evaporation of the thin film from the substrate was observed in this study. From these analyses, it is concluded that the annealing process requires a temperature of 400 °C to produce a better morphology and highly crystalline SnS films.

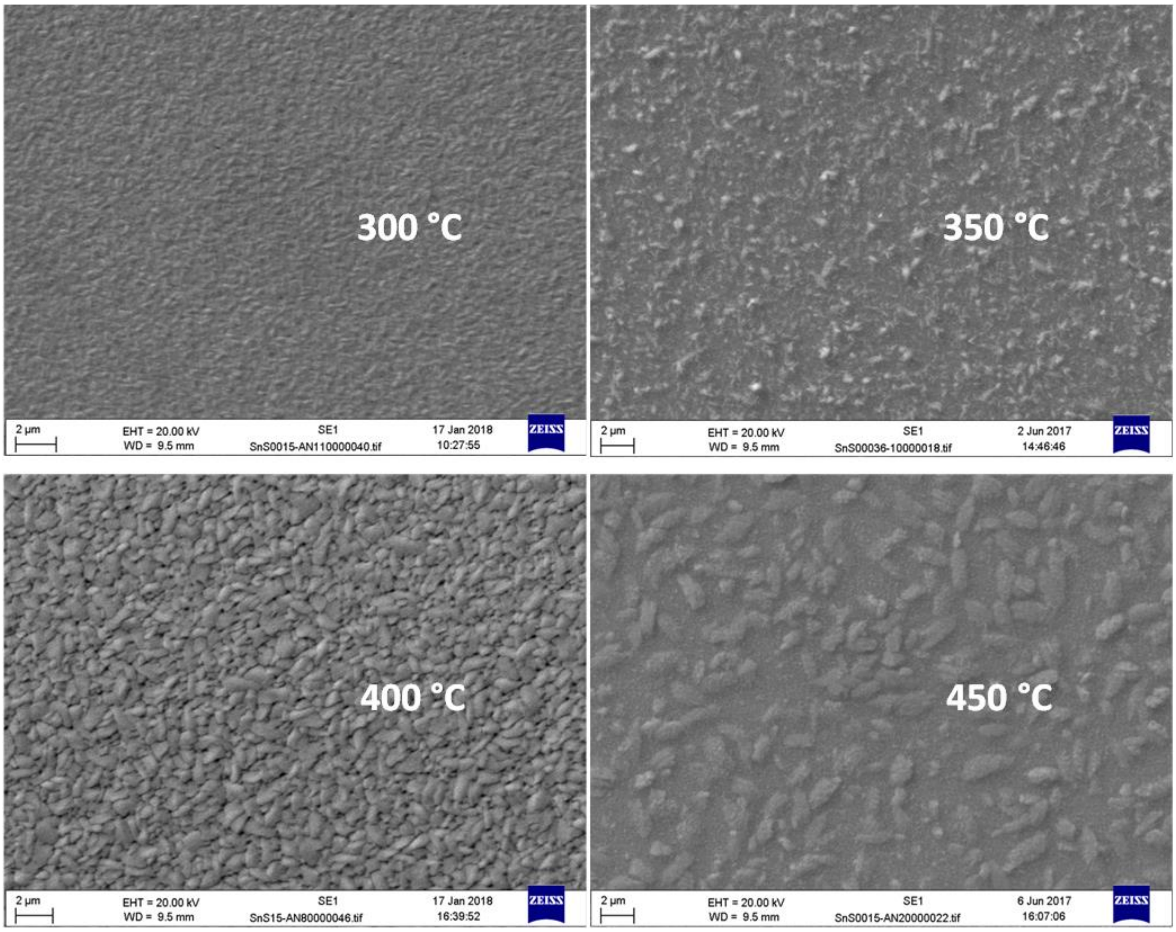

Figure 6.5 SEM images of the SnS films annealed at various temperatures, fixed pressure and annealing time.

6.3.2 Phase Investigation of Effects of Post-Deposition Annealing Treatment at Various Annealing Pressures

Interactions between residual gases and surface of the annealed films can be significantly reduced through low pressure (high vacuum). In this section the effect of annealing pressure on phase purification and film morphology is investigated. Figure 6.6 shows the XRD patterns of the films annealed at 400 °C under atmospheric pressure, 200 mbar, 100 mbar and 6 mbar for an annealing duration of 2 hours. The choices of pressure values was restricted due to the mass flow controllers and pump used in this study. The figure shows that the XRD peaks intensity increases as the pressure increases, which is attributed to the crystallization quality and grain growth. In all cases the annealing temperature and time was kept constant. At atmospheric pressure, the main peaks at 2θ = 22.2°, 26.1°,27.5°, 31.5°, 30.5°, 39.1° match with the standard pattern of orthorhombic structure of SnS (JCPDS 39–0354). Also traces of orthorhombic Sn_2S_3 phase (JCPDS no. 14-0619) at 2θ = 12.7°, 16°, 22.1°, 28.7°, 33.8°, 40.2° were detected. When the annealing pressure decreased, the Sn_2S_3 peaks decreased gently and the peaks of SnS become the dominant ones. Further decreasing the pressure to 6 mbar, the film is highly crystallized and consists of phase-pure SnS within the detection limit of XRD.

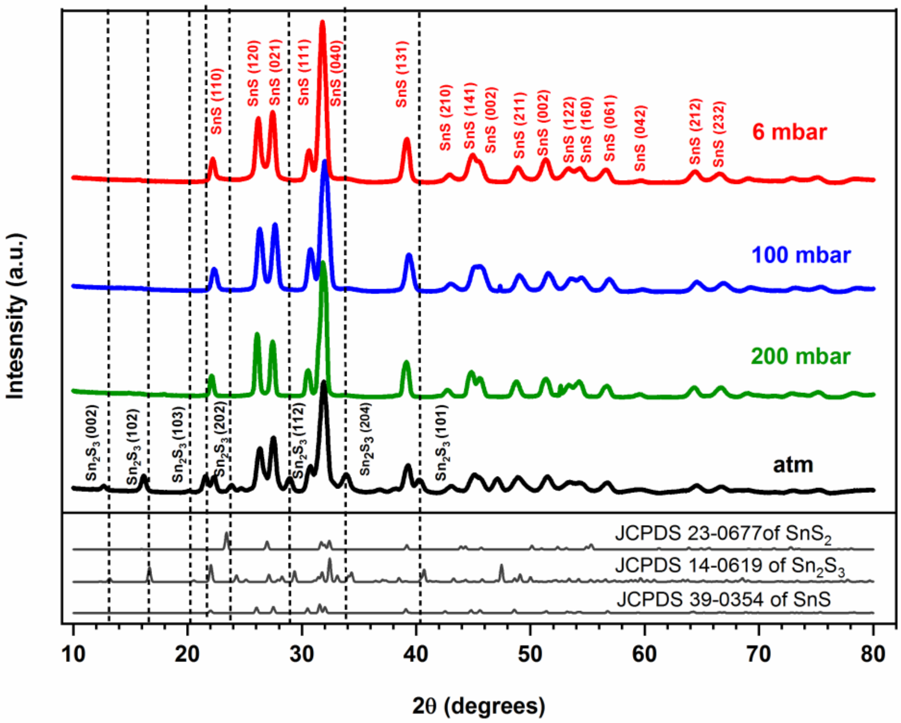

Figure 6.6 XRD spectra of the annealed samples at different temperatures at fixed temperature and annealing time, with a total pressure of 6 mbar.

Raman measurements were performed to further confirm the phases of films annealed at different pressures and the results are shown in Figure 6.7. The films annealed under atmospheric pressure are composed of Sn_2S_3, corresponding to the observed Raman peaks around 304 cm^{-1} and SnS phases corresponding to the observed Raman peaks around 160, 185 and 218 cm^{-1} [9]. As the pressure lowers the Sn_2S_3 peaks reduce and the component turns over to be SnS phase, which agrees well with the XRD analysis.

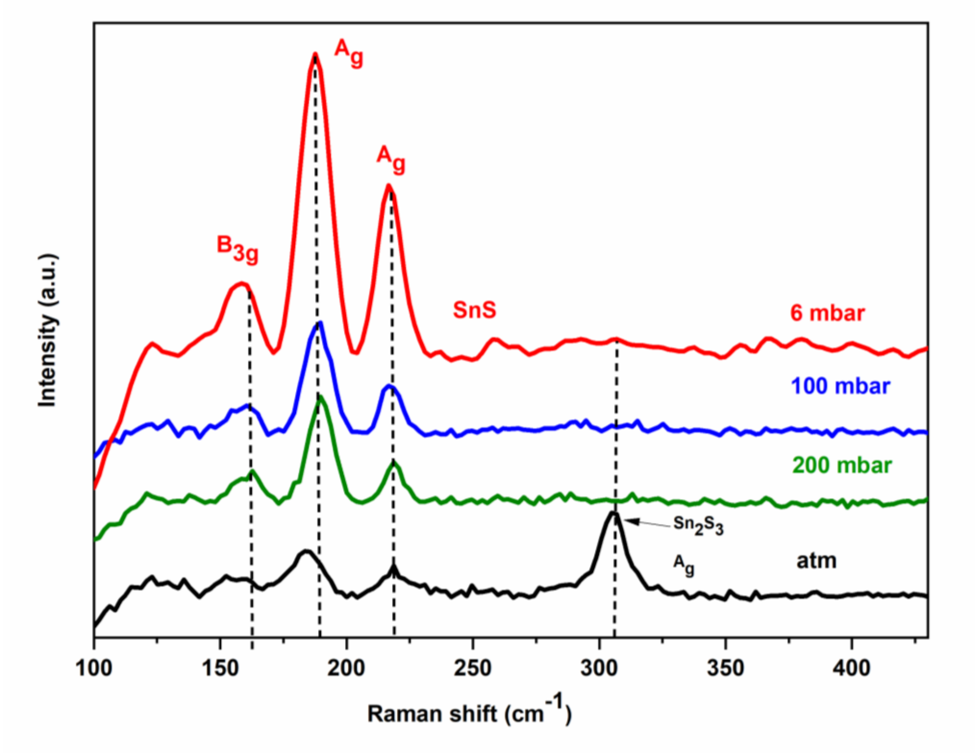

Figure 6.7 Raman spectra of the annealed samples under different pressures at fixed annealing temperature of 400 °C and annealing duration of 2 hours ,with a total pressure of 6 mbar.

The conversion of the deposited films to SnS during annealing under various pressures can be predicted by thermodynamics. Scragg et al. combined experimental investigations with a kinetic model to show the mechanism of the decomposition of SnS during annealing under sulphur (S_2) vapour. The choice of S_2 as the standard state for sulphur vapour is valid under most conditions when dealing with unsaturated sulphur atmospheres at sulphur pressures lower than around 100 mbar and temperatures above 300 °C. Figure 6.8 shows how the pressure of S_2 vapour affects the decomposition extent of SnS. The conditions required to stabilize Sn(IV) in the SnS system at a temperature of 550 °C is a minimum pressure of around 0.5 mbar. Below that pressure, Sn(IV) in Sn_2S_3 is unstable and will convert to Sn(II) in SnS. The authors mentioned that the values of equilibrium pressures given here should be treated as a rough guide to researchers in the field, as parameters can differ from each annealing system [10]. This provides key information for designing a successful annealing strategy for this study.

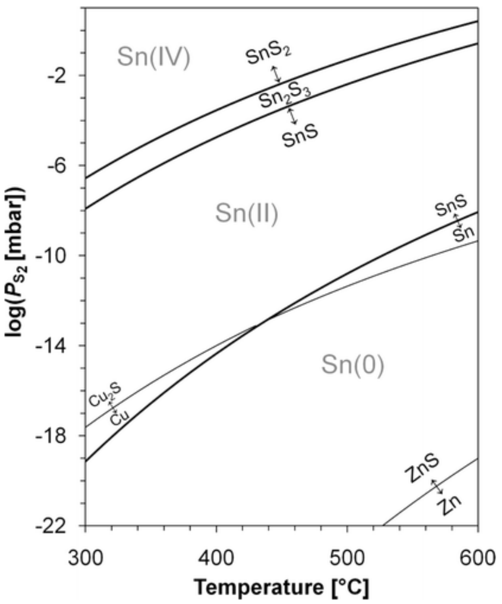

Figure 6.8 Plot of domains of stability of different sulphides of Sn as a function of temperature under S vapour [10].

6.3.3 Phase Investigation of Effects of Post-Deposition Annealing Treatment at Various Annealing Times

The effect of annealing duration was investigated for 2, 4, 6 and 8 hours. The other optimized annealing parameters such as the annealing temperature and pressure maintained as constant at 400 °C and 6 mbar, respectively.

It can be seen that the intensity of the XRD peaks increases with increased annealing duration, Figure 6.9. This observation reveals that annealing for a longer times improves the crystalline properties. As is seen, the films consist of crystalline orthorhombic SnS phase (JCPDS No. 39–0354) present at all annealing durations. The layers were mostly single phase with the crystal plane (111) and (040) giving rise to the most dominant peaks. With increasing annealing duration up to 4 hours the intensity of the (040) crystal plane of the film showed maximum intensity indicating better crystallinity. Unfortunately, such long annealing runs showed no material at the edges of the substrate, which was due to evaporation of the thin film from the substrate.

When annealed for 6 hours, the films showed a dominant orthorhombic SnS phase with some traces of hexagonal SnS_2, (100) crystal plane (JCPDS No. 23–0677). This might be due to accumulation of excess of sulphur when annealing for longer duration at 6mbar pressure. It was noticed that when annealing for more than 2 hours the edges of the films evaporated. Therefore, annealing for 2 hours was the optimum choice for this study. The (040) peak are most likely associated to the longer annealing time as shown and by other authors. At 6 hours, traces of SnS_2 phase is noticed, in addition to SnS, which is the dominant phase. This is likely due to the evaporation of SnS and tin from the substrate surface. This can be compared with Reddy et al. XRD results when annealing sputtered tin layers in a sulphur atmosphere [11]. They noticed that annealing at temperatures ≥ 450 °C the SnS_2 phase is also noticed, in addition to SnS, which was due to the evaporation of SnS and tin from the substrate surface as vapours.

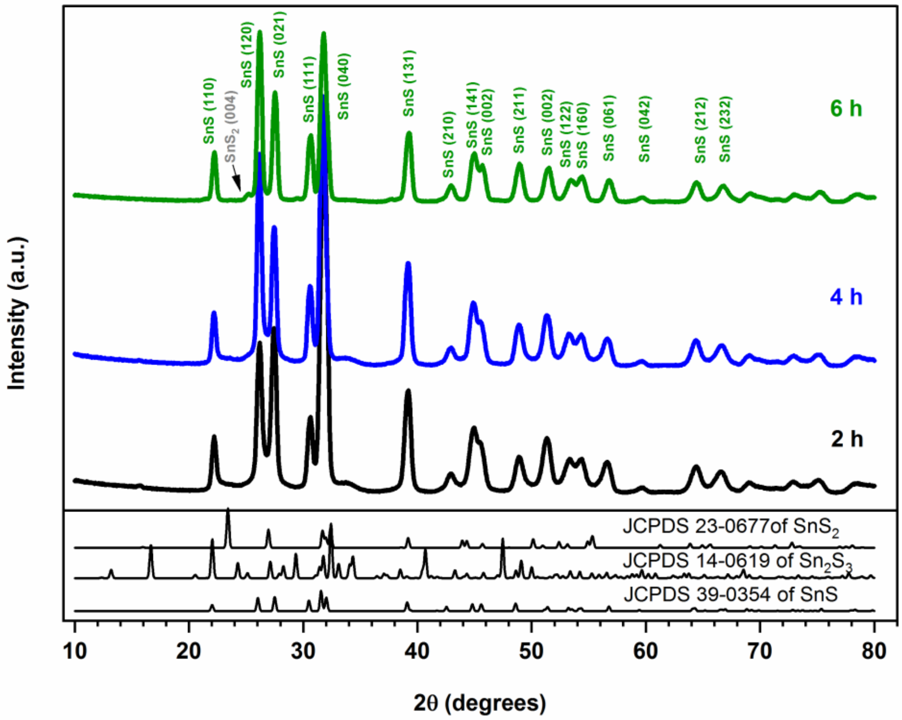

Figure 6.9 XRD spectra of the annealed samples at different annealing durations 2, 4, 6 hours, at fixed temperature 400 C, with a total pressure of 6 mbar.

To confirm phase purity Raman spectra measurements were applied to the annealed samples. Figure 6.10 shows that for all annealed samples at different durations, the films had SnS modes at 161, 187, 218 cm^{-1}, which are corresponding to the SnS phase [9]. When annealing for 6 hours a mode related to SnS_2 phase present at 312 cm^{-1} was noticed in addition to the SnS. The appearance of various phases in the films sulphurised at different temperature was in good agreement with the XRD.

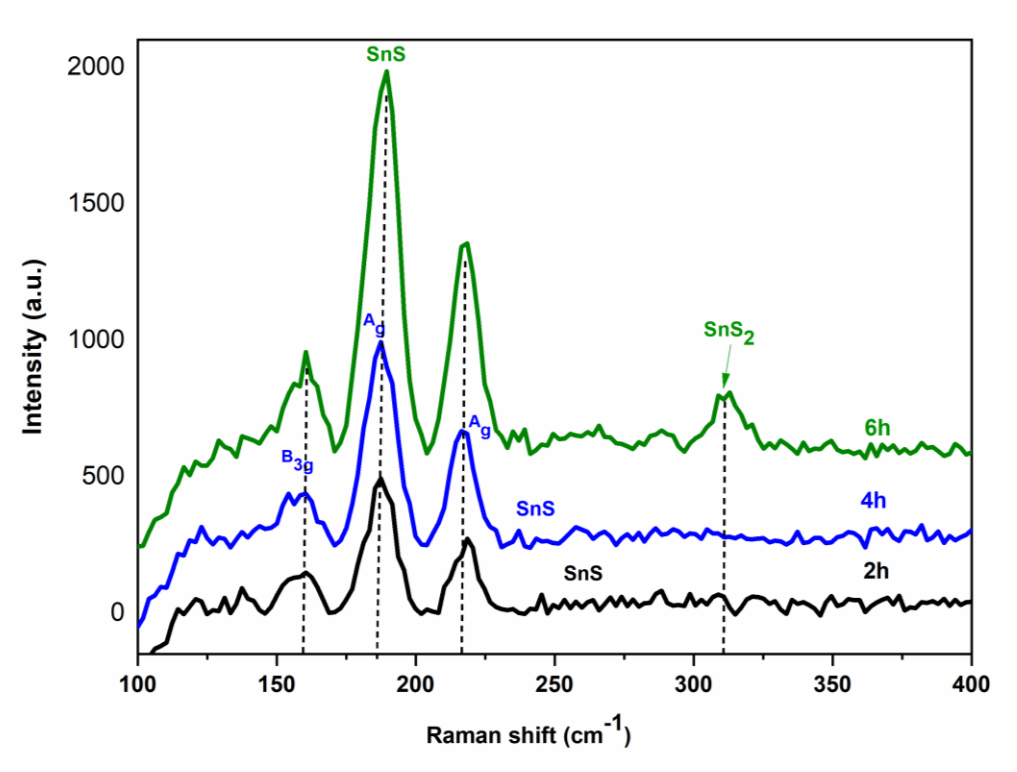

Figure 6.10 Raman spectra of annealed samples at different annealing durations 2, 4, 6 hours at fixed temperatures at a fixed annealing temperature of 400 °C , with a total pressure of 6 mbar.

6.4 Conclusions

In summary, the growth of SnS thin films via RF sputtering combined with the post-deposition annealing process under H_2S/Ar atmosphere has been successfully demonstrated. Depositing from a SnS (1:1) target at room temperature produced films that are amorphous, enabling crystallisation into SnS during annealing depending on the annealing conditions. Annealing temperatures varied from 300 to 450 °C at durations 2, 4, and 6 hours under various pressures from atmospheric pressure to 6 mbar. The annealing was performed under H_2S/Ar atmosphere. The results reveal that the films annealed at different temperature, pressures and annealing durations exhibit different structure and phase. The formation of different phases of SnS with the change of the annealing temperature may be interpreted as the result of different decomposition reactions. Analysis of XRD and Raman spectra's have elucidated the types of phases that form under various temperatures. The SnS phase was obtained by annealing at 400 °C. Lower or higher annealing temperatures resulted in mixed phases of SnS. In addition, XRD and Raman showed that annealing under low pressure is required in order to make the film surface completely stable against decomposition. The annealing pressure should be lower than 200 mbar.

The results of this work show that the phase pure SnS was obtained at the annealing temperature reach of 400 °C for 2 hours under pressure of 6mbar in H_2S atmosphere. The combined preparation route of RF sputtering and post-deposition annealing process opens up the novel possibility of mass and batch production of SnS films.

6.5 References

[1] R.E. Banai, J.C. Cordwell, G. Lindwall, N.J. Tanen, S.L. Shang, J.R. Nasr, Z-K. Liu, J.R.S. Browson, "Control of Phase in Tin Sulfide Thin Films Produced via RF Sputtering of SnS_2 Target with Post-deposition Annealing", vol. 45, pp 499–508, 2016.

[2] M.G.Sousaa, A.F.da Cunhaa, P.A.Fernandes, "Annealing of RF-magnetron sputtered SnS2 precursors as a new route for single phase SnS thin films", Journal of Alloys and Compounds, vol. 592, pp. 80-85, 2014.

[3] K. Hartman a,, J.L. Johnson b , M. I. Bertoni a , D. Recht c , M. J. Aziz c Michael A. Scarpulla b , T. Buonassisi, "SnS thin-films by RF sputtering at room temperature", vol. 519, pp. 7421–7424, 2011.

[4] J B Johnson, H Jones, B S Latham, JDParker, R D Engelken and C Barber, "Optimization of photoconductivity in vacuum-evaporated tin sulfide thin films", Semicond. Sci. Technol, vol. 14, pp 501–507.

[5] J.R. Nasr, J.J. Cordell, R.L. Gurunthan, J.R.S. Brownson and M.W. Horn, "Phase Control of RF Sputtered SnSx with Post-Deposition Annealing for a Pseudo-Homojunction Photovoltaic Device", Jornal of Electronic Materials, vol. 46, 2017.

[6] P. Sinsermsuksakul , L. Sun , S. Woon Lee , H. Hejin Park , S. Bok Kim , C. Yang , and R. G. Gordon, "Overcoming Efficiency Limitations of SnS-Based Solar Cells", Advanced Energy Materials, vol. 4 , 2014.

[7] L. A. Burton and A. Walsh, "Phase Stability of the Earth-Abundant Tin Sulfides SnS, SnS_2, and Sn_2S_3", The Journal of Physical Chemistry C, vol. 116, 2012.

[8] H. Noguchi, A. Setiyadi, H. Tanamura, T. Nagatomo and O. Omoto, "Characterization of vacuum-evaporated tin sulphide film for solar cell materials", Solar Energy Materials and Solar Cells, vol. 35, 1994.

[9] H. R. Chandrasekhar, R. G. Humphreys, and M. Cardona, "Infrared and Raman spectra of the IV-VI compounds SnS and SnSe", Physical Review B, vol. 15, pp.2177, 1977

[10] J. J. Scragg, T. Ericson, T Kubart, M. Edoff, and C. Platzer-BjCorkman, “Chemical Insights into the Instability of Cu2ZnSnS4 Films during Annealing”, Chemistry of Materials, vol. 23, 2011.

[11] V. Reddy Minnam Reddy, S. Gedi , C. Park b , M. R.W , R. Reddy K.T, “Development of sulphurized SnS thin film solar cells”, Current Applied Physics, vol. 15, 2015.

Chapter 7 Design, Fabrication and Characterization of p-SnS/ n-Si Heterojunction by RF sputtering

7.1 Introduction

As sputtering is a compatible process for large scale production of thin, it is an ideal process for the production of SnS thin film modules, such as thin film solar cells. In addition, sputtering has been successfully used for the deposition of $CuInS_2$ and Cu_2ZnSnS_4 films, with associated devices achieving energy conversion efficiencies of 11.4% and 7.9%, respectively [1-3].

Although, sputtering is proposed as a reliable industrial process to manufacture large area thin films very few studies have investigated RF sputtered SnS thin film solar cells. To date there are very few reports of SnS sputtering by a SnS (1:1) target in the literature. H.Lee fabricated a solar cell reported by using a 6 μm thick TiO_2 film to form a heterostructure. A 40-nm-thick Pt counter electrode was prepared by electron beam evaporation. To make a cell, 40-μm-thick parafilm was used as a spacer and a commercial liquid electrolyte (EL-HPE, Dyesol) was injected between the TiO_2/SnS electrode and the Pt counter electrode. This SnS electrochemical cell shows 0.025 mA/cm^2 of short circuit current, 350 mV of open circuit voltage, and a fill factor of 0.251. The resulting conversion efficiency is 0.0022 % [4].

In this chapter, I extend the results obtained in Chapter 6 to demonstrate the potential of sputtered SnS thin films to be used as absorber layers, as demonstrated by heterojunction structures. To investigate the photovoltaic properties of the films, single phase SnS thin films were grown on n-type silicon wafers to form heterojunction solar cells. The heterojunction device exhibited excellent photovoltaic performance confirming that the RF sputtered films procedure optimised is a route that can easily be scaled up for production.

This chapter describes the photovoltaic characteristics of a SnS/n-Si heterojunction solar cell. In addition, electrical properties of SnS thin films were investigated.

7.2 65Device Fabrication Process

The device characterisation and fabrication steps are discussed below. In essence, we demonstrate a similar fabrication process to Chapter 5 with the same device stack with a single deposition layer of SnS. A single layer was used since the sputtered SnS thin films showed denser compact films compared to the CVD ones, Figure 7.1.

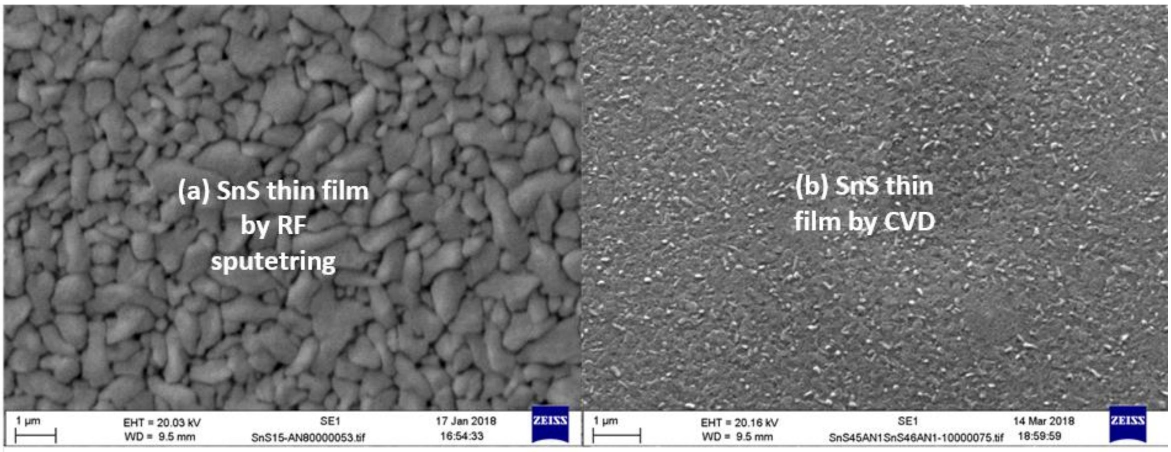

Figure 7.1 SEM images showing top surface of (a) RF sputtered SnS films and (b) SnS films by CVD.

Figure 7.2, shows a schematic cross-sectional view of the configuration of the heterojunctions devices fabricated in this chapter and a scanning electron microscopy (SEM) image of the SnS thin film surface. The optimised sputtered procedure discussed in Chapter 6 was applied to deposit SnS thin films.

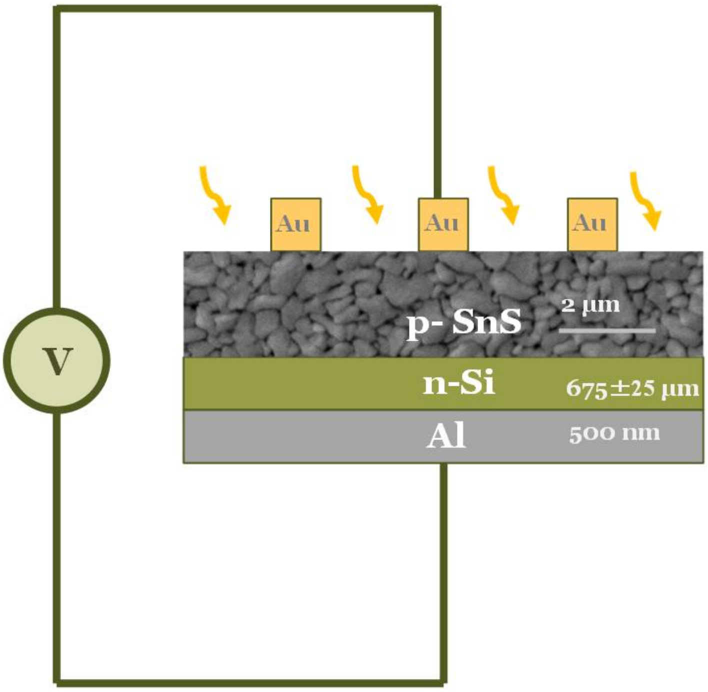

Figure 7.2 Schematic of the SnS/n-Si solar cell device structure.

7.2.1 Substrate Preparation

The substrates used were (100) oriented n-type Si dies (20×20 cm^2) with thickness of 675 ± 25 µm and a resistivity of 10-30 Ω cm. Before depositing the films the substrates were ultrasonically cleaned in sequence by acetone, isopropanol (IPA) and then finally rinsed with deionized water.

After sonication the substrates were dipped into a buffered HF solution (20:1) for 60 seconds to remove the native oxide layer from the substrates surface. After that, substrates were immediately loaded in the RF sputtering chamber for deposition.

7.2.2 Growth of SnS Absorber Layer

Optimisation of the conditions used for the deposition and annealing process indicated earlier in section 6.3, were applied to deposit the SnS films for the p–n heterojunction fabrication. The SnS film annealed at 400 °C for 2 hours under a pressure of 6 mbar was used to fabricate the thin film heterojunction solar cells.

To elucidate the phases, these samples were examined by XRD and Raman spectroscopy at room temperature. XRD spectra of the RF sputtered films deposited at room temperature and post annealed at 400 °C for 2 hours under pressure of 6mbar. Experimental XRD peaks are compared to SnS diffraction peak positions listed by JCPFS (039-0354). Figure 7.3 shows the XRD patterns of the films deposited on n-type Si substrates and annealed using the optimised process mentioned in Chapter 6. The observed peaks were compared with the standard JCPDS cards 39-0354 for SnS and indexed. XRD analysis shows all the peaks characteristic of the SnS phase having orthorhombic symmetry at $2\theta = 22.2°$, 26.1°,27.5°, 31.5°, 30.5°, 39.1° which confirms the formation of single phase of SnS with orthorhombic crystal structure. However, some small traces of Sn_2S_3 were detected at 26°, 37° which can be ignored since the intense (102) Sn_2S_3 peak at 17° did not appear which is the main characteristic of the Sn_2S_3 phase.

Raman scattering measurements was performed to further confirm the phases of sputtered films, Figure 7.4 The sputtered films show only three intense band peaks at 162, 190 and 220 cm^{-1} . These vibrations match with those reported for SnS in the literature, while, significantly, no additional vibrations indicative of the presence of SnS_2, Sn_2S_3 could be observed [5].

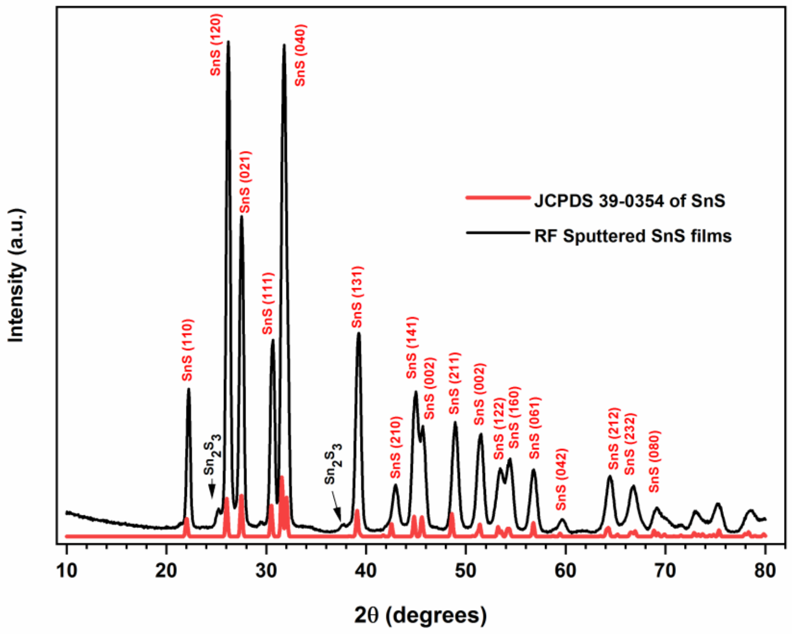

Figure 7.3 XRD spectra of the RF sputtered films deposited at room temperature and post annealed at 400 °C for 2 hours,with a total pressure of 6 mbar. Experimental XRD peaks are compared to SnS diffraction peak positions listed by JCPFS (039-0354).

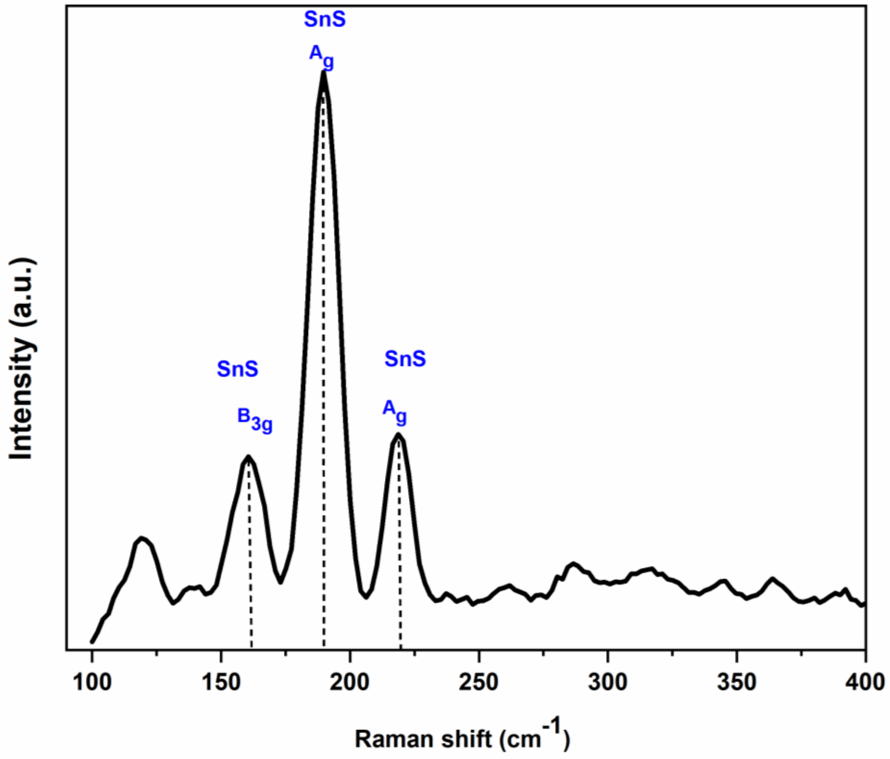

Figure 7.4 Raman spectra of the RF sputtered films deposited at room temperature and post annealed at 400 °C for 2 hours, with a total pressure of 6 mbar.

7.2.3 Front Contact Deposition

Gold contacts were deposited on the surface of SnS thin films, referred to as “front contacts.” All the front contacts described within this thesis were patterned by conventional optical lithography, metallization and lift-off using a dark field mask as discussed previously in Section 5.2.3.

I-V plots of Au/SnS measured at room temperature are shown in Figure 7.5. I-V exhibit linearity indicating an Ohmic contact between SnS and Au metal contact. The contact resistance is 1.07 $\times 10^6$ Ω., which is extracted from the I-V curve is in good agreement with the contact resistance evaluated in previous studies [7, 8].

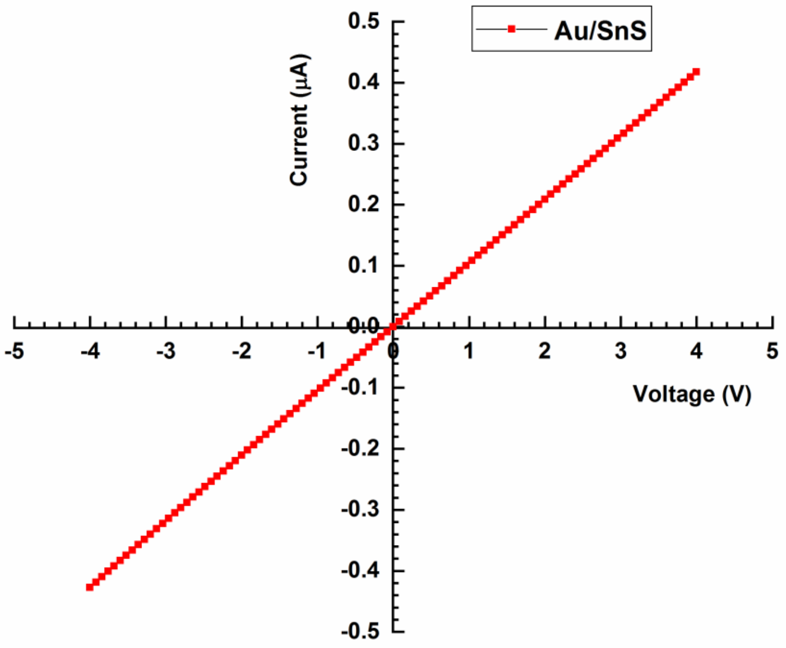

Figure 7.5 I-V characteristics of the Au contacts on RF sputtered SnS thin films.

7.2.4 Back Contact Deposition

An aluminium universal backside contact was deposited suing the same method discussed previously in section 5.2.4.

7.3 Device Characterisation

7.3.1 Current-Voltage (I-V) Measurements

To evaluate the electrical performance of the heterojunction, current-voltage curves (I-V) measurements at room temperature were carried out. The current-voltage curves were obtained using a Keysight B1500A semiconductor analyser incorporated with a HeNe 633 nm laser that was used to illuminate the heterojunctions. The electric measurements of the junction were conducted in a two-probe configuration. I-V curves of the heterojunction solar cell with and without illumination were obtained.

Dark I-V measurements are commonly used to analyse the electrical characteristics of heterojunctions, providing an effective way to determine fundamental performance of the junction. The current-voltage characteristics of the SnS/n-type Si heterojunction under dark is shown in Figure 7.6 proving the action of p-n junction. The dark forward and reverse I-V characteristics of the junctions indicated that the forward characteristics were exponential exhibiting diode like rectifying behaviour. The heterojunction shows low reverse saturation current and rectification properties.

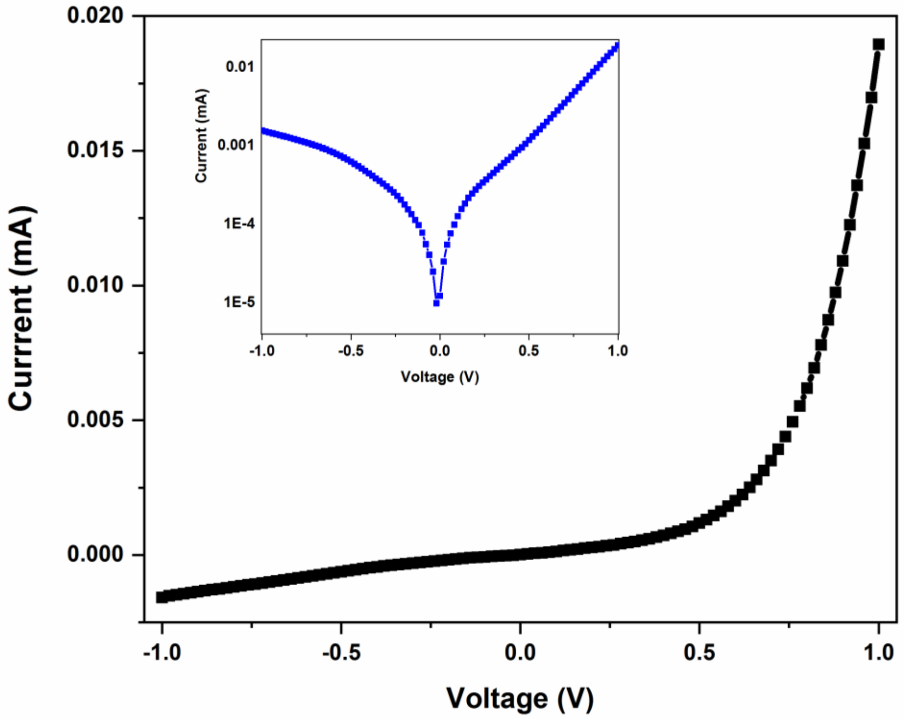

Figure 7.6 I-V curve of Au/SnS/n-type Si/Al heterojunction under dark conditions showing clear current rectification (the inset shows I-V plotted in semi-log scale).

From the dark characteristics of the graph diode the quality factor was evaluated. The ideality factor is indicative of the type of charge carrier recombination that is occurring inside of the diode. An ideality factor which is greater than unity implies the deviation from ideal diode. The fabricated heterojunction had an ideality factor of 2.8 and a value of reverse saturation current 2.01×10^{-07} A. It is generally believed that high ideality can be due to various reasons such as bulk material impurities, unusual recombination mechanisms taking place, interface trap states, and notably unfavourable heterojunction band alignment. Large ideality factor in p-n junctions, has been observed in perovskite-based oxide p-n junctions, where charge trapping at defects in the bulk seems important for transport properties [12].

Photovoltaic properties of the heterojunction are investigated by illuminating the device with a 633 nm laser, Figure 7.7. The photo-response current was found to be 0.04×10^{-6} A.

Photovoltaic properties of the heterojunction are investigated by illuminating the device with a 633 nm laser, Figure 7.7. The photo-response current was found to be 0.04×10^{-6} A. The spectral respond of the fabricated devices in this thesis was found to be 0.06 and the quantum efficiencies is 0.08%. These performance parameters are much less than those of the CVD SnS devices presented in section 5.3.1, This is the evidence that the SnS thin films absorb the light energy and transports generated carrier under applied bias. The device shows a strong response to light illumination.

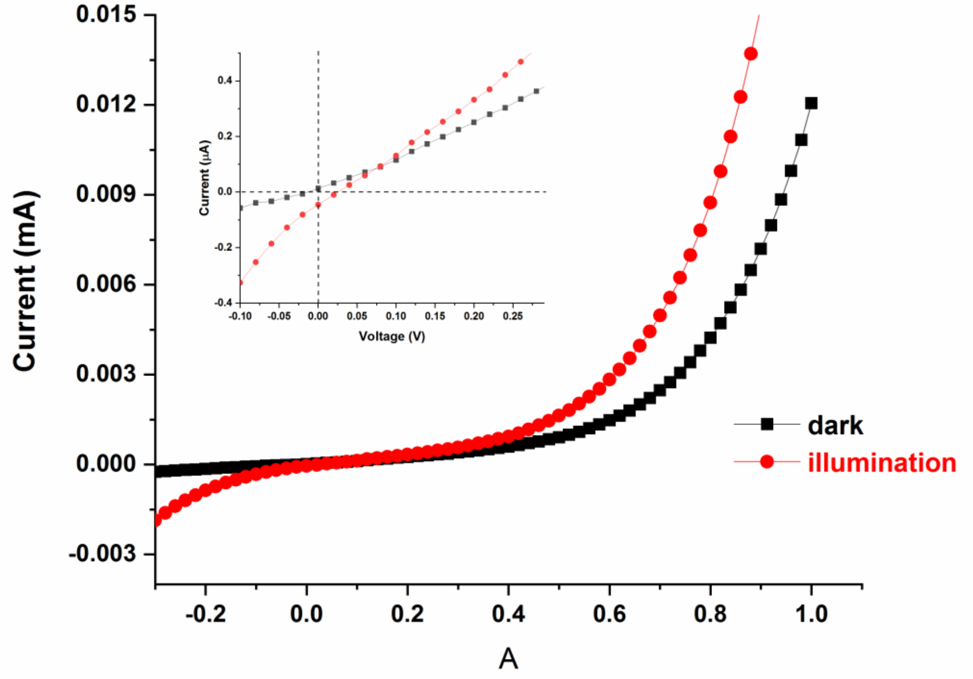

Figure 7.7 I-V characteristics of SnS/n-Si heterojunction solar cell under 633 nm laser.

7.3.2 Hall-Effect Mobility Measurements

Hall measurements are useful for extracting several electronic properties of a material and were applied in this thesis using a typical square Van der Paw structure at room temperature. Au contacts were deposited on post-annealed RF sputtered SnS thin films deposited on (100) n-type Si wafers. Contacts were spaced 5 to 10 mm apart. Contacts were checked prior to each Hall measurement by probing all combinations by sourcing current and measuring voltage. These measurements provided a baseline resistivity. The Hall coefficient R_H, +691 m^2/C, was positive showing a p-type of conductivity for the films. The films showed stable sheet resistance of $1.45\times10^{+06}$ Ω/sq and a carrier concentration of $+1.5\times10^{+16}$ $/cm^3$. The Hall mobility of about 4.74 $cm^2/$ Vs. Increase in mobility is due to the improvement in crystallinity and larger grain size, Appendix B3.

7.4 Conclusions

The orthorhombic SnS films were prepared by sulfurizing RF sputtered films. The composition of the prepared SnS film showed phase pure orthorhombic SnS, with a compact surface. In examining the electrical properties of SnS films, gold was found to make Ohmic contact to sputtered SnS films. Hall effect measurements confirmed the p-type conductivity of our films, with a mobility of 4.74 $cm^2/$ Vs and carrier concentration $+1.5\times10^{+16}$ $/cm^3$. The dark current-voltage characteristic of the p-SnS/n-type Si heterojunction was obtained. The fabricated heterojunctions shows typical rectification behaviour, the reverse saturation current has a value of around 2.01×10^{-07} A and a diode quality factor of 2.8. Under illumination of a 633 nm laser, photo-response was observed in SnS heterojunctions the open circuit voltage and short circuit current of this solar cell were 0.03 V and 0.04×10^{-6} A, respectively. The performance of the junction under illumination can be related to a number of issues, including unfavourable band offset between the deposited SnS thin film and the n-type Si wafer or grain boundaries acting as recombination centres. The heterojunction diode shows potential for photovoltaic application for photovoltaic applications and high-sensitivity silicon integrated photonic devices.

7.5 References

[1] F. Y. Liu, Y. Li, K. Zhang, B. Wang, C. Yan, Y. Q. Lai,. Z. A. Zhang, J. Li and Y. X. Liu, “Boost Voc of pure sulfide kesterite solar cell via a double CZTS layer stacks”, Solar Energy Materials and Solar Cells, vol. 94, pp. 2431–2434,2010.

[2] T. Unold, I. Sieber and K. Ellmer, “Efficient CuInS2 solar cells by reactive magnetron sputtering”, Applied Physics Letters, vol. 88, 2006.

[3] J. J. Scragg, T. Kubart, J. T. W¨atjen, T. Ericson, M. K. Linnarsson and C. Platzer-Bj¨orkman, “A detrimental reaction at the molybdenum back contact in Cu2ZnSn(S,Se)4 thin-film solar cells”, Journal of American Chemical Society, vol. 134, pp. 19330–19333, 2012.

[4] H. Lee, “Photoactive Nanostructured Materials and Devices: Pt Photo anodes, Cu Photcatalysts and SnS absorbers”, Ph.D. dissertation, The Pennsylvania State University, 2014.

[5] H. R. Chandrasekhar, R. G. Humphreys, and M. Cardona, “Infrared and Raman spectra of the IV-VI compounds SnS and SnSe”, Physical Review B, vol. 15, pp.2177, 1977.

[6] M. Devika, N. Koteeswara Reddy, F. Patolsky, and K. R. Gunasekhar, “Ohmic contacts to SnS films: Selection and estimation of thermal stability”, Journal of Applied Physics, vol. 104, 2008.

[7] C. Yang, L. Sun, R. E. Brandt, S. Bok Kim, X. Zhao, J. Feng, T. Buonassisi, and R. G. Gordon, “Measurement of contact resistivity at metal-tin sulfide (SnS) interfaces” , Journal of Applied Physics, vol. 122, 2017.

[8] R. L. Gurunathan, J.J. Cordell, R.A.Banai, M.Abraham, K.A.Cooley, M.Horn and S.E.Mohney, “Pd and Au Contacts to SnS: Thermodynamic Predictions and Annealing Study”, Journal of Electronic Materials, vol. 45, 2016.

[9] A. Mohr , P. Engelhart, C. Klenke, S. Wanka, A.A. Stekolnikov, M. Scherff, R. Seguin , S. Tardon, T. Rudolph, M. Hofmann, F. Stenzel, J.Lee , S. Diez, J. Wendt , W. Brendle, S. Schmidt , JW. Müller, P. Wawer, M. Hofmann, P. Saint-Cast, J. Nekarda , D.Erath, J. Rentsch , R. Preu. “20%-Efficient rear side passivated solar cells in pilot series designed for conventional module assembling”, Proc. 26th European Photovoltaic Solar Energy Conf., Hamburg, Germany; pp. 2150-2153, 2011.

[10] K.A. Münzer, J. Schöne, M.Hein, A. Teppe, R.E.Schlosser, M.Hanke, J.Maier, K.Varner, S.Keller, P. Fath , “Development and implementation of 19% rear passivation and local contact centaurus technology”, . Proc. 26th European Photovoltaic Solar Energy Conf., Hamburg, Germany; pp. 2292-2297, 2011.

[11] E. W. J. Mitchell and J. W. Mitchell, “The Work Functions of Copper, Silver and Aluminium”, Proceedings of the Royal Society of London. Series A, Mathematical and Physical Sciences, vol.210, pp. 70-84, 1951.

[12] Sze S M, 1981 Physics of Semiconductor Devices 2nd edn (New York: Wiley) Sharma B L and Purohit R K 1974 Semiconductor Heterojunctions (Oxford: Pergamon)

Chapter 8 Conclusions and Future Work

8.1 Conclusions

The potential suitability of SnS thin films synthesised by both CVD and RF sputtering methods, as a photovoltaic absorber material is presented in this study. This project has been unique in its direct comparison between the two fabrication techniques for the same material. More-ever, it was demonstrated that the composition, morphology and crystallinity of the SnS thin films are related to energy of the post deposition annealing step, therefore providing a method of tuning the film phase and electrical performance through a post annealing step.

In reality, very few studies have been performed for optimising room temperature deposited SnS thin film through a post-annealing treatment. Most studies present depositions at high temperatures leading to films with high roughness and poor electrical properties. The optimised post-annealing treatment in H_2S/Ar atmosphere presented in this work results in improvement in material quality and therefore better electrical properties.

The first three chapters review the different generations of solar cells through a literature review of SnS as an absorber material and the various methods used to deposit SnS films. The background theory relevant to understanding the principles of operation of solar cell devices was reviewed as well.

A simple novel two step method, consisting of the growth of smooth amorphous SnS thin films by CVD at room temperature followed by an H_2S annealing at controlled temperatures was presented in Chapter 4. Before synthesis, thermodynamic calculations of the reactions from precursors was applied. The thermodynamic calculations showed that, the reaction of $SnCl_4$ and H_2S is spontaneous at room temperature. Through the calculations it can be predicted that the formation of SnS from the direct reaction of $SnCl_4$ and H_2S by adjusting the deposition conditions of the $SnCl_4/H_2S$ CVD process is possible. In this work I additionally optimised for uniform, pinhole free thin films. The impact of $H_2S/SnCl_4$ concentration ratio on the formation of thin films was also studied. A higher $H_2S/SnCl_4$ concentration ratio was found to increase the formation of good quality SnS thin films. A second step was required to adjust the Sn/S stoichiometry and for the removal of the unreacted chlorine. Moreover, the annealing step was required to promote grain growth and reduce grain boundaries which is a procedure frequently used to improve absorber layer material properties. The results emphasized that annealing the films in H_2S atmosphere at 400 °C changes the stoichiometry of the as-deposited SnS films and leads to the formation of single phase SnS films.

Results in Chapter 5 showed that by using a two layer deposition by CVD it was possible to produce thin films of phase-pure SnS that are suitable for use in thin film solar cell structures. The SnS thin films deposited by the bilayer protocol are pure single phase. X-ray diffraction (XRD) analysis and micro-Raman studies confirm the formation of single phase SnS films. Hall effect measurements confirm the p-type nature of the SnS thin films with a mobility of 1.7 cm^2/Vs. Using the double deposition method, SnS/n-type Si heterojunction have been fabricated. From the current-voltage measurements, the heterojunction exhibited diode like behaviour in dark. The diode shows typical rectification behaviour, the saturation current has a value of 3.36×10^{-05} A and the estimated diode factor of this junction was 2.24. Under illumination, the photo response behaviour of the device was explored and the device was highly sensitive to 633 nm laser. The heterojunction exhibited photovoltaic performance The V_{OC} and J_{SC} are 0.12V and 3.3×10^{-7} A respectively. The present scheme to prepare high-quality SnS films might be useful for fabricating photovoltaic, photodetectors and optoelectronic heterostructures.

The growth of SnS thin films via RF sputtering combined with the post-deposition annealing process under H_2S/Ar atmosphere has been successfully demonstrated in Chapter 6. Depositing from a SnS (1:1) target at room temperature produced films that are amorphous, enabling crystallisation into SnS during annealing depending on the annealing conditions. Annealing temperatures varied from 300 to 450 °C for 2, 4, and 6 hours under various pressures from atmospheric pressure to 6 mbar. The annealing was performed under H_2S/Ar atmosphere. The results reveal that the films annealed at different temperature, pressures and annealing durations exhibit different structure and phase. The formation of different phases of SnS with the change of the annealing temperature may be interpreted as the result of different decomposition reactions. Analysis of XRD and Raman spectra's have elucidated the types of phases that form under various temperatures. The SnS phase was obtained by annealing at 400 °C. Lower or higher annealing temperatures resulted in mixed phases of SnS. In addition, XRD and Raman showed that annealing under high pressure is required in order to make the film surface completely stable against decomposition. The results of this work show that the phase pure SnS have been obtained when the annealing temperature reach 400 °C for 2 hours under pressure of 6mbar under H_2S atmosphere. The combined preparation route of RF sputtering and post-deposition annealing process opens up the novel possibility of mass and batch production of SnS films. The orthorhombic SnS films were prepared by post annealing RF sputtered films under H_2S/Ar atmosphere. The composition of the prepared SnS film showed phase pure orthorhombic SnS, and the surface of prepared SnS film is compact. In examining the electrical properties of SnS films, gold was found to make Ohmic contact to sputtered SnS films. Hall effect measurements confirmed the p-type conductivity of our films, with a mobility of 4.74 cm^2/ Vs and carrier concentration of $+1.5\times10^{+16}$ $/cm^3$ The dark current-voltage characteristic of the SnS/n-type

Si heterojunction was obtained. The SnS/n-Si junction shows typical rectification behaviour, and the reverse saturation current has a value of around 2.01×10^{-07} A and a diode quality factor of 2.8. Under illumination of a 633 nm laser, photo-response was observed in SnS heterojunctions the open circuit voltage and short circuit current of this solar cell were 0.03 V and 0.04×10^{-6} A, respectively. The heterojunction diode shows potential application for photovoltaic applications. Table 8.1 shows the structures of devices and performance parameters. High Jsc has been achieved in SnS solar cells, but V_{oc} and FF remain significantly lower than other thin film devices.

Table 8.1 Performance of SnS-based devices by performance

SnS deposition Method	Device Structure	η (%)	V_{oc} (mV)	J_{SC} (mA/cm^2)	FF (%)	Mobility (cm^{2}V^{-1}s^{-1})	Refs
ALD	Si/SiO$_2$/Mo/SnS/ ZnO$_{0.74}$S$_{0.26}$/ZnO/ITO/Ag	4.36	372	20.2	58.0	16.4	[1]
ALD	Glass/Mo/SnS/SnO$_2$/ Zn(O,S):N/ZnO/ITO/Al/Ni	2.9	261	24.9	44.4	4	[2]
Pulsed CVD	Glass/Mo/SnS/ Zn(O,S)/ZnO/ITO	2.0	244	19.42	42.97	-	[3]
RF sputtering	ITO/p-SnS/n-Si/Al	-	300	0.005	-	15	[4]

Contribution of this thesis to the field of SnS thin film technology can be summarised into:

- A new low-cost methodology for the synthesis of single-phase orthorhombic, p-type SnS thin films was introduced. The synthesis was achieved by CVD using $SnCl_4$ and H_2S at room temperature followed by an optimised post-annealing treatment. A detailed analysis of the properties of SnS films were investigated as a function of precursor concentration and post-annealing temperature.

- Heterojunction structures were successfully fabricated using the CVD. SnS layers grown on n-type silicon wafers. Current-voltage measurements show a diode like behaviour of the heterojunction. Under illumination the devices show photovoltaic performance confirming that the synthesis achieved is an effective route to achieve enhanced photovoltaic devices.
- Formation of high quality phase pure orthorhombic SnS films was successfully achieved consisting on the annealing of RF-magnetron sputtered thin films from a SnS (1:1) target. A systematic and detailed study of the effects of the annealing conditions on the phase content of the tin sulphide films was clearly presented. A systematic study was carried out to understand the influence of post annealing variables, which include annealing time, temperature, and pressure. Fine tuning of all annealing variables was carried out. An optimised post annealing recipe was established to produce high quality SnS thin films which enables for large scale production of SnS films at low cost.
- Heterojunction diodes of the sputtered SnS thin films were fabricated with the diode structure Au/SnS/n-type Si/Al. The junction exhibits a rectifying diode behaviour. Under illumination the photovoltaic effect was observed.

8.2 Future Work

Future work that were based on the findings of this thesis includes:

- The improvement in the photovoltaic performance can be done by exploring different buffer layers with SnS as an absorber. A study of investigating the proper candidate of n-type semiconductor materials is also important. The highest efficiency of an SnS device has been achieved using Zn(O,S) buffer layer with optimized Zn:O ratio, using similar SnS films to the ones synthesised in this thesis which indicates highest efficiencies can be achieved.
- Several experiments can be proposed to extend the research of SnS thin films. These experiments will further extend the knowledge of its material properties. XPS and infrared spectroscopic ellipsometry (IRSE) can be used to study the material at an atomic level. The measurements can be used to study bonding in the material, and more confidently extract phase information for films of mixed phase
- Fabricated devices with other suitable contact metals will affect the overall efficiency of the diode which is important for improving thin films solar cell devices. Therefore exploring various metal /semiconductor electrical behaviour can be performed for both CVD and RF

sputtered SnS thin films. This study should help to improve the performance of SnS solar cells further.

- The annealing experiments done in this thesis did a good job detailing the phase and electrical measurements of the film. Further studies on the carrier lifetimes by controlling vacancies and intrinsic defects could lead to further optimisations.
- Doping is another area that could be explored. Several other studies have been done showing improved electronic properties with silver and/or copper doping.

8.3 References

[1] P. Sinsermsuksakul, L. Sun, S. W. Lee, H. H. Park, S. B. Kim, C. Yang and R. G. Gordon, “Overcoming efficiency limitations of SnS-based solar cells”, Advanced Energy Materials, vol.4, pp. 1400496, 2014.

[2] H.H. Park, R. Heasley, L. Sun, V. Steinmann, R. Jaramillo, K. Hartman, R. Chakroborty, P. Sinsermsuksakul, D. Chua, T. Buonassisi, R. G. Gordon, “Co-optimization of SnS absorber and Zn(O,S) buffer materials for improved solar cells”, Progress in Photovoltaics: Research and Applications, 2015.

[4] P. Sinsermsuksakul, K. Hartman, S.B. Kim, J. Heo, L. Sun, H.H. Park, R. Chakraborty, T. Buonassisi, R.G. Gordon, “Enhancing the efficiency of SnS solar cells via band-offset engineering with a zinc oxysulfide buffer layer”, Applied Physical Letters, vol. 053901, 2013.

[4] M. Patel, H.-Sik Kim and J. Kim, “Wafer-scale production of vertical SnS multilayers for high-performing photoelectric devices”, Nanoscale, vol.9, pp. 15804–15812, 2017.

Appendix A1: Thermodynamics Data for Calculating the Gibbs free energy, Entropy and product concentration

$$SnCl_4(l) + 2H_2S(g) \rightarrow SnS(s) + 4HCl(g) + \frac{1}{2}S_2(g)$$

T(C)	Delta (H) J	Delta (G) J	Delta Vol (litre)	Delta S (J/K)	Delta Cp (J/K)	K eq
	SnCl4(l)	H2S(g)	SnS(s1)	HCl(g)	S(s1)	
20	75316.8	20518.9 4	4.8111E+01	86.928	-4.39E+01	2.21E-04
50	73889.7	14979.9 5	5.3034E+01	82.299	-5.12E+01	3.79E-03
100	71433.4	6062.6	6.1240E+01	75.186	-6.26E+01	1.42E-01
	SnCl4(g)	H2S(g)	SnS(s1)	HCl(g)	S(l)	
150	40260.1	770.1	3.47E+01	93.324	3.15E+01	8.03E-01
200	41860.4	-3988.1	3.88E+01	96.901	3.08E+01	2.76E+00
250	43333.4	-8909.4	4.29E+01	99.862	2.82E+01	7.55E+03
300	44688.2	-13966.2	4.70E+01	102.337	2.60E+01	1.87E+01
350	45946	-19136.9	5.11E+01	104.442	2.46E+01	4.02E+01
400	47164.1	-24406.8	5.52E+01	106.322	2.41E+01	7.83E+01
450	48361.3	-29766.4	5.93E+01	108.038	2.38E+01	1.41E+02
500	49545.9	-35208.4	6.34E+01	109.622	2.36E+01	2.39E+02

$$SnCl_4(l) + 2H_2S(g) \rightarrow SnS_2(s) + 4HCl(g)$$

T(C)	Delta (H) J	Delta (G) J	Delta Vol (litre)	Delta S (J/K)	Delta Cp (J/K)	K eq
	$SnCl_4$(l)	H_2S(g)	SnS_2(s)	HCl(g)		
20	29720.1	-18755.8	4.81E+01	165.362	-4.58E+01	2.20E+03
25	29488.2	-19580.6	4.89E+01	164.578	-4.70E+01	2.69E+03
50	28235	-23645.1	5.30E+01	160.545	-5.33E+01	6.64E+03

Appendix A1 Thermodynamics Data for Calculating the Gibbs free energy, Entropy and product concentration

100	25251.1	-31460.8	6.12E+01	151.981	-6.61E+01	2.53E+04
	$SnCl_4$(g)	H_2S(g)	SnS_2(s)	HCl(g)		
150	-8166.9	-35414.3	3.47E+01	64.392	1.42E+01	2.35E+04
200	-7492.4	-38673	3.88E+01	65.9	1.28E+01	1.86E+04
250	-6880	-41999.7	4.29E+01	67.131	1.17E+01	1.56E+04
300	-6314.9	-45382.8	4.70E+01	68.163	1.09E+01	1.37E+04
350	-5784.9	-48813.7	5.11E+01	69.05	1.03E+01	1.23E+04

Appendix A2: Thermodynamics Data for Calculating the Concentration of Reaction Products at Various Deposition Temperatures

Temperature °C	Reactants	Phase	Concentration (mole)	Reaction Product	Phase	Concentration (mole)
15						
20	$SnCl_4$+$2H_2S$	gas	3.9735	H_2S	gas	1.3363E-02
				HCl	gas	0.97995
				$SnCl_4$	gas	6.6817E-03
				H_2	gas	4.9685E-08
				H_2S_2	gas	4.9645E-08
				SnS_2	solid	0.97345
25	$SnCl_4$+$2H_2S$	gas	3.9728	HCl	gas	0.97949
				H2S	gas	1.3674E-02
				SnCl4	gas	6.8372E-03
				H2	gas	6.1795E-08
				H2S2	gas	6.1741E-08
				SnS2	solid	0.97284
50	$SnCl_4$+$2H_2S$	gas	3.9700	HCl	gas	0.97730
				H2S	gas	1.5132E-02
				SnCl4	gas	7.5662E-03
				H2	gas	1.6617E-07
				H2S2	gas	1.6593E-07
				SnS_2	solid	0.96996
100	$SnCl_4$+$2H_2S$	gas	3.9651	HCl	gas	0.97361
				H2S	gas	1.7591E-02
				SnCl4	gas	8.7963E-03

Appendix A2 Thermodynamics Data for Calculating the Concentration of Reaction Products at Various Deposition Temperatures

				H2	gas	8.0838E-07
				H2S2	gas	8.0481E-07
				SnS_2	solid	0.96512
150	$SnCl_4+2H_2S$	gas	3.9613	HCl	gas	0.97070
				H2S	gas	1.9529E-02
				SnCl4	gas	9.7673E-03
				H2	gas	2.7206E-06
				H2S2	gas	2.6842E-06
				SnS2	solid	0.96131
200	$SnCl_4+2H_2S$	gas	3.9583	HCl	gas	0.96840
				H2S	gas	2.1054E-02
				SnCl4	gas	1.0534E-02
				H2	gas	7.1637E-06
				H2S2	gas	6.9004E-06
				SnCl2	gas	4.2347E-07
				S2	gas	2.4647E-07
				SnS2	solid	0.95830
450	$SnCl_4+2H_2S$	gas	3.9892	HCl	gas	0.94402
				H2S	gas	2.9073E-02
				SnCl2	gas	1.2042E-02
				SnCl4	gas	8.6528E-03
				S2	gas	5.7930E-03
				H2	gas	1.4251E-04
				H2S2	gas	1.3228E-04
				S3	gas	1.1583E-04
				S4	gas	1.1166E-05
				S6	gas	6.5296E-06
				S5	gas	5.4969E-06
				S7	gas	8.3551E-07

Appendix A2 Thermodynamics Data for Calculating the Concentration of Reaction Products at Various Deposition Temperatures

				S8	gas	1.6777E-07
				S2C1	gas	1.4168E-07
				SnS	gas	3.1946E-08
				S2Cl	gas	2.4408E-08
				SnS2	solid	0.91744
500	$SnCl_4+2H_2S$	gas	4.0481	HCl	gas	0.90717
				H2S	gas	3.9945E-02
				SnCl2	gas	3.2268E-02
				S2	gas	1.5641E-02
				SnCl4	gas	4.1051E-03
				H2	gas	3.0998E-04
				S3	gas	2.9638E-04
				H2S2	gas	2.24E-04
				S4	gas	2.53E-05
				S5	gas	7.15E-06
				S6	gas	6.65E-06
				S7	gas	8.17E-07
				SnS	gas	6.15E-07
				S2Cl	gas	4.02E-07
				HS	gas	1.32E-07
				S8	gas	1.21E-07
				SnCl	gas	2.14E-09
				SCl2	gas	1.82E-09
				SnS2	solid	0.85276

Appendix A2 Thermodynamics Data for Calculating the Concentration of Reaction Products at Various Deposition Temperatures

Appendix A3 Single crystal XRD data (Inorganic Crystal Structure Database (ICSD)

	SnS	SnS_2	Sn_2S_3
angle θ=1.5°			
Crystal system	orthorhombic	Trigonal	orthorhombic
Space Group	P n m a (62)	R-3	P n m a (62)
a,b,c (Å)	11.180(6) 3.982(2) 4.329(3)	3.6349(2), 3.6349(2), 52.856(4)	8.878(2) 3.751(1) 14.020(3
γ	90. 90. 90	120.120,120	90. 90. 90
Volume	192.72	604.80	463.27
PDF No.	015939-354	010523-677	01-075-2183 14-619

Appendix A4 Hall Measurements for SnS films by CVD

Hall measurements for SnS thin films (deposition 1)

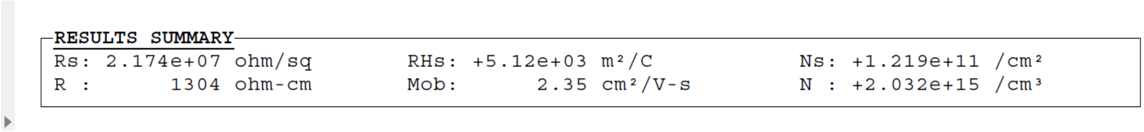

```
RESULTS SUMMARY
Rs: 2.174e+07 ohm/sq        RHs: +5.12e+03 m²/C           Ns: +1.219e+11 /cm²
R :      1304 ohm-cm        Mob:       2.35 cm²/V-s       N : +2.032e+15 /cm³
```

Hall measurements for SnS thin films (deposition 2)

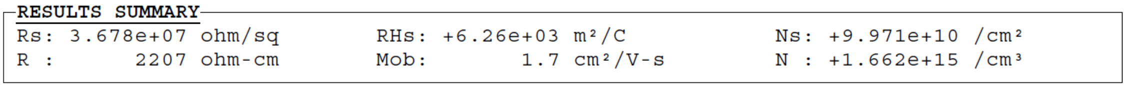

```
RESULTS SUMMARY
Rs: 3.678e+07 ohm/sq        RHs: +6.26e+03 m²/C           Ns: +9.971e+10 /cm²
R :      2207 ohm-cm        Mob:        1.7 cm²/V-s       N : +1.662e+15 /cm³
```

Appendix A4 Hall Measurements for SnS films by CVD

Appendix B1 Sputtering Deposition Conditions

Fabrication of SnS thin films by RF sputtering

Batch ID: SnS00014

Date: 25/04/17

Target: SnS (50:50) **Supplier**: Schotech

RF sputtering conditions:

Power (W)	Ar flow (sccm)
Plasma strike=35	70
Deposition power =50	20
Fwd power (W)	49
DC bias (W)	255
Base Pressure	4X10-5
Deposition pressure	3.01X10-3
Deposition rate (nm/s)	5.2 nm/min
Deposition time	2:30
Deposition temperature	RT
Ramping rate (c/min)	-
Thickness of layer	780 nm
Substrates	8 288nm SiO2 patterned substrates /Si, SL
Notes	Gun 1

Appendix B1 Sputtering Deposition Conditions

Appendix B2 EDX of SnS target

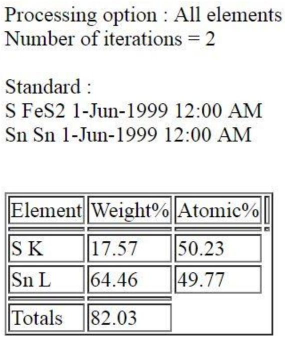

Processing option : All elements analyzed
Number of iterations = 2

Standard :
S FeS2 1-Jun-1999 12:00 AM
Sn Sn 1-Jun-1999 12:00 AM

Element	Weight%	Atomic%
S K	17.57	50.23
Sn L	64.46	49.77
Totals	82.03	

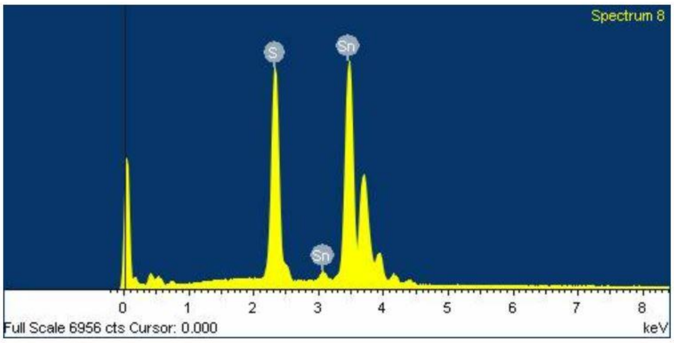

Appendix B3 Electrical Characterisation of RF Sputtered SnS/n-Si heterojunctions

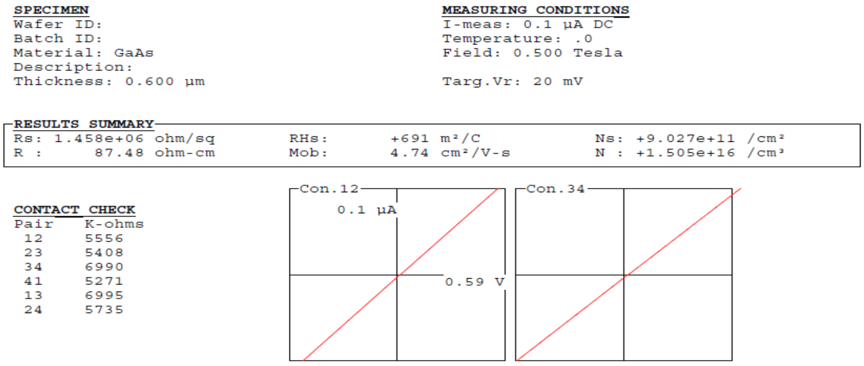

```
SPECIMEN                                    MEASURING CONDITIONS
Wafer ID:                                   I-meas: 0.1 µA DC
Batch ID:                                   Temperature: .0
Material: GaAs                              Field: 0.500 Tesla
Description:
Thickness: 0.600 µm                         Targ.Vr: 20 mV

RESULTS SUMMARY
Rs: 1.458e+06 ohm/sq       RHs:      +691 m²/C         Ns: +9.027e+11 /cm²
R :     87.48 ohm-cm       Mob:      4.74 cm²/V-s      N : +1.505e+16 /cm³

CONTACT CHECK
Pair    K-ohms
 12     5556
 23     5408
 34     6990
 41     5271
 13     6995
 24     5735
```

Table B3.1. The effects of annealing in the different environments on the electrical properties of the films are summarised

Sample ID	Annealing Temperature (°C)	Phase by Raman	Conductivity ($\Omega^{-1}cm^{-1}$)	Mobility ($cm^2\ V^{-1}\ s^{-1}$)	Carrier concentration (cm^{-3})	Type
AN 0	0	Sn_2S_3	Out of range	unknown	unknown	unknown
AN 7	300	Sn_2S_3 + traces of SnS	Out of range	unknown	unknown	unknown
AN 6	350	SnS+ traces of Sn_2S_3	Out of range	unknown	unknown	unknown
AN 5	400	SnS	0.02	2.6	$5.325\times10^{+16}$	p-type
AN 12	450	SnS+ traces of SnS_2	0.01	4.23	$2.666\times10^{+16}$	p-type